



Carolina Vesga Hernández

**Diphenyl-substituted pyridine-3,5-dicarbonitrile and
fluorenyl-substituted benzothiadiazole derivatives:
Synthesis of new fluorescent compounds with extended conjugation
for optoelectronic applications**

Dissertação de Mestrado

Dissertation presented to the *Programa de Pós-Graduação em Química* of PUC-Rio in partial fulfilment of the requirements for the degree of *Mestre em Química*.

Advisor: Prof. Dr. Jones Limberger



Carolina Vesga Hernández

**Diphenyl-substituted pyridine-3,5-dicarbonitrile and
fluorenyl-substituted benzothiadiazole derivatives:
Synthesis of new fluorescent compounds with extended conjugation
for optoelectronic applications**

Dissertation presented to the *Programa de Pós-Graduação em Química* of PUC-Rio in partial fulfilment of the requirements for the degree of *Mestre em Química*. Approved by the Examination Committee:

Prof. Dr. Jones Limberger

Advisor

Departamento de Química – PUC-Rio

Prof. Dr. Brenno Amaro Da Silveira Neto

Universidade de Brasília

Prof. Dr. Simon John Garden

Universidade Federal do Rio de Janeiro

Prof. Dr. Marco Cremona

Departamento de Física – PUC-Rio

Rio de Janeiro
February 10, 2023

All rights reserved. Reproduction of all or part of this work is prohibited without the permission of the university, the author, and the advisor.

Carolina Vesga Hernández

Graduated from the Universidad del Atlántico (Barranquilla, Colombia) in Chemistry in 2020. She has experience in Organic Synthesis with an emphasis on catalysis and organic photophysics.

Bibliographic data

Vesga Hernández, Carolina

Diphenyl-substituted pyridine-3,5-dicarbonitrile and fluorenyl-substituted benzothiadiazole derivatives: synthesis of new fluorescent compounds with extended conjugation for optoelectronic applications / Carolina Vesga Hernández; advisor: Jones Limberger. – 2023.

128 f.: il. color.; 30 cm

Dissertação (mestrado)–Pontifícia Universidade Católica do Rio de Janeiro, Departamento de Química, 2023.
Inclui bibliografia

1. Química – Teses. 2. Piridina-3,5-dicarbonitril. 3. Benzotiadiazol. 4. Emissão Aumentada Induzida por Agregação (AIEE). 5. optoeletrônicos. I. Limberger, Jones. II. Pontifícia Universidade Católica do Rio de Janeiro. Departamento de Química. III. Título.

CDD: 540

Acknowledgements

I would like to express my deepest gratitude to my professor, Dr Jones Limberger, for his invaluable guidance, patience, and feedback throughout my master's studies. This dissertation would never have been possible without his continuous support and care during the past two years.

I would like to thank the PUC-Rio, the Chemistry Department, and all the professors who taught and helped me throughout the semesters, for their warm welcome and support, even more at the beginning of this journey, when the language barrier made the challenge extra interesting.

To the examination committee, Doctors Neto, Garden, and Cremona, who generously provided their time, knowledge, and expertise in the evaluation of this work.

To LaSOQF, my second home here in Brazil, to my current and former Lab partners, especially to Julia Noronha, who was 100% involved in this work during her scientific initiation.

To all the collaborators of this work, Prof. Dr. Ricardo Aucélio and Dr. Marlin Peñafiel from LEEA; Dr. Luis Maqueira from LASURF; Prof. Dr. Marco Cremona and Dr. Rafael dos Santos Carvalho from LOEM; Prof. Dr. Leonardo De Boni and Dr. Leandro Henrique Zucolotto Cocca from the IFSC – USP; Prof. Dr. Davi Back from LMI – UFSM; Prof. Dr. Fabiano Rodembusch from AOP – UFRGS; technicians Alvaro, Diogo e Rodrigo from the Analytical Centre – PUC-Rio.

To the financial institutions for the grants and scholarships: CAPES, CNPq, and FAPERJ (grants SEI-260003/001526/2022, SEI-260003/003400/2022; scholarship FAPERJ Nota 10 SEI-260003/014588/2022).

To my family, especially my parents, my brothers, *le mie nonne*, my aunts Yaya and Tina, my stepparents, and all those who believe in me, for

all the love, support, advice, happiness, and strength that they give me even thousands of kilometres away, for being the engine of my life, my desire to move forward and to fight day by day.

To my dear friends. Kamila and Dayanne, who have been my family in Brazil, you have saved my life on many occasions. Lina, thanks for the help on my arrival to this country. Kelly, for all the time and "*surtos*" shared. Ruby, with whom I share my only neuron just like SpongeBob SquarePants and Patrick Star do, and who has been with me through all this madness, by video call in the last year, but is always there with me, *te ami*. To the grumpiest cat I've ever met, who has kept me company in the darkest episodes of my BPD, Juno.

I love you all.

"Last but not least. I want to thank me" ... Snoop Dog Style.

*A todos:
¡Gracias... Totales!*

Abstract

Vesga-Hernández, Carolina; Limberger, Jones. **Diphenyl-substituted pyridine-3,5-dicarbonitrile and fluorenyl-substituted benzothiadiazole derivatives: synthesis of new fluorescent compounds with extended conjugation for optoelectronic applications.** Rio de Janeiro, 2023. 128p. Dissertação de Mestrado - Departamento de Química, Pontifícia Universidade Católica do Rio de Janeiro.

The design of push-pull structures has led to compounds with interesting photophysical properties. This includes Aggregation-Induced Emission (AIE) and Aggregation-induced Enhanced Emission (AIEE), which are important for emission in solid state and therefore for applications in optoelectronic devices. Aiming AIEE, new fluorescent compounds with D- π -A and D-A-D characteristics were designed. Using computational tools, simulations were made to calculate their theoretical properties and validate if were appropriate for the successive development of the synthetic routes. The present work reports two new series of diphenyl-substituted pyridine-3,5-dicarbonitrile (PPC) derivatives and fluorenyl-substituted 2,1,3-benzothiadiazole (FL-BTD) derivatives, synthesized using D- π -A and D-A-D structures, respectively. The compounds presented high fluorescence quantum yields in solution, up to 0.71 in the PPC series and up to 0.67 in the FL-BTD series, displaying suitable band gaps for application as emitting layers in OLEDs. Five compounds displayed enhancement of luminescence in THF solutions containing water fraction (f_w) from 70% up to >90%, indicating AIEE properties. Among these, the derivative FL-BTD-OAM stood out, and an OLED device was built using it as an emitting layer, obtaining promising results with a device operating with high bright (luminance of 6450 cd m⁻²), good irradiance (503 mW cm⁻²) and reasonable current efficiency (0.84 cd/A).

Keywords:

Pyridine-3,5-dicarbonitrile; Benzothiadiazole; Aggregation-induced Enhanced Emission (AIEE); Optoelectronics.

Resumo estendido

Vesga-Hernández, Carolina; Limberger, Jones. **Derivados de piridina-3,5-dicarbonitril difenil-substituídos e benzotiadiazol fluorenil-substituídos: síntese de novos compostos fluorescentes com conjugação estendida para aplicações optoeletrônicas.** Rio de Janeiro, 2023. 128p. Dissertação de Mestrado - Departamento de Química, Pontifícia Universidade Católica do Rio de Janeiro.

O planejamento de estruturas push-pull tem levado a compostos com propriedades fotofísicas interessantes. Isto inclui a Emissão Induzida por Agregação (AIE) e a Emissão Melhorada Induzida por Agregação (AIEE), que são importantes para emissão em estado sólido e, portanto, para aplicações em dispositivos optoeletrônicos. Visando AIEE, novos compostos fluorescentes com características D- π -A e D-A-D foram planejados. Usando ferramentas computacionais, foram feitas simulações para calcular as propriedades teóricas dos compostos desenhados e validar se eram apropriadas para o desenvolvimento sucessivo das rotas sintéticas.

No presente trabalho, duas novas séries de derivados de piridina-3,5-dicarbonitrilo difenil-substituído (PPC) e derivados de 2,1,3-benzotiadiazol fluorenil-substituído (FL-BTD) foram sintetizados usando estruturas D- π -A e D-A-D, respectivamente. As estratégias sintéticas usadas para a sínteses dos novos compostos incluem reações multicomponente de Hantzsch (na produção do principal intermediário na série PPC), assim como reações de acoplamento cruzado C-C catalisadas por paládio, incluindo Heck, Sonogashira e Suzuki e acoplamentos N-C via reação Buchwald-Hartwig para a obtenção dos produtos. Um total de seis novos derivados de PPC, foram obtidos e caracterizados, com rendimentos de 35 a 73%, e quatro novos derivados de BTD com rendimentos de reação de 39 a 95% são reportados.

Experimentos de espectroscopia foram realizados para a avaliação das propriedades fotofísicas dos novos derivados de PPC e BTD, abrangendo medidas de absorção, emissão, e de rendimento quântico

fluorescente (ϕ_f). Os compostos apresentaram altos ϕ_f em solução, até 0,71 na série PPC e até 0,67 na série FL-BTD, exibindo band gaps adequados para sua aplicação como camadas emissoras em OLEDs. O comportamento no estado agregado dos derivados de PPC e BTD foi avaliado, quatro compostos exibiram aumento de luminescência em soluções THF contendo fração de água (f_w) de 70% até >90%, indicando as propriedades AIEE. Um dos compostos da série PPC, MT-PPC, apresentou AIE com indução da fluorescência na mistura com f_w 80%. Na série BTD, destacou-se o derivado FL-BTD-OAM com AIEE e ϕ_f significativo, assim, um OLED foi construído utilizando-o como camada emissora, obtendo resultados promissores com um dispositivo operando com alto brilho (luminância de 6450 cd m⁻²), boa irradiação (503 mW cm⁻²) e eficiência de corrente razoável (0,84 cd/A).

Palavras chave:

Piridina-3,5-dicarbonitril; Benzotiadiazol; Emissão Aumentada Induzida por Agregação (AIEE); optoeletrônicos.

Table of Contents

List of Acronyms and Abbreviations	xii
List of Figures	xiii
List of Tables	xvi
List of Appendix Figures	xvii
Chapter 1. Introduction	19
Chapter 2. Literature review	22
2.1. Photophysical processes in organic compounds.....	23
2.2. TADF: Thermally Activated Delayed Fluorescence	28
2.2.1. Design principles of organic TADF molecules	30
2.2.2. TADF compounds with D- π -A structure based in pyridine-3,5-dicarbonitriles (PCN)	34
2.2.3. TADF compounds with D-A-D structure based on 2,1,3-benzothiadiazole (BTD).....	38
2.3. Aggregation-Induced Emission (AIE) and Aggregation-Induced Enhanced Emission (AIEE)	40
2.4. OLEDs: Organic light-emitting diodes.....	44
2.4.1. OLED's operation.	45
2.4.2. Classification of OLEDs.....	46
Chapter 3. Objectives	49
Chapter 4. Methodology	50
4.1. Materials and methods	50

4.2. Synthesis of PPC derivatives	52
4.2.1. Synthesis of Br-PPC: 4-(4-bromophenyl)-2,6-diphenylpyridine-3,5-dicarbonitrile.	52
4.2.2. Synthesis of PPC derivatives <i>via</i> Suzuki cross-coupling.	53
4.2.3. Synthesis of ST-PPC derivative <i>via</i> Heck cross-coupling.	55
4.2.4. Synthesis of PPC derivative <i>via</i> Sonogashira cross-coupling...	55
4.3. Synthesis of FL-BTD derivatives	56
4.3.1. Synthesis of BTD intermediates.	56
4.3.2. Synthesis of FL-BTD derivatives <i>via</i> Suzuki cross-coupling.	58
4.3.3. Synthesis of FL-BTD derivatives <i>via</i> Buchwald- Hartwig amination	59
4.4. Preparation of solutions for spectrophotometric analysis	60
4.4.1. Absorption analysis	60
4.4.2. Emission analysis	60
4.4.3. Fluorescence quantum yield.....	61
4.4.4. Aggregation-induced enhanced emission (AIEE)	61
4.5. OLED fabrication	62
Chapter 5. Pyridine-3,5-dicarbonitrile derivatives	64
5.1. Molecular design and synthesis	64
5.2. Theoretical simulations.....	68
5.3. Photophysical properties	70
5.4. Aggregation-induced enhanced emission (AIEE) properties	75
5.5. Partial Conclusions.....	79

Chapter 6. Fluorenyl-BTD Derivatives	81
6.1. Molecular design and synthesis	81
6.2. Theoretical simulations.....	85
6.3. Photophysical properties	87
6.4. Aggregation-induced enhanced emission (AIEE) properties.	91
6.5. Electroluminescence evaluation of FL-BTD-OAM	96
6.6. Partial Conclusions.....	98
Chapter 7. Conclusions and perspectives	99
Bibliography	101
Appendix	113
A1. ¹ H and ¹³ C NMR spectra	113
A2. Crystallographic data	122
A3. Delayed fluorescence.....	127
A4. Cyclic voltammetry	127
A5. Licenses.....	128

List of Acronyms and Abbreviations

ΔE_{ST}	Energy gap between S_1 and T_1
τ	Fluorescence lifetime
ϕ_f	Fluorescence quantum yield
ϕ_{PL}	Photoluminescence quantum yield
A	Acceptor
ACQ	Aggregation caused quenching
AIE	Aggregation-induced Emission
AIEE	Aggregation-induced Enhanced Emission
B3LYP	Becke, 3-parameter, Lee–Yang–Parr
BTD	Benzothiadiazole
CBP	4,4'-Bis(N-carbazolyl)-1,1'-biphenyl
CT	Charge transfer
CV	Cyclic voltammetry
D	Donor
DCB	Dicyanobenzenes
DFT	Density functional theory
DLS	Dynamic light scattering
EL	Electroluminescence
EQE	External quantum efficiency
FL-BTD	Fluorenyl-substituted benzothiadiazole
IC	Internal conversion
IQE	Internal quantum efficiency
ISC	Intersystem crossing
IVR	Intramolecular vibrational redistribution
OLED	Organic light-emitting diode
PCN	Pyridine-3,5-dicarbonitrile
PPC	2,6-diphenylpyridine-3,5-dicarbonitrile
RIM	Restriction of intramolecular motions
RIR	Restriction of intramolecular rotations
RISC	Reverse intersystem crossing
RIV	Restriction of intramolecular vibrations
RTP	Room temperature phosphorescence
S_0	Singlet ground state
S_n	Singlet
TADF	Thermally activated delayed fluorescence
TD-DFT	Time-dependent density functional theory
THF	Tetrahydrofuran
T_n	Triplet

List of Figures

Figure 1. State diagram representing molecular states and photophysical processes: 1. Absorption, 2. Internal conversion, 3. Intersystem crossing (S → T), 4. Intersystem crossing (T → S), 5. Vibrational relaxation, 6. Fluorescence, 7. Phosphorescence. Adapted from Klán et al. 2009. ²⁶	23
Figure 2. State diagram representing the meaning of fluorescence quantum yield (ϕ_f) and the fluorescence lifetime (τ). Adapted from Lakowicz 2006. ²⁸	26
Figure 3. Emission maxima (λ_{em}) and fluorescence quantum yields in solution for some organic fluorophores.	27
Figure 4. The transition process of photogenerated excitons for TADF...	30
Figure 5. Schematic presentation of intramolecular D-A type TADF molecules. Adapted from Tao et al. ⁴⁰	31
Figure 6. Compounds obtained by Zhang et al. (2016).	33
Figure 7. A-D-A type compounds reported by Karthik and co-workers (2021).....	33
Figure 8. Structures, λ_{em} , ϕ_{PL} and OLED's EQEs for DCB and PCN derivatives.	37
Figure 9. Structures, λ_{em} , ϕ_{PL} and OLED's EQEs for TADF D-A-D type BTB derivatives.	40
Figure 10. AIE effect in HPS. Adapted from Mei et al. (2014). ⁸	41
Figure 11. Molecular structures of THBDBA and BDBA	42
Figure 12. Shape-like of Aggregation caused quenching (ACQ) and Aggregation-induced Emission (AIE) / Aggregation-induced Enhanced Emission (AIEE).	43

- Figure 13.** Elemental processes during the operation of an OLED. 1) injection of charge carriers, 2) transport of the charge carriers, 3) formation of excitons, 4) emission of light. Reproduced from Volz et al. (2015)⁸⁵ 45
- Figure 14.** Emission mechanisms of OLEDs after carrier recombination. 46
- Figure 15.** Multi-layer structure employed in current OLED products. ETL: electron-transporting layer; EML: emitting layer; HTL: hole-transporting layer; HIL: hole-injection layer. 48
- Figure 16.** D- π -A-type PPC derivatives designed and synthesized. 65
- Figure 17.** ¹H NMR spectrum of Br-PPC (400 MHz, CDCl₃). 66
- Figure 18.** ¹H NMR spectrum of MT-PPC (400 MHz, CDCl₃). 67
- Figure 19.** The HOMO and LUMO distribution from DFT calculations of PPC derivatives. 69
- Figure 20.** UV–vis absorption and fluorescence spectra in solution using different organic solvents of the PPC derivatives. 72
- Figure 21.** State diagram for suggested TICT/LE dynamics in MT-PPC.. 73
- Figure 22.** Fluorescence decays of PPC derivatives in THF..... 74
- Figure 23.** AIE/AIEE visual tests of the compounds in mixtures THF/water with different f_w 75
- Figure 24.** Fluorescence emission profile of the PPC derivatives in THF/water mixtures with different f_w (left) and their relative fluorescence intensity where I_0 is the intensity in pure THF..... 76
- Figure 25.** Molecular and single crystal structures (top) and packed crystal structures (bottom) of FL-PPC and BP-PPC 79
- Figure 26.** ¹H NMR spectrum of FL-BTD-OAM (400 MHz, CDCl₃). 83
- Figure 27.** ¹H NMR spectrum of FL-BTD-PZX (400 MHz, CDCl₃)..... 85

Figure 28. The HOMO and LUMO distribution from DFT calculations of FL-BTD derivatives.	86
Figure 30. UV–vis absorption and fluorescence spectra in solution using different organic solvents of FL-BTD-FL.....	89
Figure 31. Fluorescence decays of FL-BTD derivatives.	90
Figure 32. Relative fluorescence intensity (left) and ϕ_{fc} (right) for FL-BTD derivatives in THF/water mixtures with different <i>fw</i> . (a, b) FL-BTD-OAM (c, d) FL-BTD- AME (e, f) FL-BTD-IDB (g, h) FL-BTD-FL	94
Figure 33. Molecular and single crystal structures (top) and packed crystal structures (bottom) of FL-BTD-OAM and FL-BTD-AME	95
Figure 34. Energy diagram of materials used in the fabricated device.	96
Figure 35. (a) electroluminescence spectrum of the OLED as a function of applied voltage. (b) Representative image of the device under operation. (c) Luminance and Potency in function of applied voltage. (d) Current efficiency as a function of luminance.....	97

List of Tables

Table 1. Average timescale of photophysical processes in Figure 1. Adapted from Klán et al. 2009. ²⁶	25
Table 2. Classification of TADF compounds based on their acceptor unit.	32
Table 3. Preparation of solutions for AIEE analyses	62
Table 4. Theoretical simulation data in eV for PPC derivatives.....	68
Table 5. Photophysical data for PPC derivatives in solution.	71
Table 6. Time-resolved fluorescence data of the PPC derivatives.....	74
Table 7. DLS measurements of nano-aggregate's size and aggregation effect.	78
Table 8. Theoretical simulation data in eV for FL-BTD derivatives.	87
Table 9. Photophysical data for FL-BTD derivatives in solution.....	89
Table 10. Time-resolved fluorescence data of the FL-BTD derivatives....	91

List of Appendix Figures

Figure A - 1. ^{13}C NMR (APT) spectrum of Br-PPC (101 MHz, CDCl_3)...	113
Figure A - 2. ^1H NMR spectrum of 2M-PPC (400 MHz, CDCl_3).....	113
Figure A - 3. ^{13}C NMR (APT) spectrum of 2M-PPC (101 MHz, CDCl_3).	114
Figure A - 4. ^1H NMR spectrum of BP-PPC (400 MHz, CDCl_3).	114
Figure A - 5. ^{13}C NMR (APT) spectrum of BP-PPC (101 MHz, CDCl_3) .	115
Figure A - 6. ^1H NMR spectrum of FL-PPC (400 MHz, CDCl_3).....	115
Figure A - 7. ^{13}C NMR (APT) spectrum of FL-PPC (101 MHz, CDCl_3)..	116
Figure A - 8. ^1H NMR spectrum of MT-PPC (400 MHz, CDCl_3).....	116
Figure A - 9. ^{13}C NMR (APT) spectrum of MT-PPC (101 MHz, CDCl_3).	117
Figure A - 10. ^1H NMR spectrum of ST-PPC (400 MHz, CDCl_3).	117
Figure A - 11. ^{13}C NMR (APT) spectrum of ST-PPC (101 MHz, CDCl_3).	118
Figure A - 12. ^1H NMR spectrum of FL-BTD-Br (400 MHz, CDCl_3).	118
Figure A - 13. ^{13}C NMR spectrum of FL-BTD-OAM (101 MHz, CDCl_3).	119
Figure A - 14. ^1H NMR spectrum of FL-BTD-AME (400 MHz, CDCl_3)...	119
Figure A - 15. ^{13}C NMR spectrum of FL-BTD-AME (101 MHz, CDCl_3)..	120
Figure A - 16. ^{13}C NMR (APT) spectrum of FL-BTD-PXZ (101 MHz, CDCl_3).	120
Figure A - 17. ^1H NMR spectrum of FL-BTD-IDB (400 MHz, CDCl_3).....	121
Figure A - 18. ^{13}C NMR spectrum of FL-BTD-IDB (101 MHz, CDCl_3). ..	121
Figure A - 19. Crystal structures for FL-PPC (left) and BP-PPC (right).	123

Figure A - 20. Distance lengths (\AA) between short contacts and centroids for BP-PPC (top) and FL-PPC (bottom)	123
Figure A - 21. Crystal structures for FL-BTD-OAM and FL-BTD-AME ..	126
Figure A - 22. Fluorescence decays of PPC derivatives in Toluene.....	127
Figure A - 23. Cyclic voltammetry curve of FL-BTD-OAM.....	127

Chapter 1. Introduction

The discovery of thermally activated delayed fluorescence (TADF) has led to the development of a new generation of organic emitters and with it, more efficient optoelectronic devices. TADF is a promising solution to overcome the flaws and difficulties that first and second-generation OLED emitters face, such as the low efficiency of the first generation, based purely on fluorescence, or the excessive cost and toxicity of some of the components of the second-generation emitters, based in phosphorescence.

In OLEDs, when voltage is applied, the resulting excitons will be 75% in the triplet state and 25% in the singlet state, since radiative decays (emission of photons) from triplet states are “forbidden”, first-generation devices waste 75% of the electric potential energy injected to the device, whereas second-generation emitters can overcome the triplet problem due to the insertion of heavy metals, i.e., iridium, by increasing the spin-orbital coupling and allowing radiative decays from triplet states, thus, reaching internal quantum efficiencies of 100%, the development of blue phosphorescent emitters is quite challenging, forcing current devices to use inefficient blue fluorescent emitters, which is reflected in higher energy consumption.¹

Emitters with TADF can afford 100% of the excitons through reverse intersystem crossing (RISC), harvesting 75% from the triplet state in addition to the 25% from the lower singlet state. The basic design of TADF molecules includes push-pull structures with a twisted conformation generating large dihedral angles to achieve the smallest possible energy gap between singlet and triplet level states (ΔE_{ST}) by separating the charge distributions of HOMO and LUMO orbitals, in benefit of the RISC process.^{2,3} Most frequent TADF emitters are D- π -A type, composed of electron donor (D) and electron acceptor (A) units connected by a π -bridge. Nevertheless, D-A-D and A-D-A types have been reported as well.⁴⁻⁷ Despite the enormous advantages that TADF emitters have, the typical linear designs

of these molecules suffer from aggregation-caused quenching (ACQ), generated by strong π - π stacking interactions, deteriorating emission efficiency in the aggregate state, and requiring that the design and construction of OLEDs includes a host-guest doping system, which can generate higher costs and time consumption.³

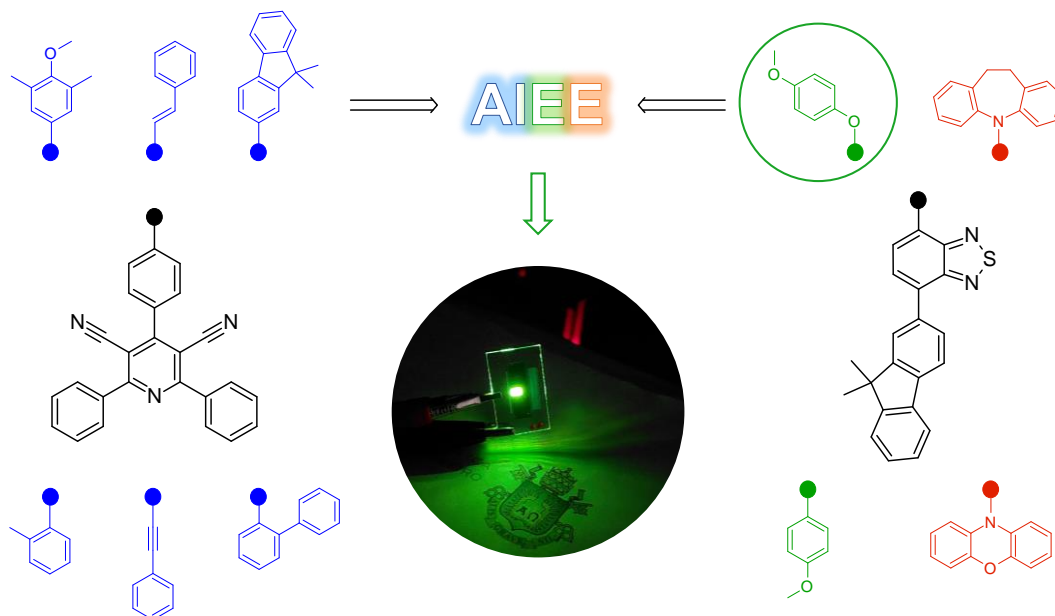
Highly emissive non-doped compounds with aggregation-induced emission (AIE) and aggregation-induced enhanced emission (AIEE) have been reported since 2001 and represent a design option to avoid the ACQ some TADF emitters exhibit. The mechanisms of AIE and AIEE processes are associated with the restriction of intramolecular motions (rotations and vibrations) with conformational and morphological alterations affecting the light-emitting performances of AIEgens/AIEEgens.⁸ In a generalized way, rigidification in aggregated state and highly twisted molecules exhibiting intramolecular steric hindrance that effectively avoid intermolecular π - π stacking are the intrinsic requirements for AIE/AIEE systems.^{9,10}

The combination of both phenomena requires careful molecular design, luckily, the structural requirements of AIEE and TADF emitters have a common ground, bonds whose rotation can be restricted when aggregation occurs and the adoption of non-planar conformations.

Bearing this in mind, this work aimed to design novel molecules that combine the two properties, using previously reported electron acceptor units with TADF or AIEE characteristics. Two families of novel chromophores were developed. The first family with D- π -A type structure derived from the pyridine-3,5-dicarbonitrile (PPC), which has multiple reports as acceptor unit of TADF emitters with good efficiency,¹¹⁻¹⁵ and the second family with the D-A-D type structure, with 2,1,3-benzothiadiazole (BTD) as the acceptor core, and which has been widely reported as an acceptor unit in compounds exhibiting AIEE.¹⁶⁻¹⁸

A total of 10 novel compounds were obtained, 6 PPCs and 4 BTDs derivatives, with cyan to green and green to orange emissions, respectively. Novel derivatives presented large stokes shifts ($\Delta\lambda_{ST}$ 121-243 nm for PPCs

and 108-157 nm for BTDs derivatives), large molar extinction coefficients, fluorescence quantum yields of up to 0.7 in solution and AIEE, for 3 PPCs and 2 BTDs derivatives, where additional analysis connecting their enhanced emission to their crystalline configuration were made.



Scheme 1. The general outline of the results obtained in this work.

Preliminary tests for the construction of OLEDs were carried out for a BTD derivative with outstanding fluorescence quantum yield and AIEE properties, obtaining promising results with a device operating with high bright, good irradiance and reasonable current efficiency (luminance of 6450 cd m^{-2} , maximum irradiance of 503 mW cm^{-2} and current efficiency of 0.84 cd/A).

Chapter 2. Literature review

In our current technological and hyperconnected society, always looking for more affordable and efficient solutions to the global energy crisis, the obtention of new materials that allow the development and manufacture of devices attending to this demand have significant importance.¹⁹ Organic semiconductors have been a milestone towards the production of devices with more flexibility, large-area, better cost-efficiency, design freedom, faster iterations, compactness, and many other benefits that may vary depending on the application of the organic semiconductor in the different optoelectronic devices, such as organic light-emitting diodes (OLEDs), where their lightness, fast emission, simple fabrication, and efficient consumption stand out.

Current research in the field of OLEDs, and optoelectronics overall, still present major challenges including colour purity, durability, and low external quantum efficiency (EQE), that is the ratio number of photons generated by injected charges, consequently demanding more energy to fulfil the requirements that today's devices need to achieve: light quality, brightness, contrast, high resolution, enhanced colour variation with low cost and low power consumption.²⁰ Foreseeing a high EQE in a device design is a complex task since there are material and structural factors that may affect the final EQE, such as the photophysical properties of the emitters, the different layers in the construction of the device, the interfaces or hosts that may be used in the production of it.²¹

Within the organic compounds used in OLEDs, they can be classified by the emission phenomena exhibited, such as fluorescence, phosphorescence or Thermally Activated Delayed Fluorescence (TADF), with the last ones as the most promising emitters in the development of more efficient devices.¹ This chapter describes the most relevant photophysical processes in organic emitters to consider for optoelectronic applications, as well as some common luminescent phenomena that may

enhance or diminish the emission efficiency of a compound as a function of its molecular (in solution) or aggregated state. And finally, OLED's device architecture, operation principles, materials and, current challenges.

2.1. Photophysical processes in organic compounds

A photophysical process is the result of the electronic excitation of a molecule – or group of molecules – induced by the absorption of light, and the subsequent events, leading to the relaxation through radiative and non-radiative transitions. No chemical alteration results, despite that bond lengths and angles may slightly change for some electronic states^{22,23}.

State diagrams, commonly referred to as Jabłoński²⁴ or Perrin²⁵ diagrams, are used to represent molecular states and photophysical processes. Figure 1 illustrates the radiative and non-radiative transitions by which molecules undergo between the different electronic states.²⁶

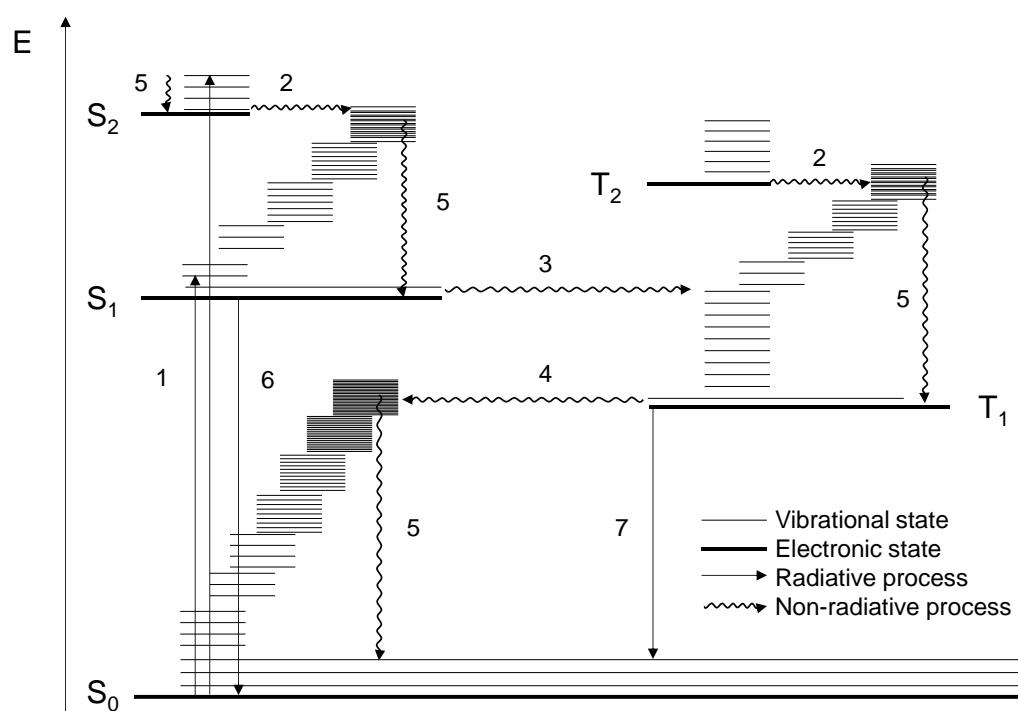


Figure 1. State diagram representing molecular states and photophysical processes: 1. Absorption, 2. Internal conversion, 3. Intersystem crossing ($S \rightarrow T$), 4. Intersystem crossing ($T \rightarrow S$), 5. Vibrational relaxation, 6. Fluorescence, 7. Phosphorescence. Adapted from Klán et al. 2009.²⁶

The thick horizontal lines represent the electronic states, and their vertical order indicates an increment in the relative energy from the bottom up, starting with the lower energy level, singlet ground state (S_0), followed by excited singlet states (S_1 , S_2 , etc.). States of higher multiplicity are represented in separate columns and their position along the abscissa is chosen to avoid congestion in the graphical diagram, without having a physical connotation. Thus, molecules with a S_0 will have their singlet electronic levels represented to the left of the diagram and triplet states to the right. The lowest triplet state is T_1 and is followed by T_2 , T_3 , etc. Vibrational states are represented by thin lines, with their lowest line being the zero-point energy level ($\nu = 0$) for each electronic state.

Radiative transitions take place between molecular states where the energy difference is absorbed or emitted as photons, and are represented by straight arrows, while non-radiative transitions are not associated with the absorption or emission of photons and are represented as wavy arrows.

Photophysical processes start with radiative excitation transitions with the **absorption** of a photon in the UV-Vis range (Fig 1. – 1), where the molecule is excited from a lower electronic state to one higher in energy.

Next, isoenergetic vibrational states from different electronic levels come into play in the non-radiative transitions. **Internal conversion (IC)** (Fig 1. – 2) is the isoenergetic non-radiative transition between two states of the same multiplicity, while **intersystem crossing (ISC)** occurs between electronic states of different multiplicity. ISC may be a process from a singlet to a triplet state (Fig 1. – 3) or vice versa, **reverse intersystem crossing (RISC)** (Fig 1. – 4). IC and ISC dissipate energy from light perturbation by distributing it over many vibrational modes, however, are slow processes, being essentially irreversible since are associated with an increment in the entropy and compete with the **vibrational relaxation** (Fig 1. – 5) which is rapid in solution. This non-radiative transition includes all processes by which the excess vibrational energy that a molecule has acquired through a vibronic transition (absorption, IC or ISC) is transferred to the surroundings through collisions with other molecules. Isolated molecules lose their

vibrational energy by infrared radiation but this process is terribly slow, hot molecules still undergo intramolecular vibrational redistribution, and it has an average time of femtoseconds in large molecules (benzene or larger).²⁷

Radiative de-excitation transitions, **luminescence**, take place via spontaneous emission of radiation from electronically excited states, including **fluorescence** and **phosphorescence**. Fluorescence (Fig 1. – 6) is the emission from excited singlet states, typically S_1 , to ground state with retention of spin multiplicity, and phosphorescence (Fig 1. – 7) from the excited triplet states, typically T_1 , to ground state with inversion of the spin multiplicity.

States diagrams show the possible transitions that can happen in a particular molecule, which are dependent on their time scales, when a transition is fast has more probability to happen as determined by the selection rules. Time scales for photophysical processes are summarized in Table 1.

Table 1. Average timescale of photophysical processes in Figure 1. Adapted from Klán et al. 2009.²⁶

Process	Name	Transition	Time scale ($\tau = 1/k_{process}$)/s
1	Absorption	$S_0 \rightarrow S_n$	10^{-15}
2	Internal Conversion	$S_n \rightarrow S_1$	$10^{-12} - 10^{-6}$
3	Intersystem crossing	$S_1 \rightarrow T_n$	$10^{-12} - 10^{-6}$
4	Intersystem crossing	$T_1 \rightarrow S_1$	$10^{-9} - 10^1$
5	Vibrational relaxation	$S_n^* \rightarrow S_n$	$10^{-13} - 10^{-12}$
6	Fluorescence	$S_1 \rightarrow S_0$	$10^{-9} - 10^{-7}$
7	Phosphorescence	$T_1 \rightarrow S_0$	$10^{-6} - 10^{-3}$

Each photophysical process mentioned before can be combined and used in state diagrams to describe more complex phenomena that may result from the interaction of matter and light, such as thermally activated delayed fluorescence (TADF), which will be discussed further in this chapter.

When discussing fluorescence and other photophysical processes, two important concepts need to be considered, **fluorescence quantum yield** (ϕ_f) and **fluorescence lifetime** (τ). Quantum yield (ϕ) is defined as “the number of defined events occurring per photon absorbed by the system”,²³ thus, ϕ_f is the number of emitted photons ($n \gamma_{em}$) relative to the number of absorbed photons ($n \gamma_{ab}$) or the number of molecules fluorescing to the total of excited molecules (excitons). Figure 2 shows the processes to return to the ground state after vibrational relaxation, emphasizing the emissive fluorescence rate of the system (k_f) and its non-radiative decay to S_0 (k_{nr}).²⁸ The rate constants k_f and k_{nr} depopulate the excited state, so fluorescence quantum yield can be denoted as:

$$\phi_f = \frac{n \gamma_{em}}{n \gamma_{ab}} = \frac{k_f}{k_f + k_{nr}} \quad (1)$$

If $k_{nr} \ll k_f$, $\phi_f \rightarrow 1$, hence, a substance with a quantum yield near 1.0 display the brightest emission, and one can say it has an efficient fluorescence.

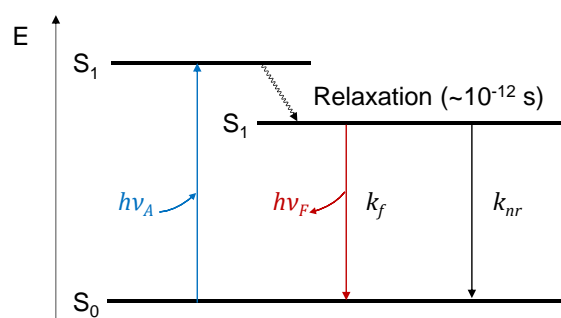


Figure 2. State diagram representing the meaning of fluorescence quantum yield (ϕ_f) and the fluorescence lifetime (τ). Adapted from Lakowicz 2006.²⁸

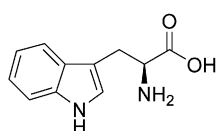
Fluorescence lifetime is defined as a “parameter describing the time evolution of the decay of the fluorescent radiant intensity”,²³ it is important since it determines the available time for the molecule to interact with the environment, and therefore obtain information about its emission. The lifetime of the excited state is the average time the molecule spends in the excited state before returning to the ground state, and is given as:

$$\tau = \frac{1}{k_f + k_{nr}} \quad (2)$$

Fluorescence is a random process and rarely an excited molecule emits the photons at exactly $t = \tau$. The lifetime of a fluorophore (fluorescent substance) in the absence of non-radiative processes is called natural lifetime, and it's denoted as the inverse of the fluorescence decay ($\tau_n = k_f^{-1}$), and can be calculated from the measured τ and quantum yield:

$$\tau_n = \frac{\tau}{\phi_f} \quad (3)$$

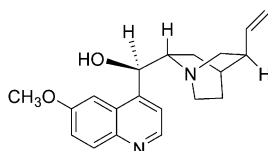
Most fluorescent compounds are organic molecules with extended conjugation. Since the observation of the phenomena in the 16th century and the first synthesis of a fluorophore in 1845,²⁹ there have been many research and applications on this matter. Figure 3 shows some common examples, with emissions going from the UV region to red (data from PhotochemCAD³⁰) and approximated wavelength to colour relationship^{31,32}.



L-Tryptophan

λ_{em} : 354 nm ○ ϕ_f : 0.12

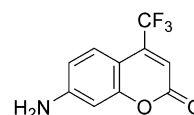
Phosphate buffer (pH 7,
0.1 M)



Quinine Sulphate

λ_{em} : 450 nm ● ϕ_f : 0.54

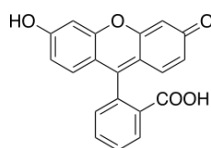
H₂SO₄ (1 N)



Coumarin 151

λ_{em} : 484 nm ● ϕ_f : 0.53

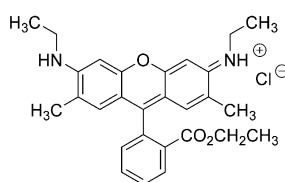
Ethanol



Fluoresceine

λ_{em} : 540 nm ● ϕ_f : 0.92

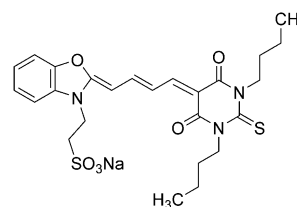
Ethanol (basic)



Rhodamine 6G

λ_{em} : 552 nm ● ϕ_f : 0.95

Ethanol



Merocyanine 540

λ_{em} : 579 nm ● ϕ_f : 0.39

Ethanol

Figure 3. Emission maxima (λ_{em}) and fluorescence quantum yields in solution for some organic fluorophores.

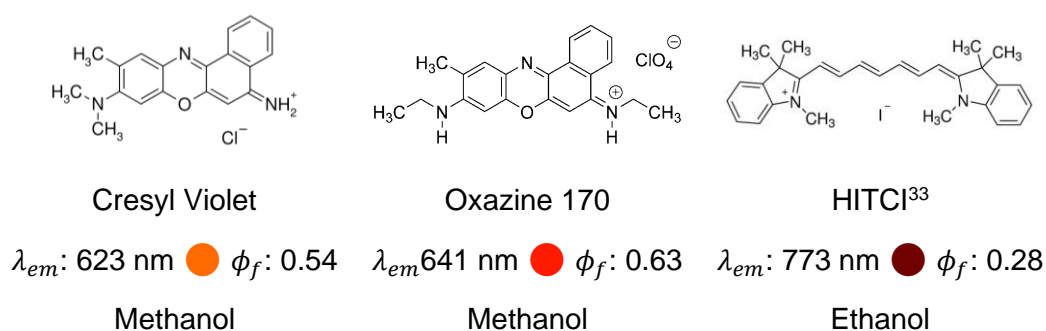


Figure 3. Emission maxima (λ_{em}) and fluorescence quantum yields in solution for some organic fluorophores (cont.).

Organic luminescent materials, whose luminescent characteristics, including colour, intensity, and emission lifetime, and that can be readily tuned through molecular structural design, have attracted considerable interest and offered extensive advanced applications in electroluminescence, organic lasers, sensors, bioimaging, forensic science, among others ^{10,34–38}.

Two interesting photophysical phenomena have attracted much attention due to the possibility of obtaining compounds with improved fluorescent quantum yields in aggregate state, as well as producing more efficient optoelectronic devices. Thermally Activated Delayed Fluorescence (TADF) and or Aggregation-Induced Enhanced Emission (AIEE) have been widely studied since their discovery and their benefits have triggered a growing demand for innovative approaches to synthesize novel compounds with desired optical and electronic properties.

2.2. TADF: Thermally Activated Delayed Fluorescence

As mentioned before organic luminescence is a radiative deactivation of excitons from the excited state to the ground state that can occur with different spin multiplicities, such as singlet or triplet excited states, which results in fluorescence or phosphorescence. According to the selection rule of quantum mechanics theory²⁶, the transition between two electronic states with the same spin multiplicity (without spin changes) is

allowed, while electrons are forbidden to jump between two states of different spin multiplicity (intersystem crossing with spin changes).

In most cases, the ground states (S_0) of organic molecules are singlets; therefore, the radiative transition of singlet excitons from the lowest singlet excited state (S_1) to the ground state for fluorescence is theoretically allowed, which is a fast process with a short lifetime of around nanoseconds. In contrast, phosphorescence is a theoretically forbidden radiation transition of triplet excitons from the lowest triplet excited state (T_1) to the ground state and exhibits a much longer lifetime ranging from microseconds to milliseconds, which is easily disturbed by external conditions, such as heat and oxygen. In addition, the transition between excited states with different spin multiplicities (such as S_1 and T_1) is also theoretically forbidden. Therefore, pure organic luminescent molecules whose energy gaps between S_1 and T_1 (ΔE_{ST}) are generally large (above 0.5 eV) usually exhibit fluorescence and non-phosphorescence. However, with the help of spin-orbit coupling from heavy metal atoms, the rate of ISC in organic metal complexes can be dramatically enhanced, resulting in strong room temperature phosphorescence (RTP). Interestingly, TADF is a special radiative transition of excitons from the S_1 state, which shows RISC and a delayed emission with a longer lifetime than the prompt fluorescence.³

RISC from T_1 to S_1 generates the final emissive singlet excitons that are involved in the TADF process (Figure 4). The energy level of the S_1 state is usually located above that of the T_1 state; therefore, RISC in the TADF process becomes an endothermal process, which makes it thermally activated with stronger emission at high temperatures.^{3,39}

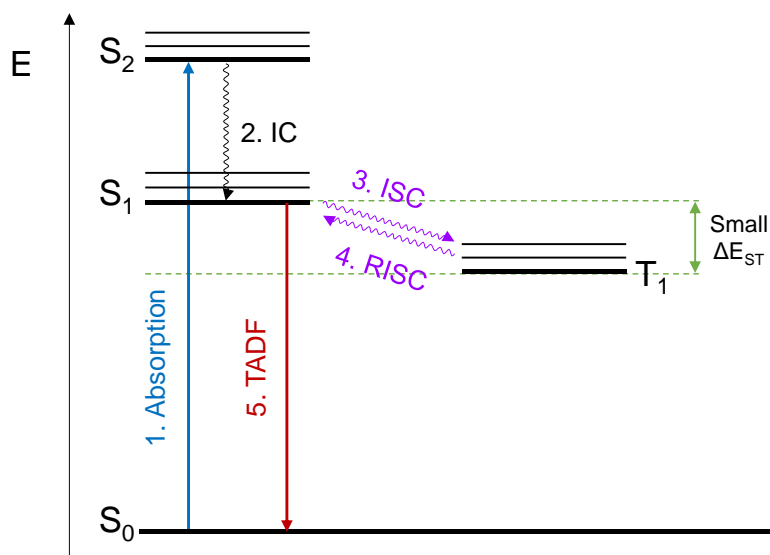


Figure 4. The transition process of photogenerated excitons for TADF.

2.2.1. Design principles of organic TADF molecules

Tao et al.⁴⁰ have summarized some design principles for donor-acceptor (D-A) type TADF molecules according to the relevant literature regarding TADF, especially for high-performance OLED applications. These rules include: (1) Separated HOMO (highest occupied molecular orbital) and LUMO (lowest unoccupied molecular orbital) in donor and acceptor groups respectively to achieve small ΔE_{ST} , (2) D-A molecular structure with a twist between the donor and acceptor moieties, caused by bulky substituents or a spiro-junction, to obtain a smaller ΔE_{ST} , (3) densely combining donors and acceptors as well as strengthening the rigidity of the molecular structure to enhance radiative luminescence efficiency, (4) the π -conjugation length and (5) the redox potential of the donor and acceptor moieties along with the interruption of the conjugation between them. In 2012, Méhes and collaborators reported a spiro-acridine derivative with TADF, they synthesized a D-A structure consisting of an acridine donor, spiro-conjugated in the C-9 position of a fluorene unit. Two CN groups were attached to the fluorene moiety to enhance its electron-accepting ability. This strategy yielded a photoluminescence quantum yield (ϕ_{PL}) of 0.67, a small ΔE_{ST} of 0,028 eV, and EQE value of 10.1% for an OLED using the molecule as an emissive layer.⁴¹ Figure 5 shows a representation of D-A

type TADF molecules and the spiro-acridine derivative from Adachi's work as an example.

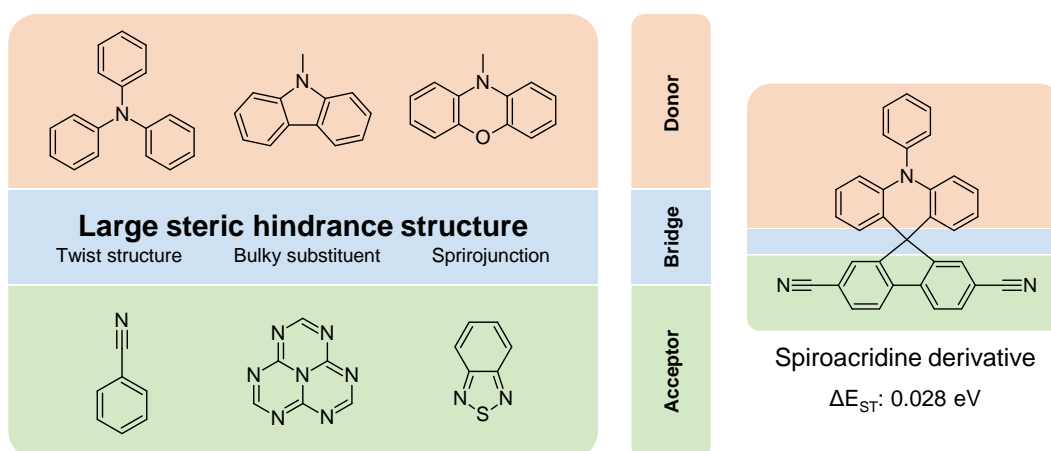


Figure 5. Schematic presentation of intramolecular D-A type TADF molecules. Adapted from Tao et al.⁴⁰

In D-bridge-A systems, the excited states are achievable by intramolecular charge transfer, generally resulting in low photoluminescence efficiency due to limited frontier orbital overlap. Therefore, is important a good choice of bridges that will connect and hybridise the donor and acceptor components.

Just like the bridge portion, the choice of donor and acceptor moieties is crucial. There is a wide range to select organic donor moieties, where N-containing aromatics stand out due to their strong electron-donating ability and their stable and high triplet states, i.e., carbazoles, diphenyl amines, phenoxazines (PXZ), phenothiazine (PTZ), 9,9-dimethyl-9,10-dihydroacridine (DMAC), 5-phenyl-5,10-dihydrophenazine (PPZ), 5,10-dihydrophenazine (DHPZ), azasiline and their derivatives.^{2,3,40,42} Among the acceptor moieties various types have been used to tune the TADF characteristics, like emission colour, excited state lifetime and TADF quantum yield. In 2017, Yang and collaborators classified TADF molecules by their acceptor units which can be appreciated in Table 2.³

Table 2. Classification of TADF compounds based on their acceptor unit.

Acceptor unit	Subcategories
N-Containing unit	Cyano-substituted aromatics
	Triazine
	Pyrimidine
	Heptazine
	Pyrazine based unit
	Quinoxaline
Diphenyl sulfoxide-based unit	Dibenzo[a,j]phenazine
	Diphenyl sulfoxide
	Dibenzothiophene-S,S-dioxide
	Thianthrenetetraoxide
Benzophenone-based	9,9-Dimethyl-9H-thioxanthene-10,10' -dioxide
	Benzophenone
	Xanthone
	Anthraquinone
Electron-withdrawing spiro-unit	Thioxanthone and its derivatives
Triarylboron based unit	
Other electron-withdrawing units as acceptors	Trifluoromethylbenzene
	Oxadiazole, thiadiazole and triazole units
	Phenoxaphosphine oxide and phenoxathiin dioxide units

Other design strategy includes intermolecular charge transfer (CT) between two individual donor and acceptor molecules. Exciplex systems have shown good efficiency in TADF devices. In 2012 Adachi and co-workers, reported the first TADF OLED using an exciplex system, m-MTDATA as the donor material and 3TPYMB as the acceptor material, with the external quantum efficiency (EQE) reaching 5.4%.⁴³ Recently, exciplex systems achieved up to 20% EQE without dopant and up to 32% using a phosphorescent emitter.⁴⁴

Although molecules with D-A and D- π -A structures have gathered more attention than other types, there are reports in the literature about D-A-D, D- π -A- π -D and A-D-A structures with TADF. Zhang and collaborators (2016) reported D-A-D type TADF emitters, using o-phthalodinitrile (PN) as

the acceptor unit and different donor units, DMAC, PXZ, and PTZ, obtaining the compounds in Figure 6. DMAC-PN showed the highest ϕ_{PL} in degassed toluene solution out of the three compounds presented, it was attributed to a lower intramolecular π - π stacking. The DMAC-PN compound was used for the fabrication of an OLED device, hosted in bis[2-(diphenylphosphino)phenyl]ether oxide (DPEPO), affording a red emission (594 nm) and EQE of 7.2%, which demonstrated TADF doped emitters can be an effective way to fabricate red OLEDs.⁴⁵

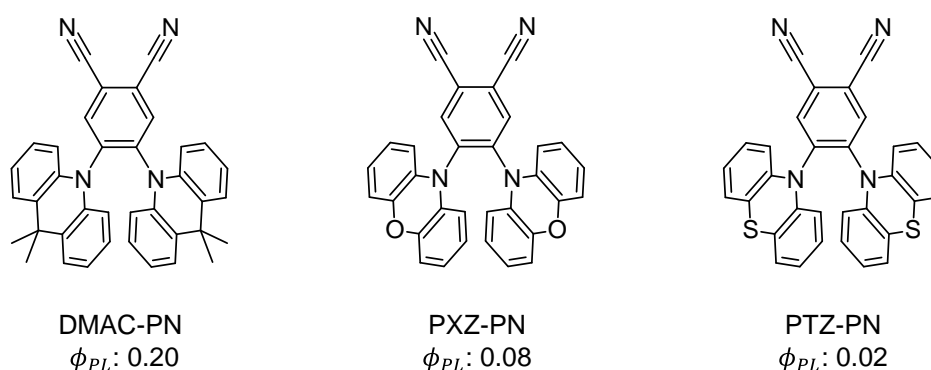


Figure 6. Compounds obtained by Zhang et al. (2016).

Karthik et al. (2021) reported orange to red TADF compounds with A-D-A structure, EQE over 30% and low efficiency roll-off^a, using rigid boron acceptors and dihydrophenazine as donor moieties. The high efficiency and low roll-off of these materials were attributed to the good electronic properties originating from the A–D–A molecular configuration.⁶

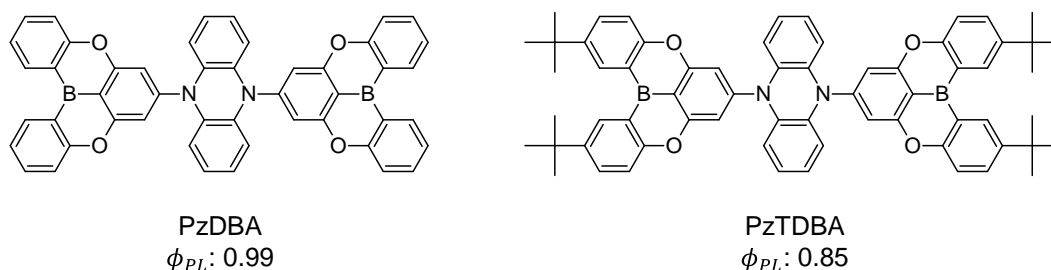


Figure 7. A-D-A type compounds reported by Karthik and co-workers (2021).

^a Decrease in OLED efficiency with increment of brightness, present in most OLEDs.¹⁰⁵

2.2.2. TADF compounds with D- π -A structure based in pyridine-3,5-dicarbonitriles (PCN)

Cyano-substituted aromatics acceptors have been widely used for the construction of TADF molecules with D-A and D- π -A structures. The strong electron-withdrawing character of the CN- group, yields effective acceptors when using it as a substituent in aromatic compounds, playing a key role in the production of highly efficient TADF materials.⁴⁶

Dicyanobenzenes (DCB) are known for altering chemical bonds in the excited state, changing their electronic properties and making them an important subunit to obtain high photoluminescence efficiencies. Coupling them with good donating groups is a promising option to produce TADF compounds.³⁴

Uoyama and collaborators, reported the synthesis of a series of new emitters using 1,2-, 1,3-, and 1,4-DCB as acceptors and carbazole units as donors adjusting the position and quantity of carbazole units in the central acceptor ring, as well as selected substitutions in the carbazoles. Two of these compounds stand out (Figure 8). 4CzIPN presented green emission (507 nm) with high ϕ_{PL} of 0.94. For the evaluation as an emissive layer, it was hosted in 4,4'-Bis(N-carbazolyl)-1,1'-biphenyl (CBP) providing an OLED with EQE of 19,3%. 2CzPn had a blue emission (473 nm) but lower a ϕ_{PL} (0.47), while its OLED, using 2,8-bis(diphenylphosphoryl)dibenzo [*b,d*]thiophene (PPT) as host material, yielded an EQE of 8%, which is higher than the values obtained from conventional fluorescence-based OLEDs. It is also noteworthy that this was the first sky-blue OLED reported.³⁴ It is important to highlight that 2CzPn and 4CzIPN are among the best-known cyanobenzene-based TADF materials in the industrial and academic fields.^{46–50}

Dicyano-N-heterocyclics, have received less interest than DCB, highly likely because of the higher cost of their synthesis⁴⁶, however, are also promising moieties for the design of new acceptor units to be used in TADF materials. Pyridine-3,5-dicarbonitriles (PCN) have been reported to

have exceptional carrier transporting properties and good electrochemical stability, derivatives with PCN as the acceptor unit usually have TADF and OLEDs achieving high EQEs of up to nearly 40% were reported.^{11–15,47,51–57}

In 2015, Liu and co-workers reported CPC (Figure 8), a blue TADF emitter based in carbazole units as donators and PCN as acceptor, the 13 wt % CPC doped in mCP host, showed a fair ϕ_{PL} of 0.49 and its OLED exhibits an outstanding EQE of 21.2%.¹⁵

Similar compounds were developed later, using D- π -A systems with PCN as the acceptor, a π conjugated bridge and PXZ as donor moieties. Compounds PXZ-PCN, Bis-PXZ-PCN and Tris-PXZ-PCN (Figure 8) were evaluated in film (doped 10 wt% CBP) obtaining orange to red emissions and ϕ_{PL} from 0.34 to 0.57. Devices fabricated with the doped emitters displayed EQEs from 9.7 to 15.1%, although EQEs weren't considerably high, these devices presented exceptionally low efficiency roll-off values of 15 to 17.5% at high luminance of 1000 cd m⁻².¹¹

To study the effects of the relative position and the number of donors, Jayakumar and collaborators designed highly congested emitters using the PCN core as acceptor and di-*t*-butylcarbazoles as donor units. Three blue to green TADF molecules were reported, 26tCzPPC, 246TCzPPC, and 35tCzPPC (Figure 8). The emitters exhibited ϕ_{PL} from 0.85 to 0.98, ΔE_{ST} from 63 to 120 meV and EQEs from 18.2 to 29.6%, with 246TCzPPC, the more congested of all, with the smallest ΔE_{ST} and highest EQE for the electroluminescent device. Highlighting the significant impact of donor adjustment in the design of novel emitters.⁵⁴

Further modifications in donor moiety and substituents of the acceptor were made. In 2020, Liu's team reported D- π -A systems with DMAC as the donor, keeping the PCN backbone and benzene as π conjugated bridge. The authors aimed to validate the relation between minor modifications in the structure of the acceptor and their properties. Compounds Ph-DMAC, Na-DMAC and 3Py-DMAC (Figure 8) were synthesized and studied, doped films (10 wt% in CBP) had green emissions

and ϕ_{PL} of 0.89, 0.56 and 0.60, respectively, the negative effect in ϕ_{PL} was attributed to the extra vibration modes induced by naphthyl and pyridyl substitutions. OLEDs fabricated using the compounds as emissive layers had EQEs from 21.2 to 29.1%, with Ph-DMAC accomplishing the higher efficiency, with the TADF characteristic of each compound having an impact on the efficiency roll-off.⁵⁶

Similar modifications in the 2,6-position of the PCN were made, producing naphthyl- and thienyl-substituted pyridine-3,5-dicarbonitriles functioning as acceptors, keeping the benzene as π conjugated bridge, and using PXZ as the donor for D- π -A type molecules (Figure 8). Doped films of NP and TP (10 wt% CBP) had λ_{em} and ϕ_{PL} of 560 nm and 0.50 for NP and 555 nm and 0.40 for TP. For the evaluation of the doped emitters, optimized OLEDs were made, obtaining yellow electroluminescence (EL) and EQEs of 594nm and 17.1% for NP and 591nm and 12.4% for TP, ascribing it to the fine confinement of excitons.⁵⁷

Chen and collaborators reported triarylamine-pyridine-carbonitrile-based TADF compounds, TPAPPC, TPAmPPC, and tTPAmPPC (Figure 8), with exceptional ϕ_{PL} of 1.0, 1.0 and 0.79 respectively for measurements in doped film (10 wt% emitters in 9-(3-(9H-carbazol-9-yl)phenyl)-9H-carbazole-3-carbonitrile – mCPCN). Devices constructed with these compounds as doped emitters presented EQEs of 37.5 (TPAPPC), 39.8 (TPAmPPC) and 29.8% (tTPAmPPC).¹²

The results of these studies show PCN as an efficient acceptor unit in designing TADF emitters with better results for 2,6-diphenyl substituted PCNs. Figure 8 summarizes the structures, λ_{em} , ϕ_{PL} and the optimized OLED's EQEs for the DCB and PCN derivatives mentioned before.

Despite the impressive results obtained with PPC derivatives as emitting layers for OLEDs, biaryl-PPC type TADF compounds, nor studies associating TADF and AIEE in PPC derivatives, have been described.

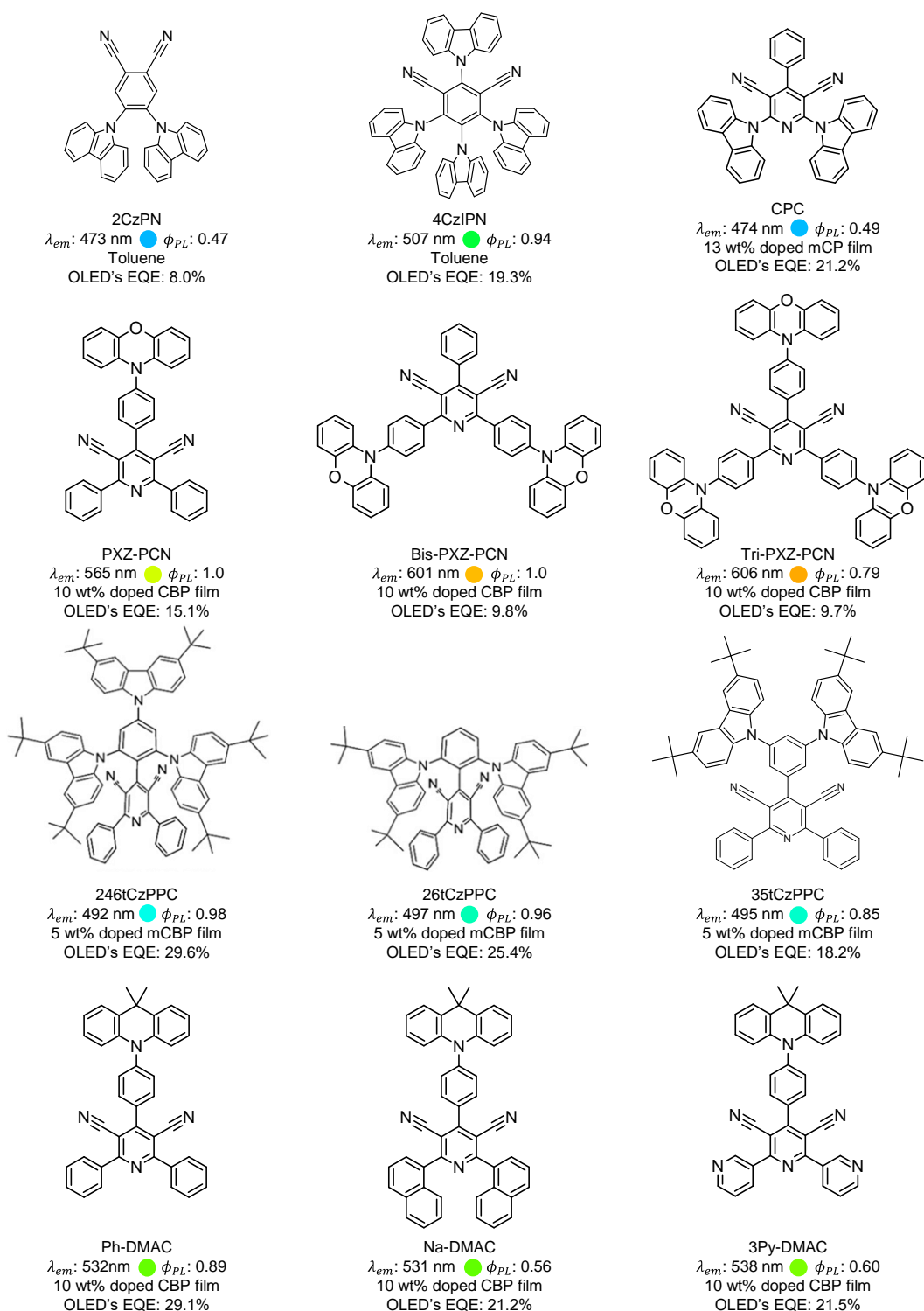


Figure 8. Structures, λ_{em} , ϕ_{PL} and OLED's EQEs for DCB and PCN derivatives.

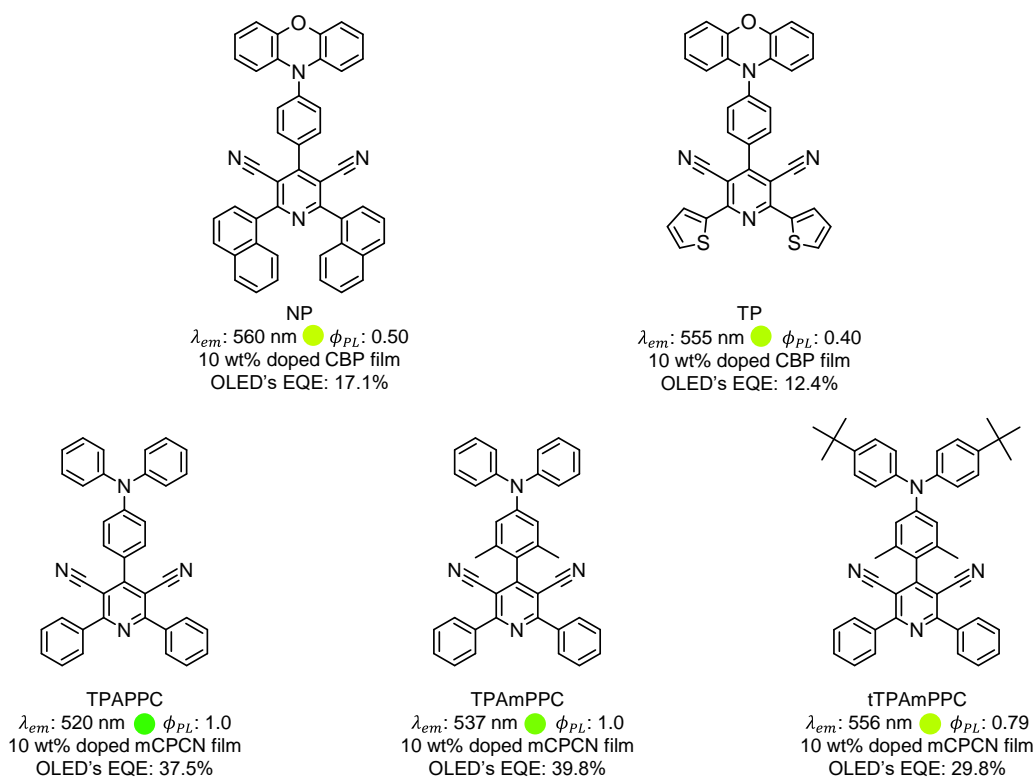


Figure 8. Structures, λ_{em} , ϕ_{PL} and OLED's EQEs for DCB and PCN derivatives.

2.2.3. TADF compounds with D-A-D structure based on 2,1,3-benzothiadiazole (BTD)

2,1,3-Benzothiadiazoles (BTD) are strong acceptor moieties used for the design of luminophores with vast applications, among which optoelectronics and bio-probes stand out, compounds containing the BTD unit generally present desirable characteristics for their application as semiconductors: (1) BTD possess a strong electron-withdrawing ability, and derivatives containing it are potential candidates for the obtention of electron carrier materials. The high emissive capacity of the compounds having BTD core is given by its electron acceptor characteristic, which can be coupled to groups that possess a great capacity to donate electrons, affording efficient emitters, conductors and semiconductor materials. (2) BTDs present a relatively high reduction potential and electron affinity, important for their use in optoelectronic technologies. (3) BTDs have highly polarized properties, leading to intermolecular interactions of the kind of π - π

interactions and heteroatoms short contacts, resulting in well-ordered crystal structures. The aforementioned makes BTDs an important piece in the design of new materials with optoelectronic applications. ^{36,58–64}

Many D-A-D type TADF s have been reported using benzothiadiazole as the acceptor unit. Although the EQEs are not as high as the ones reported for other TADF derivatives, BTD TADF emitters have gathered attention mainly in the development of deep-red and near-infrared OLEDs.

In 2018, Ni and co-workers reported a symmetric D-A-D type BTD TADF derivative with red emission. BTZ-DMAC presented a fluorescence quantum yield in doped CBP film (3 wt%) of 0.56, affording an OLED device with a max EQE of 8.8% using it as TADF emissive layer.⁶⁵

Symmetric “hot exciton” D-A-D type TADF emitters have been reported as well, using BTD as the acceptor core and 9-dimethyl-9H-fluoren-2-yl as donor units, with emissions from blue to green and ϕ_{PL} up to 0.98 in 2-Me-THF solution and 0.89 in doped thin films (30 wt% in SPPO1). BTH-DMF, 2F-BTH-DMF and o-BTH-DMF afforded devices with EQE maxima from 1.51 to 9.13 % when used as doped emitters.⁶⁶

Kumsampao and co-workers reported a near-infrared D-A-D type TADF emitter having 5,6-dicyano[2,1,3]benzothiadiazole as the acceptor and triphenylamine (TPA) as the electron-donating unit. TPACNBz showed emissions and ϕ_{PL} at 674 nm and 0.7, and 710 nm and 0.52 in toluene solution and 30 wt% TPACNBz:CBP doped film, respectively. The doped emitter was used as an emissive layer affording EQE of 6.57% for the device.⁶⁷

An asymmetric D-A-D type BTD derivative was reported to show TADF as well as AIE characteristics. BCZ-BTD-AD was used as an emissive layer, for the obtention of a non-doped pure red OLED with EQE of 2.3%. A doped version (20 wt% in CBP) showed a slight improvement in the EQE of the device, obtaining an EQE of 5.6%.⁶⁸

The structures, λ_{em} , ϕ_{PL} and OLED's EQEs for the TADF D-A-D type BTD derivatives previously described are represented in Figure 9.

Despite the substantial number of works describing BTD derivatives as emitter layers in OLEDs, there is a limited number of reports on D-A-D type TADF emitters. which opens the possibility to explore this topic further to understand the relationship between the BTD as an acceptor core and its influence in TADF systems.

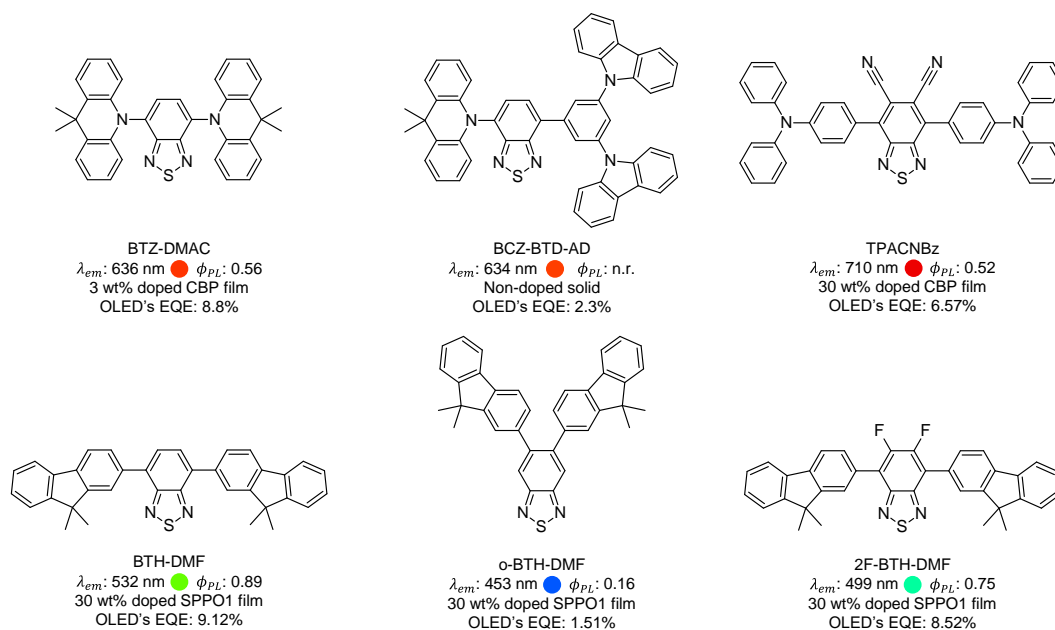


Figure 9. Structures, λ_{em} , ϕ_{PL} and OLED's EQEs for TADF D-A-D type BTD derivatives.

2.3. Aggregation-Induced Emission (AIE) and Aggregation-Induced Enhanced Emission (AIEE)

Aggregation-induced emission (AIE), discovered in 2001 by Tang et al.,⁶⁹ and Aggregation-induced enhanced emission (AIEE), first described in 2002 by Park et al.,⁷⁰ are photophysical phenomena associated with chromophore aggregation. AIEgens and AIEEgens are non-emissive or weakly emissive, respectively, when the molecules are genuinely dissolved in a good solvent but are induced to emit by the aggregate formation. With a plethora of applications that go from chemo-sensing to optoelectronics,

AIEE has opened new avenues to an array of possibilities with immense potential for high-tech innovations.^{8,71}

Conventional luminophores have high emission when they are acting as isolated species, like in diluted solutions, however, as aggregates their emission is quenched due to intense intermolecular π - π stacking interactions, promoting energy dissipation through non-radiative channels, which affects negatively the emission processes, it happens specially to compounds with planar or disk-like structures, and is known as aggregation caused quenching (ACQ). The ACQ effect that many fluorescent organic molecules present, has prevented them from being employed in everyday technologies since most of the applications require them to be used as a whole (aggregates) and not as individual molecules,¹⁰ especially in optoelectronic applications (i.e., OLEDs), where the luminophores are normally used in the aggregated state as thin solid films.^{1,72,73}

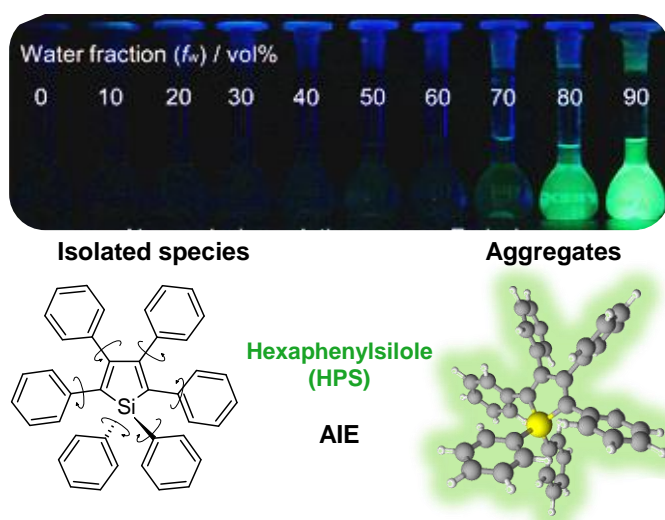


Figure 10. AIE effect in HPS. Adapted from Mei et al. (2014).⁸

With AIEEgens the opposite effect occurs, as isolated species, there is no or weak emission, however as the aggregates form, a sharp increase in the emission is observed. Figure 10 displays the classical AIE example, hexaphenylsilole (HPS), in diluted solutions with a good solvent no emission is detected, but as the fraction of poor solvent increases the molecules are forced to form nano-aggregates, and once the fraction of said solvent

reaches a critical point the emission is perceived. The absence of emission in HPS dilute solutions can be associated with the dynamic rotations of the phenyl rings against the silole core, on the single bond axes, dissipating the energy from the excited state through non-radiative pathways. However, when forming aggregates, those rotations are restricted, due to the physical constraint, and the radiative relaxation channels are activated.

The restriction of intramolecular rotations (RIR) has been associated as the responsible for the AIE/AIEE effect in molecular rotors. However, it does not apply to all molecular systems. The RIR mechanism is unable to explain the AIE/AIEE effect in molecules without freely rotatable components, so for molecules such as THBDBA and BDBA (Figure 11), without rotors but with flexible components, another form of intramolecular motion has been associated, vibrations, hence, the restriction of intramolecular vibrations (RIV) may be also able to induce AIE/AIEE. For “isolated” species in dilute solutions, low frequency motions are associated with the non-radiative excited-state decay process, when suppressed, either due to aggregation, high viscosity or low temperatures, radiative decay pathways predominate.⁷⁴ Therefore, AIE/AIEE can occur not only by RIR but also through RIV as well, thus having as a generalized mechanism, the restriction of intramolecular motions (RIM) associated with emission turn-on in aggregate states.

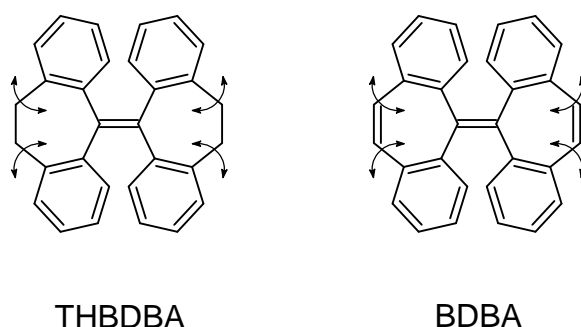


Figure 11. Molecular structures of THBDBA and BDBA

Additional aspects need to be considered for RIM to be able to act more effectively in the emission enhancement, it must be accompanied by a non-planar structure of the luminescent molecule, to avoid detrimental

intermolecular π - π interactions, leading to suppression of luminescence in the aggregate state. Basic design strategies have been developed to accomplish efficient AIE/AIEE structures, including 1) rotor or propeller-like structures, 2) transformation of ACQ chromophores to AIEgens/AIEEgens by insertion of AIE/AIEE cores and 3) Twisted π systems with not too close intermolecular distance or sufficient steric effect, to avoid π - π stacking caused by short intermolecular distance.⁷⁵

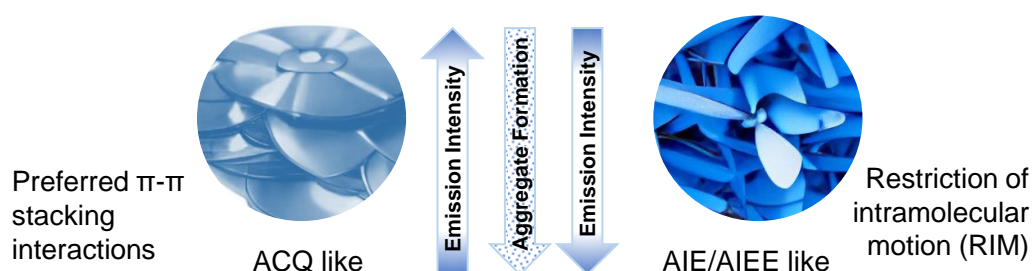


Figure 12. Shape-like of Aggregation caused quenching (ACQ) and Aggregation-induced Emission (AIE) / Aggregation-induced Enhanced Emission (AIEE).

These design strategies have been taken further to achieve molecular systems with specific properties, such as efficient AIE/AIEE-TADF luminogens. To seize high EQEs in TADF-based OLED devices, the classic host-guest doping system is applied to prevent the ACQ effect,^{76,77} making AIE/AIEE ideal in emitters to simplify device fabrication, in that way, principles for the rational design of efficient AIE/AIEE-TADF emitters and strategies to achieve small ΔE_{ST} and high ϕ_{PL} are of great interest. Despite the great advantages of emitters that include TADF and AIE/AIEE, reports of compounds or targeted research for this purpose are scarce.⁷⁸⁻⁸⁰

Multiple BTDs derivatives presenting AIE/AIEE have been reported, with applications in optoelectronics and bio-probes, several reports in the literature have been made in this regard, however, BTB derivatives that present AIE/AIEE and TADF are still limited.^{17,36,60,65,68,81-84}

A comparable situation occurs with PCN derivatives, despite their excellent results as TADF emitter layers, their high efficiencies require host-guest systems to prevent ACQ from affecting them, with little to no reports

in the literature associating them with AIE/AIEE, it is essential to find the link that associates the two properties to obtain highly luminescent doping-free emitters.^{11–15,47,51–57}

2.4. OLEDs: Organic light-emitting diodes.

OLEDs have been used in next-generation flat-panel displays and solid-state lighting technologies due to the advantages of the solid-state, high brightness, short responsive time, wide operating temperature range, wide viewing angle, low power dissipation and flexibility, which have been attracting the attention of scientists and engineers from both academic and industrial communities.⁸⁵ The luminescent materials that are employed in OLED devices include small molecular materials and polymeric materials, which can be produced by using different synthetic strategies. Thus, since Tang and Van Slyke reported the first OLED device in 1987,⁷² many organic luminescent materials with advanced device performances have been reported, which has significantly promoted the progress of OLEDs.

In general, the electroluminescence (EL) quantum efficiency is the most essential parameter for an OLED device and in particular, the EQE, which is defined as the ratio of the number of emitted photons outside the device to the apparent number of charges injected into the device. It is well known that exciton formation under electrical excitation typically results in 25% singlet and 75% triplet excitons. Only the radiative transition process of singlet excitons from the S_1 state to the S_0 state can be used in the emission of light, i.e., fluorescence, which is quantum mechanically allowed. Therefore, in organic fluorescent materials, the electrically generated 75% triplet excitons are emitted as heat rather than light. Even if the ϕ_{PL} of conventional fluorescent molecules can reach 100%, in theory, the EQE maximum value may only reach 5% due to the light out-coupling efficiency of around 20% in the OLED device. Hence, to increase the efficiency of OLED devices, one effective tactic is to break through the theoretical upper limit of quantum efficiency and use the non-emissive triplet excitons as much as possible. The study of harvesting both singlet and triplet excitons for EL is attractive for the enhancement of OLED device efficiency.⁴⁰

2.4.1. OLED's operation.

The detailed process of how OLEDs work has been described in depth in several previous works.^{1,85-89} In a simplified form, there are four fundamental steps in their operation (Figure 13). When voltage is applied across the device, positive and negative charges (electrons and holes, respectively) are generated (1). Electrons are injected from the cathode to the LUMO of the compound that acts as an electron carrier/injector. The holes, on the other hand, are injected from the anode to the HOMO of the compound that acts as a carrier/injector of holes. The electrons go towards the anode and the holes towards the cathode, these charges migrate under the effect of the applied electric field and the Coulomb attraction between the opposite charges (2). In the meantime, will occur the recombination between the holes and electrons (3) and several processes of energy transfer will happen to form singlet and triplet excitons (electron-hole pairs in the excited state) within the emitter layer (EC) and so there will be the emission of light (4).

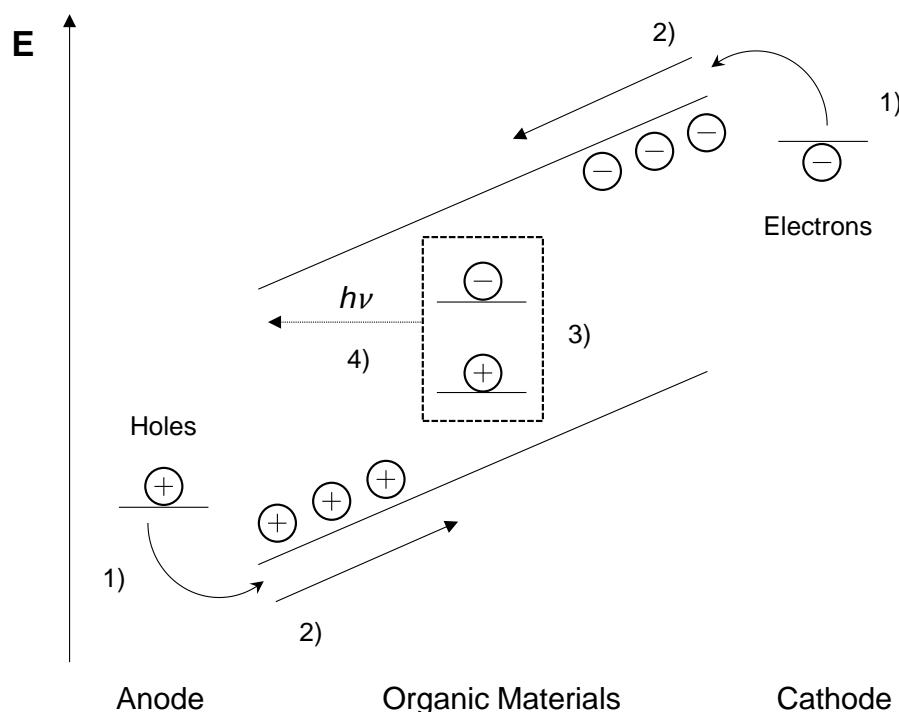


Figure 13. Elemental processes during the operation of an OLED. 1) injection of charge carriers, 2) transport of the charge carriers, 3) formation of excitons, 4) emission of light. Reproduced from Volz et al. (2015)⁸⁵

2.4.2. Classification of OLEDs

Based on the emitting layer, OLEDs can be classified into different types and generations: fluorescent, phosphorescent and thermal-activated delayed fluorescence (TADF), related to 1st, 2nd and 3rd generations respectively.^{1,90}

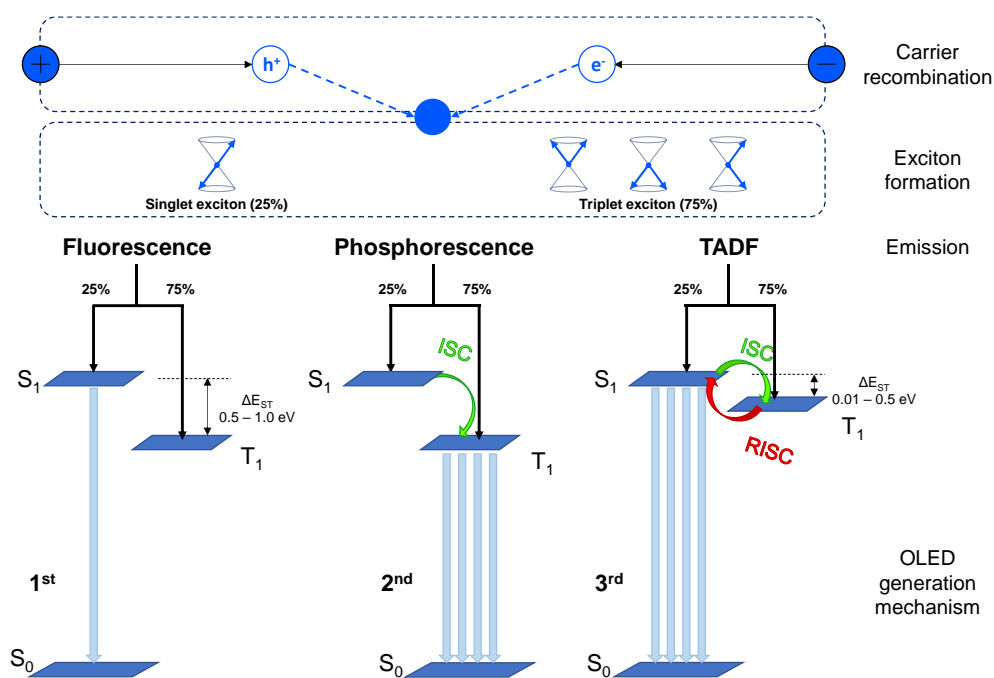


Figure 14. Emission mechanisms of OLEDs after carrier recombination.

In a device in which the emitting layer is based on the fluorescence phenomenon, only the radiative decay of singlet states is used when subjected to an electrical excitation, which in turn supplies a theoretical limit of only 25% in internal quantum efficiency (IQE).

On the other hand, by introducing heavy metals in the emitter layer, phosphorescent OLEDs can be fabricated. Due to the strong spin-orbit coupling of the metals, iridium and platinum complexes are usually used in these devices, with which the lifetime in the triplet state is reduced to microseconds, resulting in an efficient phosphorescent emitter. In these devices, there is the possibility of 100% IQE, because there is an intersystem crossing between the singlet and triplet states. The radiative decay, in this case, occurs from the triplet state.

Finally, the devices of greatest interest in this research are those that present in the emitting layer the characteristic TADF. A compound with this attribute has a low energy difference between the singlet and triplet states, which facilitates the energy exchange between these states. In this way, the electron displaced to the triplet state can return to the singlet state using thermal energy, through RISC, so that the fluorescence emission occurs (via S_1). These TADF-based devices collect great interest since an IQE of 100% can be achieved using purely organic materials.

OLEDs can be classified by their structure, and the number of layers it has. Multilayer OLEDs are the most common structures used and consist of different layers, with each of them playing a key role in the production of electrically generated light. Multilayer OLEDs consist of different layers, such as:⁷³

Substrate: Usually transparent plastic, glass, or metal foil, which is a transparent and conductive substrate with a high work function.

Anode: Transparent electrode to inject holes into organic layers.

Hole injection layer (HIL): Materials with high mobility, electron blocking capacity and high glass transition temperature.

Hole transport layer (HTL): Plays a vital role in transporting holes and blocking electrons, thus preventing electrons from reaching the opposite electrode without recombining with holes.

Emissive layer (EML): Good emitter of visible photons, requires high efficiency, lifetime, and colour purity.

Electron transport layer (ETL): This layer should have good electron transporting and hole-blocking properties.

Cathode: The cathode injects electrons into emitting layers. It is transparent in top-emitting devices. It must be stable to the organic layers under it.

The deposition of all the layers on the ITO glass substrate itself is quite important due to the sensitivity of the material to varied factors such as elevated temperature, or incorporation of dust during fabrication.⁷³ Figure 15 displays the typical structure of a multilayer OLED.

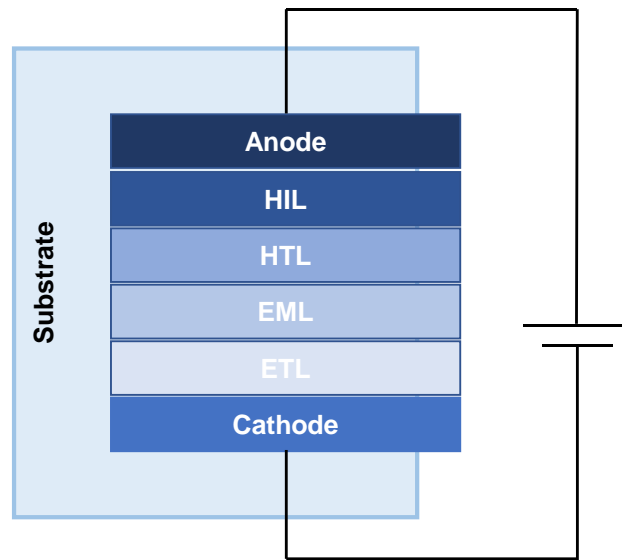


Figure 15. Multi-layer structure employed in current OLED products. ETL: electron-transporting layer; EML: emitting layer; HTL: hole-transporting layer; HIL: hole-injection layer.

Chapter 3. Objectives

In this work, we aim to design, synthesize, and characterize new luminescent compounds derived from diaryl-substituted pyridine-3,5-dicarbonitriles (PPC) and fluorenyl-substituted benzothiadiazoles (FL-BTDs). We intend to develop highly emissive compounds that display AIEE and TADF characteristics which can lead to purely organic OLED devices with high brightness and efficiency.

The following specific objectives were established for the development of the work:

- Use computational tools to design new PPC and FL-BTD derivatives with extended conjugation, displaying D- π -A and D-A-D structures, respectively by determining the energy and distribution of HOMO and LUMO orbitals via DFT, as well as the energy difference between the singlet and triplet states in the new compounds via TD-DFT.
- Synthesize novel PPC and FL-BTD derivatives using cross-coupling and multicomponent reactions.
- Conduct photophysical and electrochemical characterization of the new luminophores, determining absorption and emission maxima, band gap, Stokes shift, and fluorescence quantum yield in solution and solid state.
- Perform time-resolved fluorescence experiments to evaluate the occurrence of delayed fluorescence for the new compounds.
- Evaluate the influence of the aggregation state for the new compounds and link the occurrence of ACQ, AIE or, AIEE to their structure.
- Evaluate the performance of selected PPCs and FL-BTDs as emissive layers.

Chapter 4. Methodology

4.1. Materials and methods

All reagents and solvents used in this work were bought from commercial sources and employed as received unless otherwise indicated. Solvents used in cross-coupling reactions (Buchwald-Hartwig, Heck, Sonogashira, and Suzuki) and Hantzsch multicomponent reaction were de-aerated using a nitrogen flow.

Compounds were characterized via ^1H and ^{13}C NMR on a Bruker Advance III HD 400 MHz spectrometer. NMR analyses were performed at the Analytical Facilities “Pe. Leopoldo Hainberger” of the Chemistry Department of PUC-Rio (CAPLH PUC-Rio).

High-resolution mass spectra (HRMS) were obtained on a MICROTOF mass spectrometer (Bruker Daltonics) using direct infusion of the sample in a solution of acetonitrile, in positive mode using electrospray ionization at the Mass Spectrometry Laboratory, from Analytical Facilities of the USP's Chemistry Institute.

UV-Vis absorption spectra were acquired on a Shimadzu UV-1800 spectrophotometer with a 2 mm optical path quartz cuvette for PPC derivatives. For AIEE measurements a 10 mm optical path cuvette was used. UV-Vis spectra for FL-BTD derivatives were obtained using a Cary 100 Conc spectrophotometer with a 1 cm path length quartz cuvettes, using a scan velocity of 1200 nm min^{-1} , and spectral bandpass of 10 nm. The solution concentrations were around $10^{-5}\text{ mol L}^{-1}$. Spectrophotometers used were from the Photonics Laboratory of IFSC-USP and CAPLH – PUC-Rio, respectively.

Fluorescence measurements for PPC derivatives were obtained by a Hitachi F7000 fluorimeter in a 10 mm cuvette. To avoid reabsorption of the fluorescence signal, the solution concentrations were around $10^{-6}\text{ mol L}^{-1}$. For FL-BTD derivatives measurements were made on a model LS 55

luminescence spectrometer (PerkinElmer, USA). Photoluminescence measurements were made with a 1200 nm min⁻¹ scan rate in the 200–800 nm range, using a 10.0 nm spectral bandpass and 1 cm optical path length quartz cuvettes. When necessary, reflective density filters (F 2.0, 1.0, and 0.6) were used to avoid saturation of the detector.

Evaluations of fluorescence quantum yields were made on a model LS 55 luminescence spectrometer from PerkinElmer using 1 cm optical path length quartz cuvettes (four optical clear faces) and a 1000 nm min⁻¹ scan rate and 10.0 nm spectral excitation and emission bandpasses at the LASURF – PUC-Rio for FL-BTD derivatives.

Time-resolved fluorescence measurements were performed by using a homemade experimental setup which employs third harmonic generation (343 nm) from a 220-fs laser centred at 1030 nm working at a 1 kHz repetition rate. Experimental fluorescence decay curves were collected by a silicon fast detector and averaged in a digital oscilloscope. To analyse the fluorescence lifetime of the samples, a global fitting procedure was performed taking into consideration the instrument response function. The technique is always calibrated by using Rhodamine B dissolved in Ethanol. The equipment used was from the Photonics Laboratory of IFSC-USP.

The size of the aggregates was estimated in mixtures of THF/ water with different water fractions in a concentration of 5×10^{-6} mol L⁻¹, by dynamic light scattering (DLS) using a Zetasizer NanoSeries model Nano-ZS (Malvern Instruments) at the LASURF – PUC-Rio.

The electrochemical studies were made using a potentiostat/galvanostat (μ -AUTOLAB Type III, Metrohm) interfaced to a computer and operating in the voltammetric analysis cyclic voltammetric mode. The working electrode was a glassy carbon, the Ag|AgCl (KCl(sat)) electrode was used as the reference and a platinum wire was used as the auxiliary electrode. The electrochemical cell (15 mL volume) is of Pyrex glass with a Teflon cap with openings to adapt the electrodes. Cyclic voltammetry experiments were performed at a scan rate of 50 mV s⁻¹ at

room temperature under nitrogen. As the electrolyte, a solution of 0.04M of tetrabutylammonium phosphorus hexafluoride (TBAPF₆) in a mixture of dichloromethane and acetonitrile solution (85/15 %v/v) was used. The ferrocene was used as reference.

Theoretical calculations were made to estimate structural parameters using the 6-31G** basis set.⁹¹ Calculations were conducted using the density functional theory (DFT) method with the ORCA 4.2.1 program package.⁹² The commonly used B3LYP (Becke, 3-parameter, Lee–Yang–Parr) exchange-correlation functional approach⁹³ was employed as indicated for the study of other organic systems.⁹⁴ Molecular builder and visualizer Avogadro 1.2.0 was used to visualize molecular orbital distribution.⁹⁵

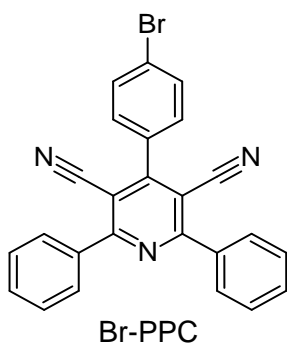
Single crystals of PPC and FL-BTD derivatives suitable for X-ray diffraction studies were grown at room temperature from concentrated solutions of dichloromethane/hexane mixtures. X-ray diffractometry was performed using a Bruker D8 Venture Photon 100 diffractometer. The structures were obtained by direct methods using the SHELXS software⁹⁶ and the graphic designs were obtained using the Mercury 4.0 software⁹⁷ for Windows. Measurements were performed by Prof. Dr. Davi Back at the Chemistry Department of UFSM. The crystallographic data and structure refinement parameters are provided in appendix (A2).

4.2. Synthesis of PPC derivatives

4.2.1. Synthesis of Br-PPC: 4-(4-bromophenyl)-2,6-diphenylpyridine-3,5-dicarbonitrile.

The synthesis of Br-PPC was achieved *via* the Hantzsch multicomponent reaction followed by oxidation of the resulting dihydropyridine. In an oven-dried screw-capped Schlenk tube, evacuated and backfilled with nitrogen, was added 4-bromobenzaldehyde (300 mg, 1.62mmol), 2.5 equivalents of benzoyl-acetonitrile (588 mg, 4.05 mmol), 10

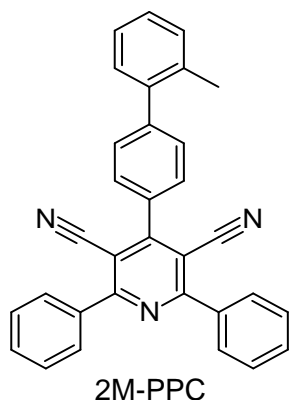
equivalents of ammonium acetate (989.5 mg, 16.20 mmol) and 41 mL of degassed glacial acetic acid. The reaction mixture was carried out at 120°C for 12h to obtain the dihydropyridine intermediate, which was not isolated. The reaction was cooled down to 66°C, afterwards, twenty equivalents of NaNO₂ were added in portions to the suspension with constant stirring, and the temperature was maintained for one hour to obtain the desired pyridine. After completion of the reaction, it was allowed to cool down to room temperature. For the extraction, 700 mL of ice-water mixture was added and afterwards, the mixture was neutralized using ammonium hydroxide. The precipitate was filtered and washed with icy water, followed by filtration under vacuum using a mixture of equal parts ethanol and toluene to afford a white/beige solid with 92% yield.



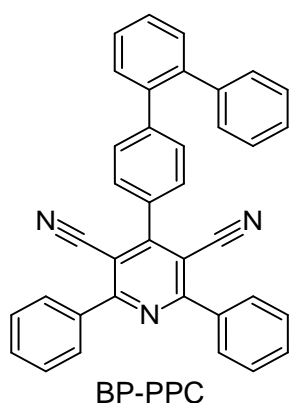
4-(4-bromophenyl)-2,6-diphenylpyridine-3,5-dicarbonitrile: White/beige solid. mp = 269 - 272 °C. 92% yield. ¹H NMR (400 MHz, CDCl₃) δ (ppm): 8.01 – 8.12 (m, 4H), 7.78 (d, *J* = 8.5 Hz, 2H), 7.64 – 7.54 (m, 6H), 7.51 (d, *J* = 8.5 Hz, 2H). ¹³C NMR (101 MHz, CDCl₃) δ (ppm): 163.5, 159.4, 136.4, 132.7, 132.5, 131.7, 130.6, 129.7, 129.0, 126.1, 115.8, 105.8. (m/z) calculated for (M+H)⁺: 437.3101, found: 437.1954.

4.2.2. Synthesis of PPC derivatives *via* Suzuki cross-coupling.

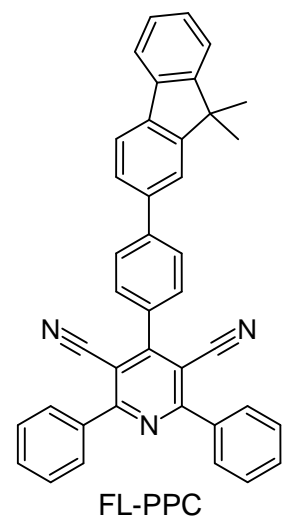
For the synthesis of each PPC derivative, oven-dried screw-capped Schlenk flasks were evacuated, back-filled with nitrogen and loaded with Br-PPC (100 mg, 0.23 mmol), Pd(OAc)₂ (0.73 mg, 3.2 × 10⁻³ mmol), PPh₃ (1.69 mg, 6.4 × 10⁻³ mmol), K₂CO₃ (30.4 mg, 0.22 mmol), arylboronic acids (0.22 mmol), degassed ethanol (1.5 mL) and degassed toluene (1.5 mL). The reactions were stirred for 5h at 75 °C, and after the reaction time, were allowed to cool down to room temperature. The solids were washed with dichloromethane (3 × 5 mL) and the solution containing the product was concentrated under reduced pressure. The crude products were then purified by column chromatography on silica gel using hexane/dichloromethane as the mobile phase.



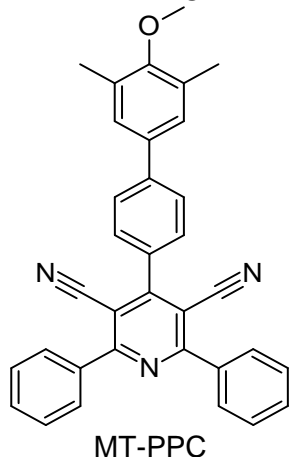
4-(2'-methyl-[1,1'-biphenyl]-4-yl)-2,6-diphenylpyridine-3,5-dicarbonitrile: White solid. mp = 211 - 213 °C. 73% yield. ^1H NMR (400 MHz, CDCl_3) δ (ppm): 8.16 – 8.06 (m, 4H), 7.72 (d, J = 8.0 Hz, 2H), 7.60 (d, J = 6.5 Hz, 8H), 7.32 (s, 4H), 2.36 (s, 3H). ^{13}C NMR (101 MHz, CDCl_3) δ (ppm): 163.2, 160.1, 144.7, 140.4, 136.3, 135.2, 132.0, 131.9, 131.8, 131.2, 130.3, 129.8, 129.6, 129.4, 128.9, 128.6, 128.6, 128.4, 128.3, 128.1, 127.7, 125.8, 125.1, 115.8, 114.7, 105.7, 20.3. HRMS (m/z) calculated for ($\text{M}+\text{H}$) $^+$: 448.5366, found: 448.1807



4-([1,1':2',1''-terphenyl]-4-yl)-2,6-diphenylpyridine-3,5-dicarbonitrile: White solid. mp = 234 – 337 °C. 46% yield. ^1H NMR (400 MHz, CDCl_3) δ (ppm): 8.13 – 8.02 (m, 4H), 7.63 – 7.53 (m, 7H), 7.53 – 7.43 (m, 5H), 7.39 (d, J = 8.4 Hz, 2H), 7.30 – 7.20 (m, 3H), 7.20 – 7.13 (m, 2H). ^{13}C NMR (101 MHz, CDCl_3) δ (ppm): 163.3, 160.5, 144.6, 140.9, 140.9, 139.5, 136.6, 131.9, 131.5, 130.8, 130.5, 130.1, 129.7, 128.9, 128.6, 128.4, 128.3, 127.8, 126.9, 115.9, 106.1. HRMS (m/z) calculated for ($\text{M}+\text{H}$) $^+$: 510.6060, found: 510.1964.



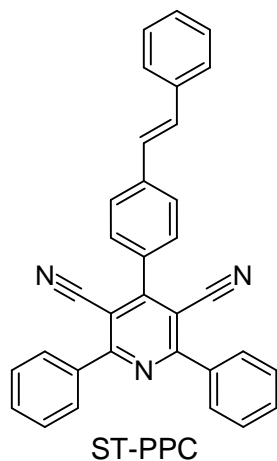
4-(4-(9,9-dimethyl-9H-fluoren-2-yl)phenyl)-2,6-diphenylpyridine-3,5-dicarbonitrile: White solid. mp = 223 - 225 °C. 46% yield. ^1H NMR (400 MHz, CDCl_3) δ (ppm): 8.16 – 8.06 (m, 4H), 7.92 (d, J = 8.2 Hz, 2H), 7.84 (d, J = 7.9 Hz, 1H), 7.81 – 7.73 (m, 4H), 7.68 (d, J = 7.8 Hz, 1H), 7.64 – 7.51 (m, 6H), 7.51 – 7.43 (m, 1H), 7.43 – 7.32 (m, 2H), 1.58 (s, 6H). ^{13}C NMR (101 MHz, CDCl_3) δ (ppm): 163.6, 160.3, 154.6, 154.1, 144.5, 139.5, 139.0, 138.8, 136.6, 132.2, 131.5, 129.7, 129.7, 128.9, 127.9, 127.7, 127.2, 126.5, 122.8, 121.8, 120.6, 120.4, 116.2, 106.0, 47.2, 27.4. HRMS (m/z) calculated for ($\text{M}+\text{H}$) $^+$: 550.6699, found: 550.2273.



4-(4'-methoxy-3',5'-dimethyl-[1,1'-biphenyl]-4-yl)-2,6-diphenylpyridine-3,5-dicarbonitrile: White solid. mp = 300 – 303 °C. 64% yield. ^1H NMR (400 MHz, CDCl_3) δ (ppm): 8.13 – 8.02 (m, 4H), 7.79 (d, J = 8.5 Hz, 2H), 7.70 (d, J = 8.5 Hz, 2H), 7.64 – 7.54 (m, 6H), 7.34 (s, 2H), 3.79 (s, 3H), 2.38 (s, 6H). ^{13}C NMR (101 MHz, CDCl_3) δ (ppm): 164.2, 160.9, 146.3, 144.6, 137.3, 136.1, 132.6, 132.1, 130.5, 130.2, 129.6, 128.6, 128.3, 116.8, 106.7, 60.6, 17.0. HRMS (m/z) calculated for ($\text{M}+\text{H}$) $^+$: 492.5892, found: 492.2067.

4.2.3. Synthesis of ST-PPC derivative *via* Heck cross-coupling.

An oven-dried screw-capped Schlenk flask was evacuated, back-filled with nitrogen and loaded with Br-PPC (104mg, 0.24 mmol), styrene (0.25 mmol; 26.33 mg), Pd(OAc)₂ (1.4 mol%; 0.8 mg), PPh₃ (2.7 mol%; 1.7 mg), NaOAc·3H₂O (0.24 mmol, 32.7 mg) and degassed DMF (1 mL). The reaction was stirred at 130 °C for 24 h and allowed to cool down to room temperature. The mixture was then diluted with dichloromethane (10 mL) and washed with water (3 × 5 mL). After, the organic phase was dried with sodium sulphate, filtrated, and concentrated under vacuum. The crude product was then purified by column chromatography on silica gel using hexane/dichloromethane as the mobile phase.

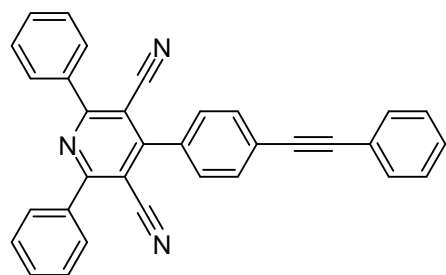


(E)-2,6-diphenyl-4-(4-styrylphenyl)pyridine-3,5-dicarbonitrile: White-yellow solid. mp = 262 – 263 °C. 35% yield. ¹H NMR (400 MHz, CDCl₃) δ 8.18 – 8.11 (m, 4H), 7.81 (d, *J* = 8.3 Hz, 2H), 7.74 – 7.68 (m, 2H), 7.68 – 7.59 (m, 8H), 7.46 (t, *J* = 7.5 Hz, 2H), 7.39 – 7.34 (m, 1H), 7.31 (d, *J* = 3.8 Hz, 1H), 7.23 (d, *J* = 12.2 Hz, 1H). ¹³C NMR (101 MHz, CDCl₃) δ (ppm) 163.5, 160.2, 140.4, 136.9, 136.6, 132.4, 131.5, 131.4, 129.7, 129.6, 128.9, 128.3, 127.5, 127.2, 126.9, 116.2, 105.9. HRMS (*m/z*) calculated for (M+H)⁺: 460.5473, found: 460.1835.

4.2.4. Synthesis of PPC derivative *via* Sonogashira cross-coupling.

An oven-dried screw-capped Schlenk flask was evacuated, back-filled with nitrogen and loaded with Br-PPC (110mg, 0.25 mmol), phenylacetylene (0.27 mmol; 28 mg), Pd(OAc)₂ (1 mol%; 0.56 mg), PPh₃ (2 mol%; 1.31 mg), CuI (2 mol%; 0.95 mg) N(Et)₃ (0.47 mmol, 62.5 μL) and degassed TFH (1 mL). The reaction was stirred at 80 °C for 18 h and allowed to cool down to room temperature. The mixture was then diluted with dichloromethane (10 mL) and washed with water (3 × 5 mL). After, the organic phase was dried with sodium sulphate, filtrated, and concentrated under vacuum. The crude product was then purified by column chromatography on silica gel using hexane/dichloromethane as the mobile phase. Nevertheless, purification by column chromatography was

challenging due to the slight difference in R_f between the brominated starting material and the desired product.



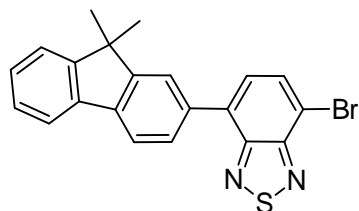
2,6-diphenyl-4-(4-(phenylethynyl)phenyl)pyridine-3,5-dicarbonitrile:
White-yellow impure solid. 57% raw yield.

PA-PPC

4.3. Synthesis of FL-BTD derivatives

4.3.1. Synthesis of BTD intermediates.

For the synthesis of FL-BTD-Br intermediate, oven-dried screw-capped Schlenk flask was evacuated, back-filled with nitrogen and loaded with 4,7-dibromo-2,1,3-benzothiadiazole (diBr-BTD) (150 mg, 0.51 mmol), Pd(OAc)₂ (0.56 mg, 2.5 × 10⁻³ mmol), PPh₃ (1.31 mg, 4.9 × 10⁻³ mmol), K₂CO₃ (23.49 mg, 0.17 mmol), 9-dimethyl-9H-fluoren-2-yl boronic acid (40.5 mg, 0.17 mmol), degassed ethanol (1.5 mL) and degassed toluene (1.5 mL). The reaction was stirred for 5h at 70 °C, after the reaction time, was allowed to cool down to room temperature. The solid was washed with dichloromethane (3 × 5 mL) and the solution containing the product was concentrated under reduced pressure. The crude product was then purified by column chromatography on silica gel using hexane/dichloromethane as the mobile phase.

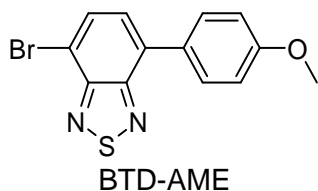


FL-BTD-Br

4-bromo-7-(9,9-dimethyl-9H-fluoren-2-yl)-2,1,3-benzothiadiazole: Green solid. mp: 126 – 129 °C. 86% yield. ¹H NMR (400 MHz, CDCl₃) δ (ppm) 7.99 – 7.84 (m, 4H), 7.83 – 7.75 (m, 1H), 7.65 (d, J = 7.6 Hz, 1H), 7.52 – 7.45 (m, 1H), 7.43 – 7.31 (m, 2H), 1.57 (s, 6H).

BTD-AME and BTD-OME intermediates were prepared as previously reported.^{82,98} To synthesize BTD-AME, an oven-dried screw-capped

Schlenk flask was evacuated, back-filled with nitrogen and loaded with diBr-BTD (588 mg, 2 mmol), Pd(OAc)₂ (44.9 mg, 0.2 mmol), PPh₃ (104.9 mg, 0.4 mmol), K₂CO₃ (553 mg, 4 mmol), 4-methoxyphenylboronic acid (304 mg, 2 mmol), degassed THF (5 mL) and degassed toluene (5 mL). The reaction was stirred for 5h at 70 °C, after the reaction time, was allowed to cool down to room temperature. The solid was washed with ethyl acetate (3 × 5 mL) and the solution containing the product was concentrated under reduced pressure. The crude product was then purified by column chromatography on silica gel using hexane/ethyl acetate as the mobile phase.

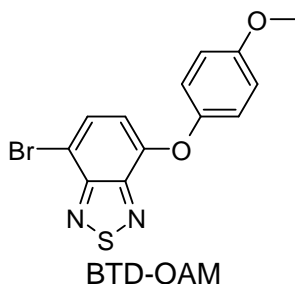


4-bromo-7-(4-

methoxyphenyl)benzo[c][1,2,5]thiadiazole:

Yellow solid. 57% yield. ¹H RMN (400 MHz, CDCl₃) δ (ppm.) 7.90 (d, *J* = 7.7 Hz, 1H), 7.86 (d, *J* = 8.8 Hz, 2H), 7.52 (d, *J* = 7.9 Hz, 1H), 7.06 (d, *J* = 8.8 Hz, 2H), 3.89 (s, 3H).

For the synthesis of BTD-OAM, a screw-capped Schlenk flask was evacuated, back-filled with nitrogen and charged with diBr-BTD (1.00 mmol, 294 mg), 4-methoxyphenol (2.0 mmol, 248 mg), K₂CO₃ (3.0 mmol, 415 mg) and DMF (6.5 mL). The reaction was stirred at 100 °C for 24 h then allowed to cool down to room temperature. The mixture was diluted with 10 mL of water and extracted with ethyl acetate (3 x 15 mL). The combined organic layers were dried over sodium sulphate, filtered, concentrated under reduced pressure, and purified by column chromatography on silica gel using hexane/ethyl acetate as the mobile phase.

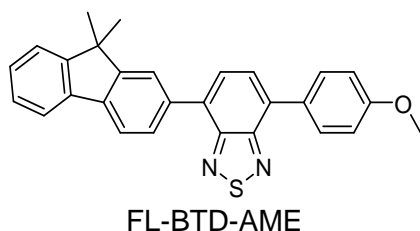


4-(4-methoxyphenoxy)-7-bromobenzo[c]

[1,2,5]thiadiazole: Yellow solid. mp: 120 – 122 °C. 33% yield. ¹H NMR (400 MHz, CDCl₃) δ (ppm.) 7.66 (d, *J* = 8.1 Hz, 1H), 7.13 (d, *J* = 9.1 Hz, 2H), 6.96 (d, *J* = 9.1 Hz, 2H), 6.60 (d, *J* = 8.1 Hz, 1H), 3.84 (s, 3H). ¹³C NMR (101 MHz, CDCl₃) δ (ppm) 157.1, 154.4, 150.7, 148.1, 147.8, 132.2, 121.7, 115.2, 111.4, 105.8, 55.7.

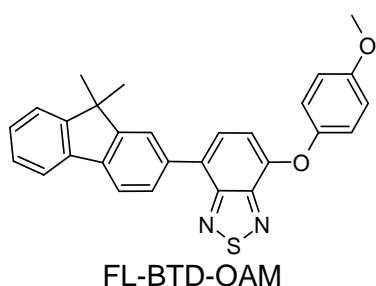
4.3.2. Synthesis of FL-BTD derivatives *via* Suzuki cross-coupling.

Oven-dried screw-capped Schlenk flasks were evacuated, back-filled with nitrogen and loaded with BTD-AME (50 mg, 0.16 mmol) to produce FL-BTD-AME and BTD-OAM (54 mg, 0,16 mmol) to produce FL-BTD-OAM, as well as Pd(OAc)₂ (0.56 mg, 2.5 × 10⁻³ mmol), PPh₃ (1.31 mg, 4.9 × 10⁻³ mmol), K₂CO₃ (23.49 mg, 0.17 mmol), 9-dimethyl-9H-fluoren-2-yl boronic acid (43 mg, 0.16 mmol), degassed ethanol (1.5 mL) and degassed toluene (1.5 mL). The reactions were stirred for 5h at 75 °C, and after the reaction time, were allowed to cool down to room temperature. The solids were washed with ethyl acetate (3 × 5 mL) and the solutions containing the products were concentrated under reduced pressure. The crude products were then purified by column chromatography on silica gel using hexane/ethyl acetate as the mobile phase.



4-(9,9-dimethyl-9H-fluoren-2-yl)-7-(4-methoxyphenyl)benzo[c][1,2,5]thiadiazole

: Green solid. mp: 189 – 191 °C. 62% yield. ¹H NMR (400 MHz, CDCl₃) δ 8.07 – 7.92 (m, 4H), 7.89 (d, *J* = 7.8 Hz, 1H), 7.85 (d, *J* = 7.3 Hz, 1H), 7.83 – 7.73 (m, 2H), 7.49 (dd, *J* = 6.0, 2.1 Hz, 1H), 7.37 (dd, *J* = 7.3, 3.6 Hz, 2H), 7.10 (d, *J* = 8.8 Hz, 2H), 3.91 (s, 3H), 1.59 (s, 6H). ¹³C NMR (101 MHz, CDCl₃) δ (ppm) 159.5, 159.0, 159.0, 157.2, 150.7, 137.2, 136.2, 134.2, 130.6, 130.5, 128.5, 128.12, 127.8, 127.4, 127.3, 127.2, 126.9, 125.3, 124.7, 124.3, 124.2, 113.1, 56.0, 49.6, 26.7. HRMS (*m/z*) calculated for (M+H)⁺: 435.5594, found: 435.1548.

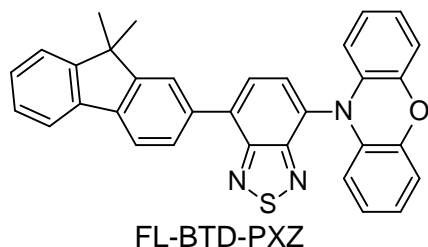


4-(4-methoxyphenoxy)-7-(9,9-dimethyl-9H-fluoren-2-yl)benzo[c][1,2,5]thiadiazole:

Green solid. mp: 124 – 126 °C. 95% yield. ¹H NMR (400 MHz, CDCl₃) δ 7.93 (s, 1H), 7.91-7.82 (m 7.9 Hz, 2H), 7.78 (d, *J* = 6.4 Hz, 1H), 7.62 (d, *J* = 7.8 Hz, 1H), 7.47 (d, *J* = 6.5 Hz, 1H), 7.41-7.31 (m, 2H), 7.19 (d, *J* = 8.9 Hz, 2H), 6.98 (d, *J* = 8.9 Hz, 2H), 6.83 (d, *J* = 7.8 Hz, 1H), 3.86 (s, 3H), 1.56 (s, 6H). ¹³C NMR (101 MHz, CDCl₃) δ (ppm) 157.7, 157.2, 156.5, 150.7, 150.2, 143.3, 143.2, 137.2, 136.2, 134.2, 128.1, 127.8, 127.3, 126.9, 126.8, 124.9, 124.9, 124.3, 124.2, 120.0, 114.8, 56.0, 49.1, 26.8. HRMS (*m/z*) calculated for (M+H)⁺: 451.5589, found: 451.1472.

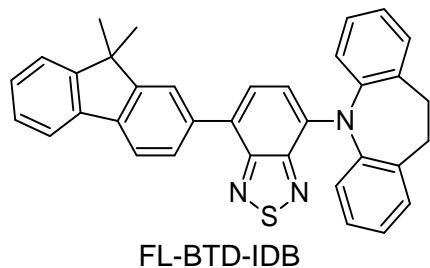
4.3.3. Synthesis of FL-BTD derivatives via Buchwald-Hartwig amination

An oven-dried screw-capped Schlenk flask was evacuated, backfilled with nitrogen and loaded with FL-BTD-Br (100 mg, 0.25 mmol), phenoxazine or iminodibenzyl (0.37 mmol), Pd(OAc)₂ (2.25 mg, 0.01 mmol), tri-tert-butylphosphonium tetrafluoroborate (8.7 mg, 0.03 mmol), sodium tert-butoxide (36 mg, 0.37 mmol) and anhydrous toluene (2 mL). The reactions were stirred at 110 °C for 24h and allowed to cool down to room temperature. The mixtures were diluted with dichloromethane (30 mL) and washed with water. The organic fraction was dried over sodium sulphate, filtrated and concentrated under vacuum. The crude products were purified by column chromatography on silica gel using hexane/ethyl acetate as the mobile phase.



FL-BTD-PXZ

10-(7-(9,9-dimethyl-9H-fluoren-2-yl)benzo[c][1,2,5]thiadiazol-4-yl)-10H-phenoxazine: Red solid. mp: 142 – 144 °C. 79% yield. ¹H NMR (400 MHz, CDCl₃) δ 8.08 (d, *J* = 1.2 Hz, 1H), 8.04 (dd, *J* = 7.9, 1.6 Hz, 1H), 7.94 (dd, *J* = 7.6, 5.8 Hz, 2H), 7.87 – 7.78 (m, 2H), 7.54 – 7.48 (m, 1H), 7.44 – 7.35 (m, 2H), 6.80 (dd, *J* = 7.9, 1.4 Hz, 2H), 6.71 (td, *J* = 7.7, 1.4 Hz, 2H), 6.58 (td, *J* = 7.8, 1.5 Hz, 2H), 5.92 (dd, *J* = 8.0, 1.3 Hz, 2H), 1.62 (s, 6H). ¹³C NMR (101 MHz, CDCl₃) δ (ppm) 155.4, 154.1, 154.1, 152.9, 144.1, 140.0, 138.6, 135.9, 135.6, 133.5, 132.9, 129.4, 128.5, 127.9, 127.7, 127.1, 123.7, 123.2, 122.7, 121.9, 120.4, 120.2, 115.8, 113.3, 47.1, 27.2. HRMS (*m/z*) calculated for (M+H)⁺: 510.6276, found: 510.1660.



4-(10,11-dihydro-5H-dibenzo[b,f]azepin-5-yl)-7-(9,9-dimethyl-9H-fluoren-2-yl)benzo[c][1,2,5]thiadiazole: Orange solid. mp: 163 – 164 °C. 39% yield. ¹H NMR (400 MHz, CDCl₃) δ 7.95 – 7.88 (m, 2H), 7.84 (d, *J* = 7.9 Hz, 1H), 7.77 (m, 1H), 7.59 (d, *J* = 8.0 Hz, 1H), 7.54 – 7.45 (m, 3H), 7.41 – 7.30 (m, 2H), 7.28 (m, 6H), 6.81 (d, *J* = 8.0 Hz, 1H), 3.14 (s, 4H), 1.57 (s, 6H). ¹³C NMR (101 MHz, CDCl₃) δ (ppm) 163.8, 157.2, 150.7, 144.8, 143.2, 137.2, 136.2, 135.7, 134.2, 132.3, 130.6, 129.8, 129.4, 128.4, 128.4, 128.1, 127.8, 127.3, 126.9, 125.9, 124.9, 124.2, 124.2, 49.6, 34.6, 26.66. (m/z) calculated for (M+H)⁺: 522.6813, found: 522.2016.

4.4. Preparation of solutions for spectrophotometric analysis

4.4.1. Absorption analysis

For the UV-Vis analyses of the synthesized PPC and FL-BTD derivatives, stock solutions were prepared in THF at a concentration of 5×10^{-4} mol L⁻¹. To analyze the absorption maxima and the solvatochromic effect, dilutions were prepared, using different solvents (toluene, tetrahydrofuran - THF, chloroform, dichloromethane - DCM, acetonitrile, ethanol, methanol, DMF and DMSO) at a concentration of 5×10^{-5} mol L⁻¹. For the molar absorptivity analysis, solutions with different concentrations were prepared in THF ($1, 2, 3, 4$ and 5×10^{-5} mol L⁻¹) to obtain a calibration curve where the gradient of the linear plot provides the molar absorptivity.

4.4.2. Emission analysis

To analyze the emission maxima and the solvatochromic effect, dilutions were prepared, using different solvents (toluene, tetrahydrofuran - THF, chloroform, dichloromethane - DCM, acetonitrile, ethanol, methanol, DMF and DMSO) at concentrations of between 1.0×10^{-7} and 2.5×10^{-6} mol L⁻¹. Subsequently, the emission measurements for the prepared solutions were performed.

4.4.3. Fluorescence quantum yield

Determination of fluorescence quantum yields in solution was made by the comparative method using Equation 4. Solutions were prepared in THF using concentrations between 1.0×10^{-7} and 2.5×10^{-6} mol L⁻¹. Fluorescein sodium salt solutions (1.0×10^{-7} and 2.5×10^{-6} mol L⁻¹) were prepared in NaOH (0.1 mol L⁻¹) and used as the standard solution with fluorescence quantum efficiency of 0.93.⁹⁹

$$\phi_x = \phi_{St} \left(\frac{Grad_x}{Grad_{St}} \right) \left(\frac{\eta_x^2}{\eta_{St}^2} \right) \quad (4)$$

In Equation 4, subscripts St and x denote standard and test, respectively, ϕ is the fluorescence quantum yield, Grad is the gradient from the plot of integrated fluorescence intensity vs absorbance and η the refractive index of the solvent.

4.4.4. Aggregation-induced enhanced emission (AIEE)

Stock solutions in THF at a concentration of 5×10^{-4} mol L⁻¹ were used to prepare twelve dilutions in THF/water with increasing water fractions (f_w) ranging from 0 to 99%, as shown in Table 3. To avoid bubble formation water was slowly added as the last component of the dilutions and then mixture the solvents manually. The final concentration for each dilution was 5×10^{-6} mol L⁻¹ and the emission measurements were made the same day of their preparation to avoid changes in the emission for each f_w due to possible instability of the nano-aggregates.

Table 3. Preparation of solutions for AIEE analyses

% f_w	μl stock sol.	mL THF	mL water	V Total
00	50	5,0	0,0	5,0
20	50	4,0	1,0	5,0
30	50	3,5	1,5	5,0
40	50	3,0	2,0	5,0
50	50	2,5	2,5	5,0
60	50	2,0	3,0	5,0
70	50	1,5	3,5	5,0
80	50	1,0	4,0	5,0
85	50	0,7	4,3	5,0
90	50	0,5	4,5	5,0
95	50	0,2	4,8	5,0
99	50	0,0	5,0	5,0

4.5. OLED fabrication

The OLED structure consisted of an Indium Tin Oxide (ITO) covered glass substrate where 2 nm of molybdenum trioxide (MoO_3) were evaporated via thermal deposition to improve charge injection, followed by 20 nm of N,N0-bis(naphtalen-2-yl)-N,N0-bis(phenyl) benzidine (β -NPB) used as a hole-transporting layer. The emitting layer consisted of 30 nm of Bis-4-(N-carbazolyl)phenyl)phenylphosphine oxide (BCPO) used as host and 30 nm of FL-BTD-OAM. After that 40 nm of bathophenanthroline (BPhen) was deposited as an electron-transporting layer and, finally, a 0.1 nm thick Lithium Fluoride (LiF) followed by a 150 nm thick aluminium layer was evaporated to form the cathode. All materials were bought from Lumtec (Luminescence Technology Corp.) besides Lithium fluoride (LiF) from Sigma Aldrich and used without any further purification. After the OLED fabrication, the devices were carefully encapsulated inside a glove box with a controlled nitrogen atmosphere using a glass lid with UV-curing epoxy. The electroluminescent spectra were measured using a PTI fluorimeter model QuantaMaster 40, while the JxV curves were measured by using a

Keithley source meter model 2400. The device's Luminance was measured with a luminance meter Konica Minolta model LS-100. All measurements were carried out with the encapsulated samples at room temperature and room atmosphere at LOEM – PUC Rio.

Chapter 5. Pyridine-3,5-dicarbonitrile derivatives

5.1. Molecular design and synthesis

Bearing in mind the outstanding results of D- π -A PCNs as TADF materials, as well as the importance of the development of compounds that associate both TADF and AIE (or AIEE) properties, we design novel D- π -A biaryl-PPCs. The architecture of these compounds was based on the insertion of bulky substituents on the terminal aryl ring aiming at twisted structures. In terms of TADF development, the non-coplanarity tends to provide a concentration of HOMO on the donor group and LUMO over the acceptor unit, which leads to a decrease in the ΔE_{ST} , favouring RISC. Regarding AIE/AIEE luminogens development, the role of the bulky substituent is to provide a twisted structure that avoids p-p stacking in the solid/aggregate state and consequently hampers non-radiant channels of deactivation. In this sense, the PPCs 2M-PPC, MT-PPC, BP-PPC and FL-PPC possessing 2-toluy, dimethylmethoxyaryl, 2-biaryl and dimethylfluorene groups, respectively, were proposed. In addition, the insertion of styryl and alkynyl groups was also proposed since the presence of these groups led to AIEE properties in previously described compounds.^{17,100}

The synthesis of the proposed PPC derivatives was performed via a two-step methodology. First, a multicomponent Hantzsch reaction was employed for the construction of the acceptor PPC moiety, After C-C cross-coupling reactions (Suzuki, Heck and Sonogashira) were applied for the insertion of the donor units.

For the Hantzsch reaction, a one-pot condensation between 4-bromobenzaldehyde, two equivalents of benzoyl-acetonitrile, and ammonium acetate was performed. The starting materials were dissolved in degassed glacial acetic acid and the mixture was stirred at 120°C for 12h. In the sequence, the temperature was reduced to 70°C, and the resulting dihydropyridine was oxidized using sodium nitrite, affording the brominated

intermediate, 4-(4-bromophenyl)-2,6-diphenylpyridine-3,5-dicarbonitrile (Br-PPC), in 92% yield of (Scheme 2).

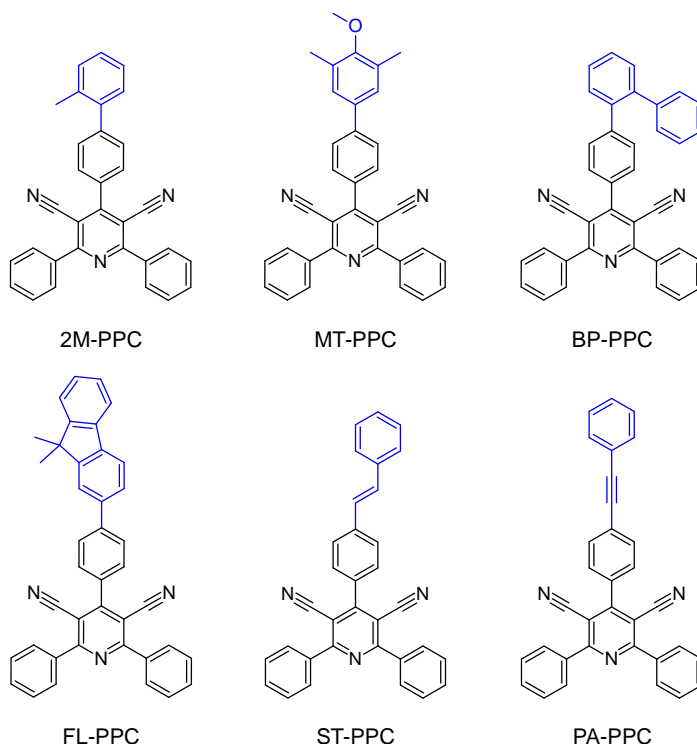
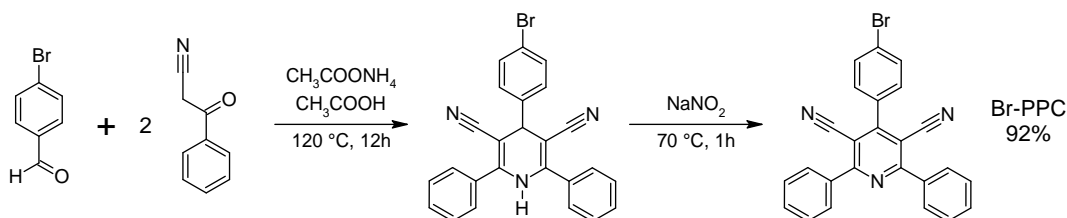


Figure 16. D- π -A-type PPC derivatives designed and synthesized.



Scheme 2. Synthesis of the intermediate 4-(4-bromophenyl)-2,6-diphenylpyridine-3,5-dicarbonitrile (Br-PPC)

Br-PPC was characterized *via* ^1H and ^{13}C NMR and high-resolution mass spectrometry (HRMS). To illustrate the structural characterization of this intermediate, the ^1H NMR spectrum is depicted in Figure 17. The multiplets at 8.01 – 8.12 ppm, integrating for four hydrogens, and at 7.64 – 7.54, integrating for six hydrogens are related to phenyl groups at positions 2 and 6 of pyridine. The signals from the bromoarene are observed as two coupled doublets ($J = 8.5$ Hz) at 7.78 and 7.51 ppm. Moreover, the absence

of the CH signal typically observed in dihydropyridines, indicates that oxidation was achieved.

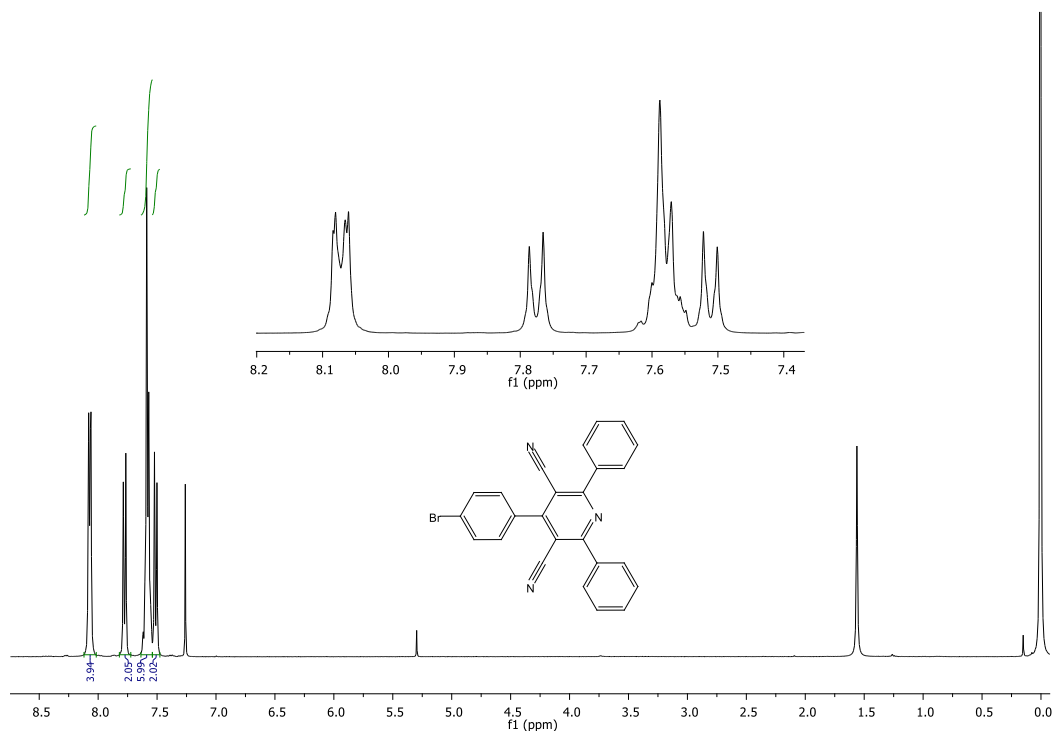
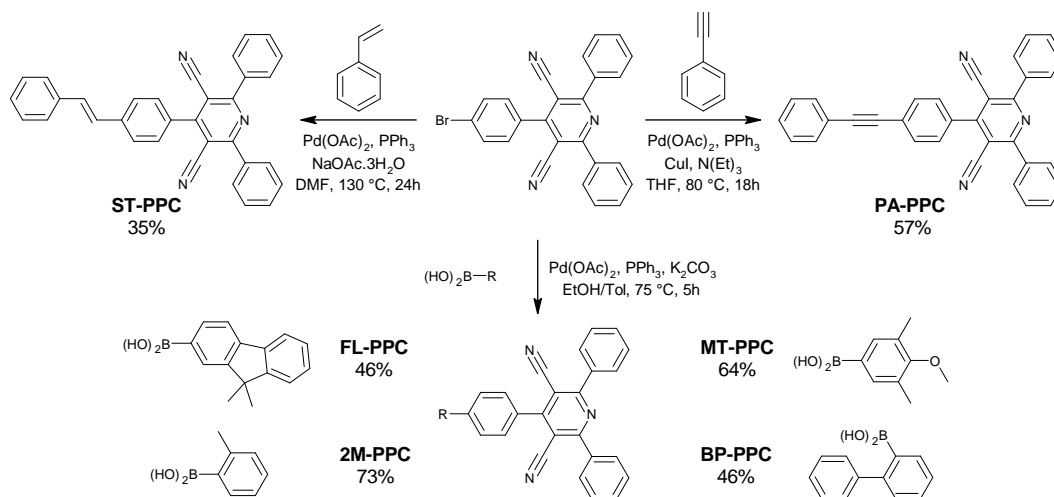


Figure 17. ¹H NMR spectrum of Br-PPC (400 MHz, CDCl₃).

Afterwards, the Br-PPC substrate was submitted to Suzuki reactions, using dimethyl-fluorenyl-, 2-tolyl- methoxydimethylphenyl- and 2-biphenyl-boronic acids. The reaction was carried out using conditions previously optimized by our group and reported in the literature,^{82,84,98,100–103} affording the target fluorophores 2M-PPC, BP-PPC, FL-PPC and MT-PPC in 46 to 73% yields. Scheme 3 shows the synthetic routes. In addition, the brominated substrate was also submitted to classical Heck and Sonogashira coupling conditions with styrene and phenylacetylene, providing ST-PPC and PA-PPC in 35 and 57% yields, respectively (Scheme 3).



Scheme 3. Synthetic routes of the new PPC derivatives.

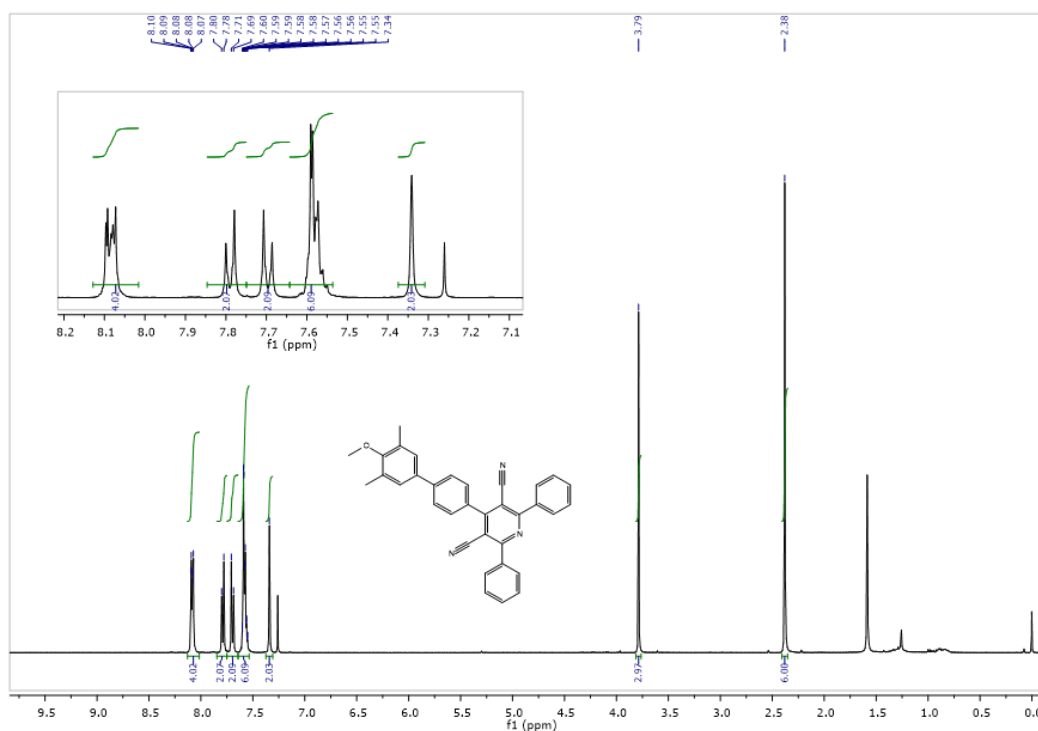


Figure 18. ^1H NMR spectrum of MT-PPC (400 MHz, CDCl_3).

The obtained PPC derivatives were characterized using NMR and HRMS. In addition, X-ray structures of BP-PPC and FL-PPC were obtained, and these data are discussed in the section related to AIEE. To illustrate the structural characterization of these compounds, the ^1H NMR spectrum of MT-PPC is shown in Figure 18. The two multiplets at 8.13 – 8.02 ppm and 7.64 – 7.54 are related to phenyl groups at positions 2 and 6 of pyridine.

The coupled doublets ($J = 8.5$ Hz) at 7.79 and 7.70 ppm are related to the hydrogens of the bridge aryl group. The singlets at 7.34 (2Hs), 3.79 (3Hs) and 2.38 ppm (6Hs) are related to ortho positions of the terminal aryl, methoxy group and methyl groups, respectively.

5.2. Theoretical simulations

Estimations to calculate the properties of ground state (S_0) and first singlet (S_1) and triplet (T_1) excited states were made using DFT and TD-DFT, under B3LYP/6-31G(d,p). In addition to energy levels, DFT can also provide the HOMO/LUMO distribution over donor/acceptor groups, which can give insights concerning the potential of the compounds to display TADF properties (Table 4). The estimation pointed out HOMO ranging from -6.23 eV to -5.60 eV and LUMO between -2.29 and -2.26 eV, which led to E_{gap} values from 3.34 to 3.95 eV. All these energy levels indicated that these compounds are suitable for application as emissive layers in OLEDs^{11,56,87}. Additionally, calculations for the optimized structures show large distortion angles between PPC unit and donor substituents, as well as localized orbital distributions, with LUMO concentrated on the PPC acceptor and HOMO mainly located on donor moieties, with a small portion on the benzene bridge which may be attributed to the electron-withdrawing character of the PPC acceptor. These results show a clear separation of the frontier orbitals achieved in the PPC derivatives (Figure 19).

Table 4. Theoretical simulation data in eV for PPC derivatives.

	HOMO	LUMO	E_{gap}	E_S	E_T	DE_{ST}
2M-PPC	-6.23	-2.28	3.95	3.49	2.92	0.58
BP-PPC	-5.91	-2.27	3.64	3.23	2.91	0.32
FL-PPC	-5.60	-2.26	3.34	3.00	2.84	0.16
MT-PPC	-5.87	-2.23	3.64	3.22	2.94	0.28
PA-PPC	-5.79	-2.29	3.50	3.09	2.73	0.36
ST-PPC	-5.67	-2.26	3.41	3.00	2.44	0.56

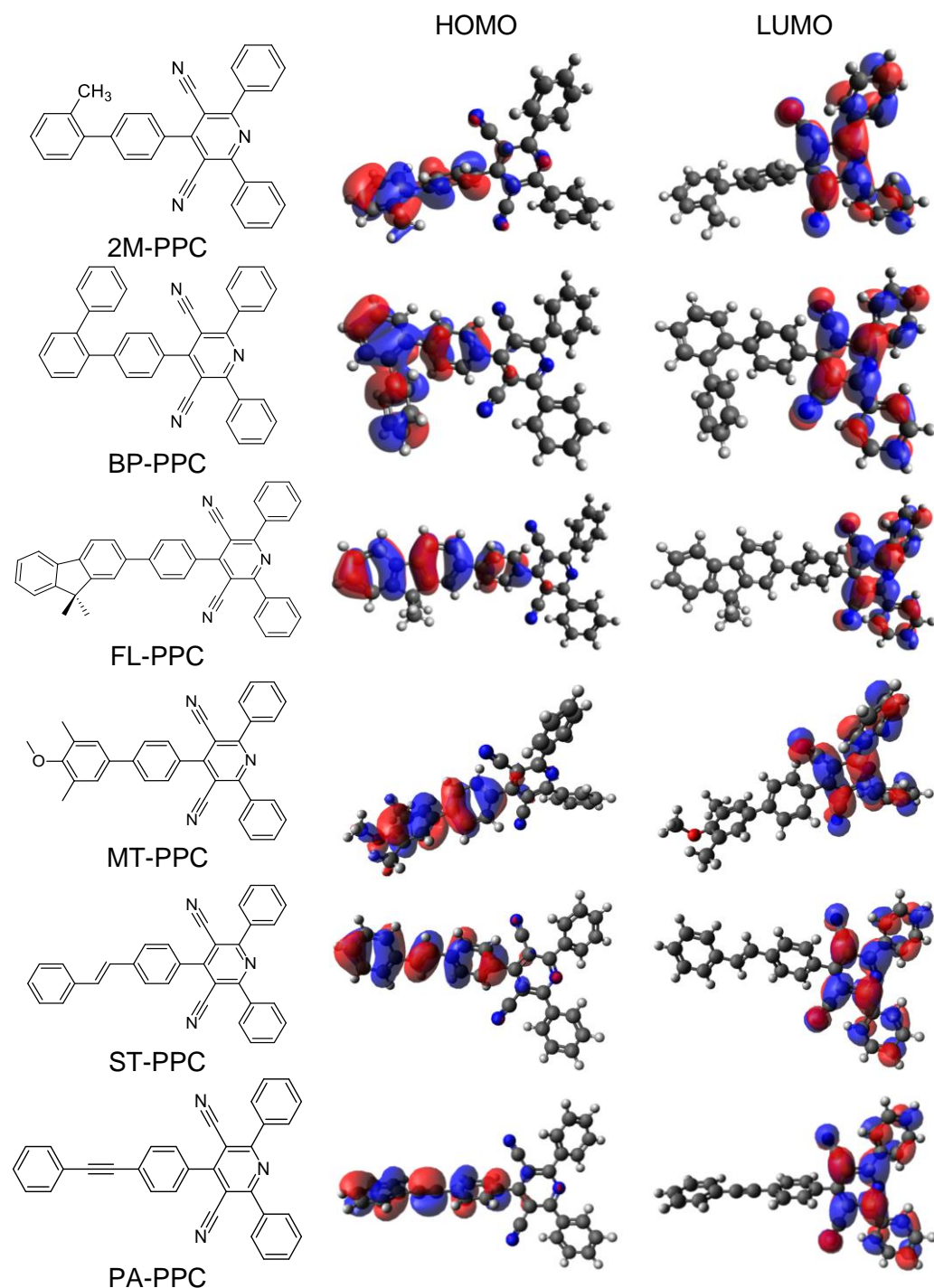


Figure 19. The HOMO and LUMO distribution from DFT calculations of PPC derivatives.

Energies of excitation state (S_1 and T_1) were obtained from TD-DFT calculations, values for singlet and triplet states ranged from 3.00 to 3.49 and 2.44 to 2.94 eV, respectively, leading to ΔE_{ST} values from 0.16 to 0.58 eV. These values for PPC derivatives are within the ΔE_{ST} range to present

efficient ISC and RISC, especially for FL-PPC. Reported PPC TADF derivatives with outstanding results, registered ΔE_{ST} from 0.01 up to 0.5 eV,^{11,56} thus, is reasonable to expect high fluorescence quantum yields and delayed fluorescence for our compounds.

5.3. Photophysical properties

Photophysical characterization in solution was made in different organic solvents (chloroform, DMF, DMSO, ethanol, methanol, and toluene). The UV-vis absorption and fluorescence spectra of the PPC derivatives were recorded at room temperature using concentrations of 5×10^{-5} mol L⁻¹ and $1 - 5 \times 10^{-6}$ mol L⁻¹, respectively. Detailed photophysical characterization has been carried out for the compounds obtained *via* Suzuki cross-coupling. The ST-PPC derivative is still under characterization and PA-PPC requires further purification or, if necessary, a different synthetic route to allow its correct isolation. The corresponding spectra for 2M-PPC, BP-PPC, FL-PPC and MT-PPC are shown in Figure 20 and relevant data from the photophysical characterization is summarized in Table 5.

PPCs presented intense absorptions in the UV region, with maxima between 277 and 294 nm and molar absorption coefficient in the order of 10^4 cm⁻¹mol⁻¹L, corresponding to allowed p→p* transitions. A small solvatochromic effect was observed ($\Delta\lambda_{abs} = 5-14$ nm) which indicated an almost absent charge-transfer character in the ground state.

Table 5. Photophysical data for PPC derivatives in solution.

	PPC	2M	FL	MT	BP
λ_{abs} (nm)	Toluene	289	287/314*	294	290
	THF	289	287/314*	294	290
	Chloroform	291	286	287	285
	DCM	286	283	282	278
	Ethanol	285	282	285	272
	Methanol	277	282	280	278
	DMF	-	-	-	-
	DMSO	-	-	-	-
$\Delta\lambda_{\text{abs}}$ (nm)		14	5	14	12
ϵ_{THF} (cm ⁻¹ mol ⁻¹ L)		34849	37578/37239	39345	36511
ϵ_{DCM} (cm ⁻¹ mol ⁻¹ L)		41200	62615	54178	115776
λ_{em} (nm)	Toluene	407/445	451	480	430
	THF	410	460	504	433
	Chloroform	415	472	498	440
	DCM	427	474	525	452
	Ethanol	441	503	438/498 ^a	467
	Methanol	451	504	426/530 ^a	478
	DMF	453	500	430/522 ^a	477
	DMSO	433	505	-	455
$\Delta\lambda_{\text{em}}$ (nm)		46	54	99	48
$\Delta\lambda_{\text{ST}}$ (nm)	Toluene	118	164	186	140
	THF	121	173	210	143
	Chloroform	124	186	211	155
	DCM	141	191	243	174
	Ethanol	156	221	153	195
	Methanol	174	222	146	200
ϕf	Toluene	0.01	0.71	0.30	0.24
	THF	0.02	0.18	0.02	0.11

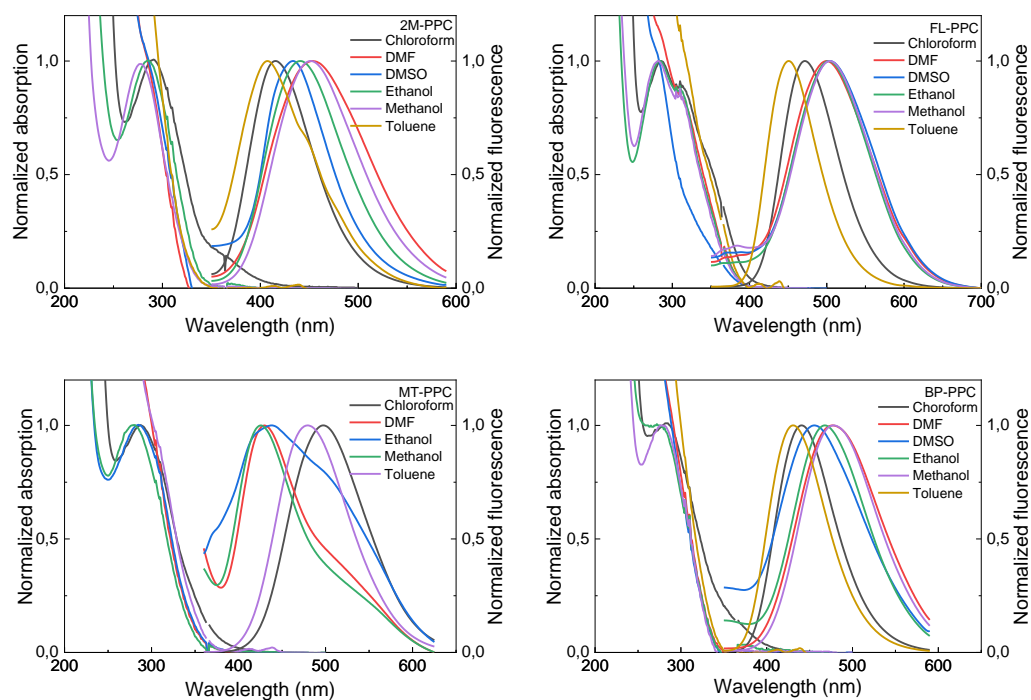


Figure 20. UV-vis absorption and fluorescence spectra in solution using different organic solvents of the PPC derivatives.

On the other hand, MT-PPC displayed a distinct emission profile. In less-polar environments (toluene, THF, chloroform and DCM), only one emission maximum is observed between 480 and 525 nm. However, in addition to this band, in highly polar solvents (ethanol, methanol and DMF), a blue-shifted band is also observed from 426 to 438 nm, with the original emission appearing as a shoulder. Bearing in mind the structure of this compound, in which donor and acceptor groups are linked by sigma bonds, the existence of a twisted intramolecular charge-transfer excited state (TICT) is suggested. In this case, when the fluorophore absorbs one photon, a planar locally excited (LE) state is formed. However, the steric hindrance of bulky substituents (meta-CH₃ groups) facilitates intramolecular D-A twisting around the sigma bond, producing a relaxed perpendicular structure. The dual emission is, therefore, due to an equilibration between a relaxed perpendicular conformer (TICT) and a coplanar conformer (LE). As the perpendicular conformation is more stabilized it is related to the redshifted emission whereas the coplanar counterpart emits a more energetic transition. Fluorescence quantum yields were determined for all

PPCs in toluene and THF and values between 0.01 and 0.71 were observed. Clearly, the modification of the terminal aryl groups dramatically changes the intensity of the fluorescence emission. The lower ϕ_f values were observed for 2M-PPC, whereas the most emissive compound was FL-PPC, indicating the positive effect of the fluorenyl group and the negative effect of the 2-toluy unit. In addition, with exception of 2M-PPC, higher ϕ_f values were observed in toluene than in THF. This is expected since, more polar solvents interact strongly with charged excited states, which favours non-radiant decays.

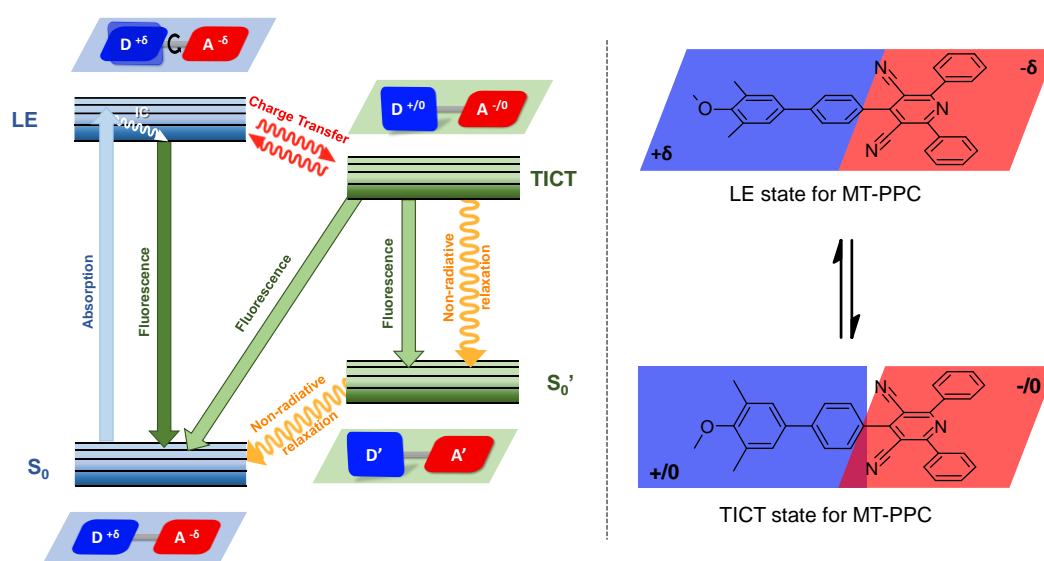


Figure 21. State diagram for suggested TICT/LE dynamics in MT-PPC.

Time-resolved fluorescence measurements were performed to evaluate the dynamics of the excited state of the PPCs, as well as evaluate the presence of two fluorescence decays (t_{prompt} and t_{delayed}), which is a characteristic of TADF emitters. The photoluminescence decay curves in THF are depicted in Figure 22 and t values along with, k_r and k_{nr} are displayed in Table 6. Decay curves in toluene are depicted in the appendix section. For all compounds, the photoluminescence decay fits as a monoexponential in the presence as well as in the absence of O_2 . Observed t values between 1.2 and 3.2 ns were determined in toluene and between 4.2 and 5.3 ns were observed in THF. The absence of a second decay in the ms scale (t_{delayed}) excludes the TADF behaviour for these compounds.

In addition, with exception of FL-PPC dissolved in toluene, all k_{nr} values were higher than the k_r . Time-resolved fluorescence decay for 2M-PPC was not measured due to its lower quantum yield.

Table 6. Time-resolved fluorescence data of the PPC derivatives.

Toluene	t_{prompt} (ns)	ϕ_f	k_r ($\times 10^8 \text{ s}^{-1}$)	k_{nr} ($\times 10^8 \text{ s}^{-1}$)
FL-PPC	1.7	0.707	4.2	1.7
MT-PPC	3.2	0.296	0.9	2.2
BP-PPC	1.2	0.246	2.1	6.3
TFH				
FL-PPC	4.2	0.183	0.4	1.9
MT-PPC	5.3	0.02	0.0	1.8
BP-PPC	4.2	0.112	0.3	2.1

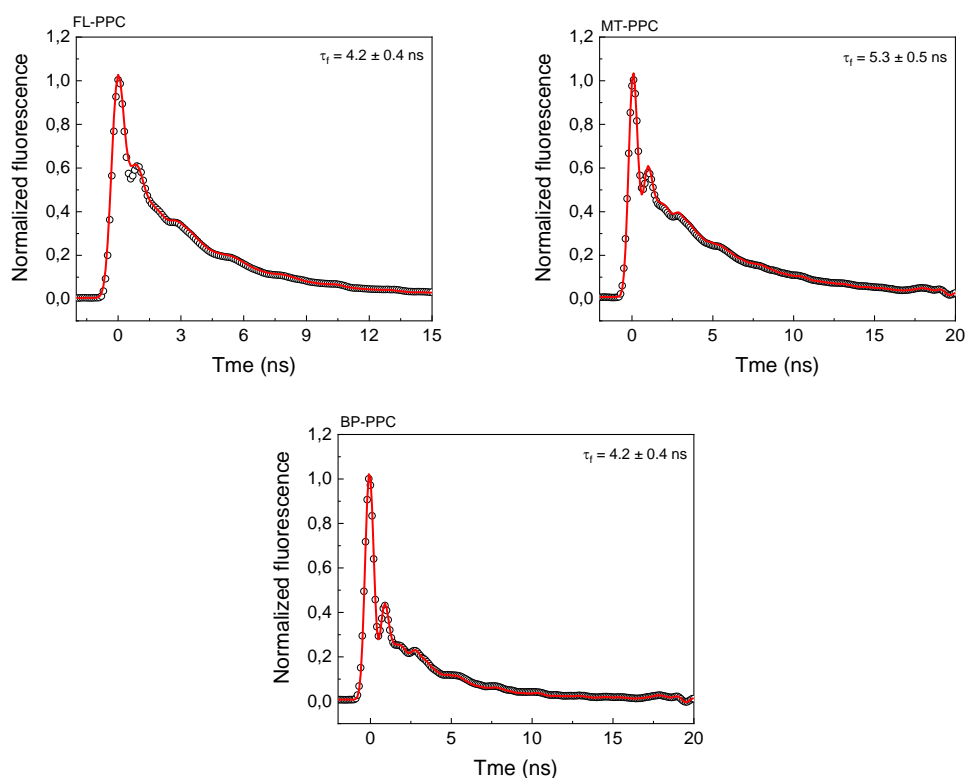


Figure 22. Fluorescence decays of PPC derivatives in THF.

5.4. Aggregation-induced enhanced emission (AIEE) properties

To validate the AIEE properties of the PPC derivatives, initially, preliminary visual tests were made. Emission profiles of the compounds with positive aggregation effect were studied in THF/water mixtures with the increase of the water fraction (f_w). The putative ACQ effect was studied as well. FL-PPC, MT-PPC and ST-PPC, presented positive AIEE, while BP-PPC, presented a negative effect, suggesting ACQ. 2M-PPC didn't show significant ϕ_f in the photophysical characterization nor AIE/AIEE effect in the visual test, hence, it was omitted for aggregate state emission measurements.

Figure 23 shows the results of the visual test. Aggregates are expected to be formed when the water content reaches a critical point. A clear enhancement in the fluorescence for the styryl-, dimethylmethoxyphenyl- and fluorenyl-substituted compounds can be observed when aggregation occurs. On the other hand, for the biphenyl-substituted BP-PPC, the opposite effect occurs, and the emission is quenched.

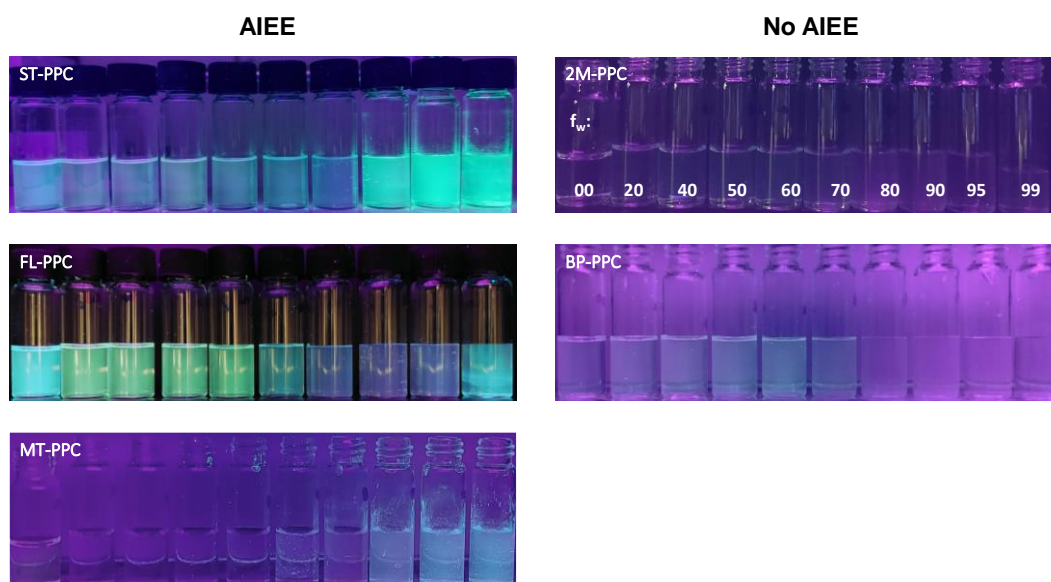


Figure 23. AIE/AIEE visual tests of the compounds in mixtures THF/water with different f_w

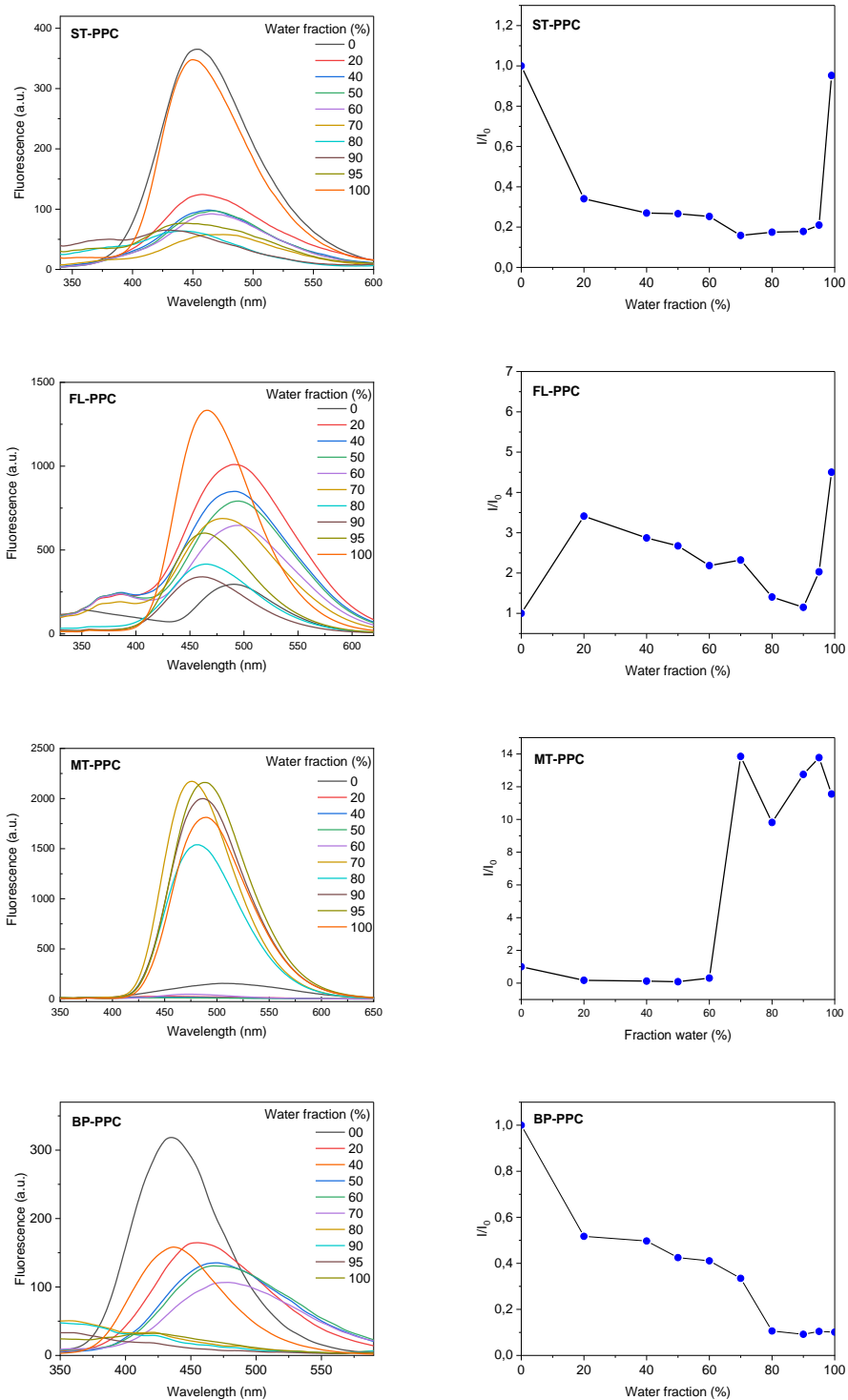


Figure 24. Fluorescence emission profile of the PPC derivatives in THF/water mixtures with different f_w (left) and their relative fluorescence intensity where I_0 is the intensity in pure THF.

Emission spectra (Figure 24) corroborate the results in the visual tests. As the f_w increases, a reduction in the fluorescence intensity occurs,

as well as minor alterations in the wavelength emission maxima, this can be attributed to the change in the solvent polarity, affecting the ICT process for the excited states. Once f_w reaches its critical point and the aggregates are formed, a significant increase in emission intensity is noted for ST-PPC, FL-PPC and MT-PPC. The effect can be better observed with the relation between the relative intensity (I/I_0) for each water fraction.

For ST-PPC, the aggregation effect is evident at 99 % f_w . The decline in the emission stops at 60%, and slightly rises before reaching the I/I_0 maxima, getting a relative intensity like its emission in pure THF. AIEE effect for FL-PPC and MT-PPC is larger, with an improvement of the relative intensity five and fourteen times, respectively. This behaviour can be attributed to the substituents in donor moieties that promote twisted conformations for the emitters in the nano-aggregates, in benefit of radiative decays.

ACQ was observed for the BP-PPC derivative, in which the emission deteriorates, first, due to polarity changes in the media, and then due to aggregate formation, until it is completely quenched at an I/I_0 value of 80% f_w . This can be attributed to a more planar conformation in the aggregated state, favouring non-radiative relaxations because of π - π stacking interactions.

DLS studies for aggregate formation were made by measuring the nano-aggregate's diameter before and after the I/I_0 maxima. The data obtained is displayed in Table 7. The general behaviour of aggregate size concerning f_w and I/I_0 can be noted. FL-PPC and ST-PPC show smaller diameters for aggregates formed in f_w with the highest I/I_0 ratio, implying enhancement of the emission in the most compact aggregates due to restriction of intramolecular motions (RIR and RIV). The poorer compactness of aggregates would still allow for energy consumption through intramolecular motion, which can be observed as a lower emission intensity in those f_w .

The size of the nanoaggregate would be reflected in the ACQ effect as well. For BP-PPC it is observed a drastic shrink in the diameter of aggregates at 80% f_w when the emission has been quenched. A decrease of 58% in size, greater than the decrease in the other particle sizes for FL-PPC (33%) and ST-PPC (28%), could suggest the preference of BP-PPC to form disk-like arrangements that would perform strong detrimental π - π stacking interactions.

This tendency in diameter size and emission is not observed in MT-PPC, where the contrary has a size increment of 15%.

Table 7. DLS measurements of nano-aggregate's size and aggregation effect.

PPC	Aggregation tests		Aggregation effect	DLS	
	Visual ^a	f_w ^b		f_w (%)	Z-Ave (d.nm)
2M		-	None	-	-
FL		99	AIEE	90	187
				95	188
				99	120
MT		70	AIEE	60	1778
				70	2101
BP		80	ACQ	70	1104
				80	465
ST		99	AIEE	80	440
				90	228
				99	162

^a f_w from left to right: 0, 20, 40, 50, 60, 70, 80, 90, 95, 99. ^b Fluorescence measurements. f_w (%) where an increase or decrease in fluorescence is observed.

Additional insights regarding the improvement or quenching in the emission of PPC derivatives in the aggregated state can be obtained from the crystal structure of FT-PPC and BP-PPC. Solid state structures for both compounds show nonplanar molecules, first in the PPC ring due to large steric hindrance induced by adjacent CN groups, then with the benzene

bridge and donor substituents due to the steric hindrance between the hydrogen atoms. Torsion angles between substituents and pyridine ring in the PCC core are 11.18° for BP-PCC, and a large dihedral angle of 62.63° for FL-PCC (Figure 25).

Packing structures with distance measurements between centroids and short contacts of compounds BP-PCC and FL-PCC are displayed in the appendix (A2). Stacking structures are formed with π - π interactions of 4.166 \AA for BP-PCC between the phenyl rings from 2,6- positions of the pyridine ring (PhPy) and the phenyl ring in the position 2 of the biphenyl substituent (Figure 25). For FL-PPC interactions between centroids are weaker (4.755 to 5.224 \AA), compared to BP-PPC. The shortest distances between the molecules and small torsion angle benefit the energy dissipation, favouring non-radiative channels of deactivation, thus, presenting the ACQ effect in BP-PPC.

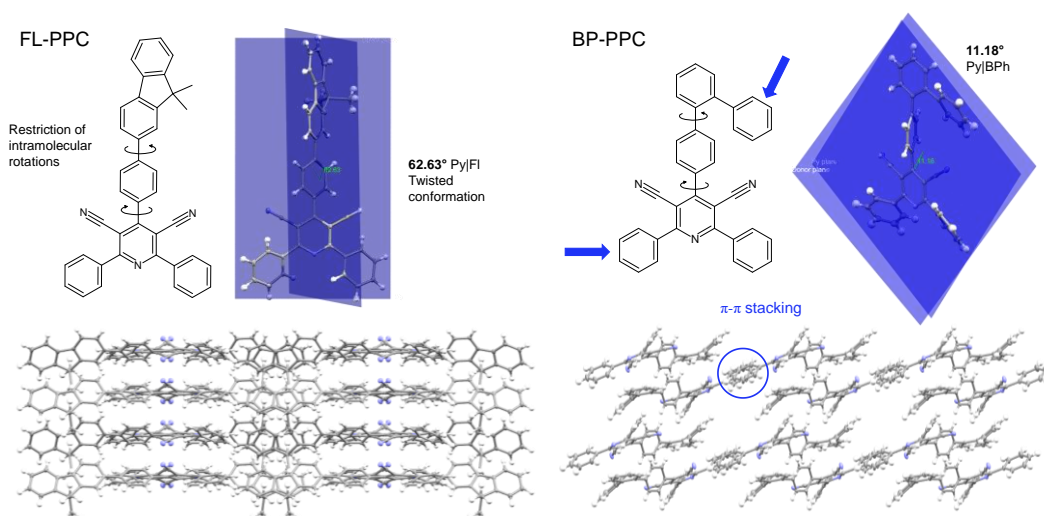


Figure 25. Molecular and single crystal structures (top) and packed crystal structures (bottom) of FL-PPC and BP-PPC

5.5. Partial Conclusions

In summary, the synthesis and photophysical characterization of biaryl-pyridyne-3,5-dicarbonitrile derivatives was described for the first time. Compounds presented absorption in the UV region (~ 280 - 300 nm) and cyan to green fluorescence. The inserted terminal aryl donor groups played a key

role in the photophysics of the compounds. The Fluorenyl group led to the more emissive PPC derivative in solution, whereas 2-toluyyl substitution provided a weakly emissive compound. MT-PPC presented interesting dual emission fluorescence, which was attributed to an equilibrium between LE and TICT excited states. None of the compounds presented TADF. Compounds FL-PPC, MT- PPC and ST- PPC presented aggregation-induced enhanced emission, with prominence for MT-PPC whose emission presented a 14-fold increase upon aggregation. Currently, the complete characterization of styryl-substituted ST- PPC and the evaluation of MT-PPC as an emissive layer in OLEDs is under development.

Chapter 6. Fluorenyl-BTD Derivatives

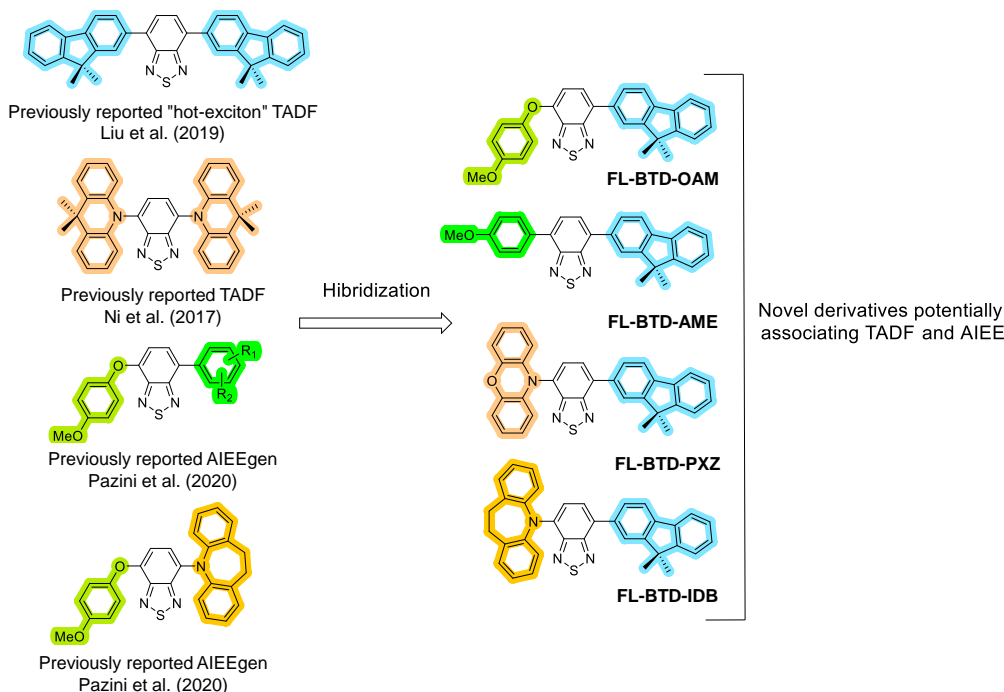
6.1. Molecular design and synthesis

Given the vast applications that BTD derivatives have in pure and applied sciences and considering that the scope of possibilities increases when properties such as TADF and AIE/AIEE are present in the fluorophores, we aimed to design molecules that exhibit both these properties. Therefore, a new series of D-A-D type molecules were designed with BTD as the acceptor core, keeping one of the donor moieties of the molecule fixed in position 4, the 9-dimethyl-9H-fluoren-2-yl (FL) unit, a weak electron-donating group, which was introduced owing to the rigidity and planarity of its aromatic component but also to the bulkiness the methyl substituents add, which may lead to twisted conformations that benefit a small ΔE_{ST} , interruption of the conjugation between donors and acceptor components and enhance radiative decays, important characteristics of TADF emitters. Such twisted conformation would diminish π - π stacking interactions in aggregate formation changing the relaxation process to the radiative paths. This fluorenyl group in position 4 of the BTD core was selected considering the reliable performance of the OLED fabricated with a “hot-exciton” symmetric 4,7-difluorenyl-BTD derivative⁶⁶ (Scheme 4).

In addition to the FL group, units that provided either AIEE or TADF properties^{65,82,98,101} were inserted into the structure in position 7 of the BTD core to afford asymmetric fluorenyl-BTD derivatives and study the effects of these substituents in the previously reported symmetric structure showing TADF properties. Therefore, compounds FL-BTD-OAM, FL-BTD-AME, FL-BTD-IDB and FL-BTD-PXZ, displaying 4-methoxy-phenoxy, 4-methoxy-phenyl, iminodibenzyl and phenoxazinyl units were proposed (Scheme 4).

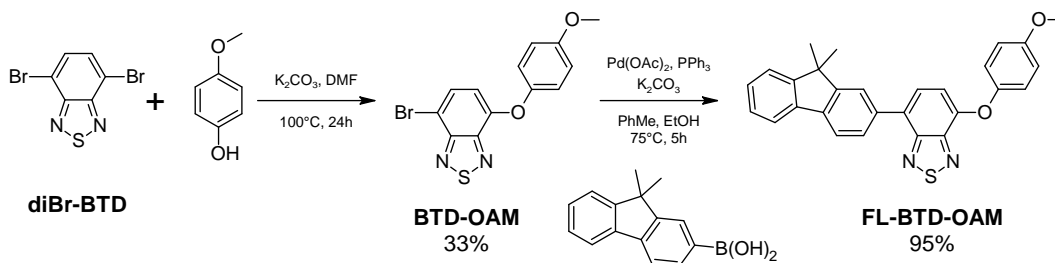
Two different strategies were used for the synthesis of the FL-BTDs. For FL-BTD-OAM and FL-BTD-AM, the insertion of aryl or aryloxy units preceded the fluorenyl group installation. On the other hand, for the synthesis of FL-BTD-IDB and FL-BTD-PXZ, a common mono-brominated

FL-BTD-Br intermediate was first produced and then submitted to amination to install imidodibenzyl and phenoxazinyl units.



Scheme 4. Design of the novel fluorenyl-BTD derivatives.

In the synthesis of FL-BTD-OAM, diBr-BTD was reacted with 4-methoxyphenol in the presence of K_2CO_3 in degassed DMF providing the BTD-OAM intermediate in 33% yield. A second reaction was performed, using Br-BTD-OAM and 9,9-dimethyl-9H-fluoren-2-yl boronic acid under Suzuki cross-coupling optimized conditions⁸² to afford FL-BTD-OAM in 95% yield.



Scheme 5. Synthesis of FL-BTD-OAM.

To illustrate the structural characterization, the ^1H NMR spectrum of FL-BTD-OAM is depicted in Figure 26. The singlet integrating for three hydrogens at 3.86 ppm and the two coupled doublets at 7.35 and 6.98 ppm ($J = 8.9$ Hz), integrating two hydrogens each, are related to the 4-methoxyphenol portion. Coupled doublets ($J=7.8\text{Hz}$) at 7.62 and 6.83 ppm, integrating for one hydrogen, are from the BTD core. Finally, the singlets at 1.56 ppm (6H, methyl groups) and 7.93 ppm (1H), and the other signals are associated with the fluorenyl group.

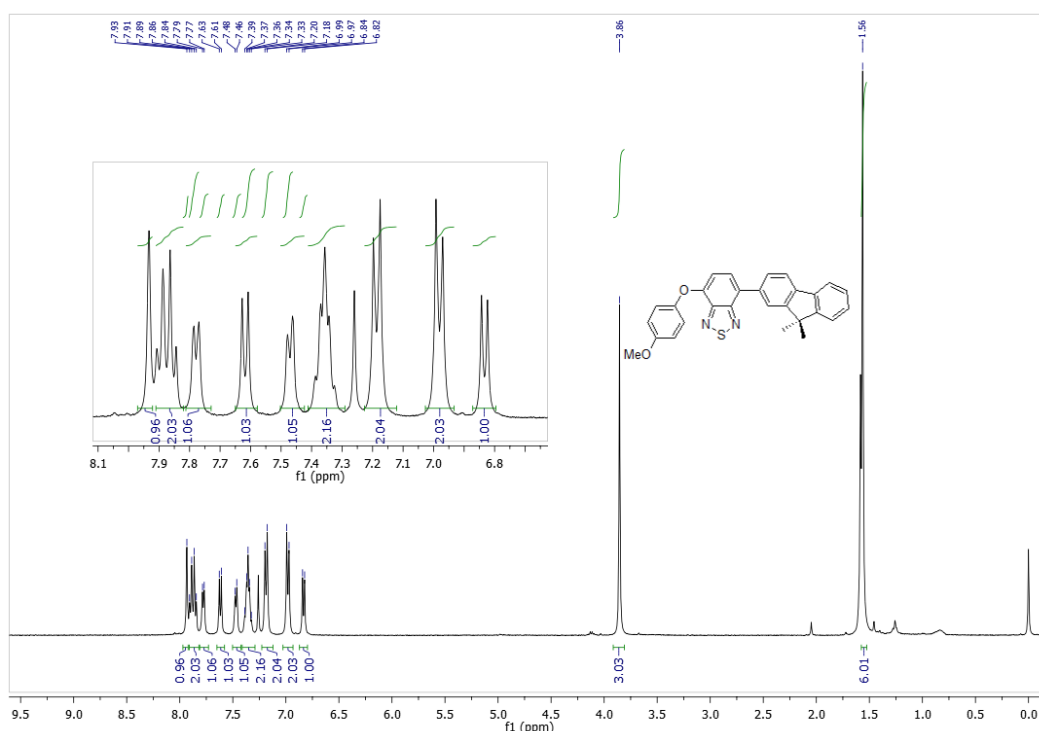
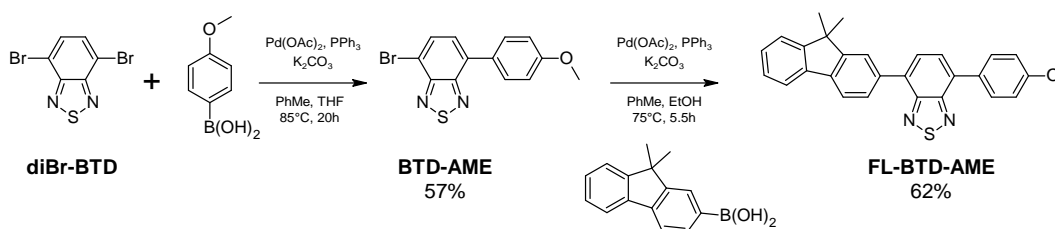


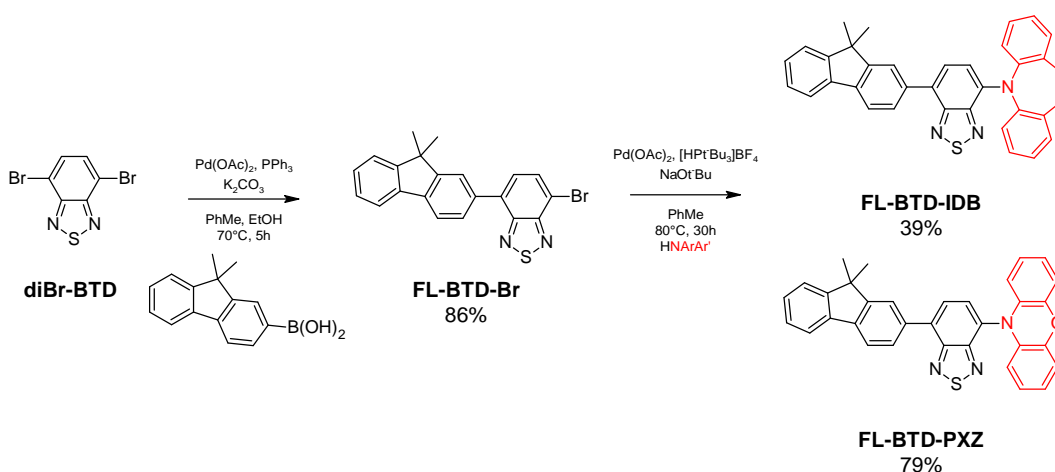
Figure 26. ^1H NMR spectrum of FL-BTD-OAM (400 MHz, CDCl_3).

For the synthesis of FL-BTD-AME, initially, diBr-BTD was submitted to Suzuki conditions, providing the mono-brominated intermediated Br-BTD-AME in 57% yield. This compound was then submitted to a second Suzuki reaction which afforded the final compound in 62% yield.



Scheme 6. Synthesis of FL-BTD-AME.

FL-BTD-IDB and FL-BTD-PXZ were synthesised using a different approach. First, the intermediate FL-BTD-Br (86% yield) was obtained *via* Suzuki cross-coupling. It is important to highlight that the synthesis of this intermediate was challenging, mainly because of the laborious isolation of FL-BTD-Br from the symmetric diarylated by-product. For the obtention of the target molecules, FL-BTD-Br was then submitted to Buchwald-Hartwig amination with iminodibezyl or phenoxazine in a system composed by PdOAc, [HP(*t*-Bu)₃]BF₄ which afforded FL-BTD-IDB and FL-BTD-PXZ In 39% and 79% yield, respectively.



Scheme 7. Synthesis of FL-BTD-IDB and FL-BTD-PXZ.

The obtained FL-BTD-IDB and FL-BTD-PXZ were characterized using NMR and HRMS ¹H NMR spectrum of FL-BTD-PXZ is displayed in Figure 27. Double doublets at 6.80 (2H) and 5.92 ppm (2H) and triple doublets at 6.71 (2H) and 6.58 (2H) ppm correspond to the 8 hydrogens of the PXZ group. One of the hydrogens related to the BTD core is found at 8.08 ppm (1H) as a doublet, which is shifted downfield due to the insertion of the PXZ group. Lastly, hydrogens for fluorenyl moiety are present as a singlet at 1.62 ppm, for 6 hydrogens, related to methyl groups, two double doublets at 8.04 (1H), 7.94 (2H) ppm, and two multiplets at 7.87 (2H) and 7.44 (2H), related aromatic CHs.

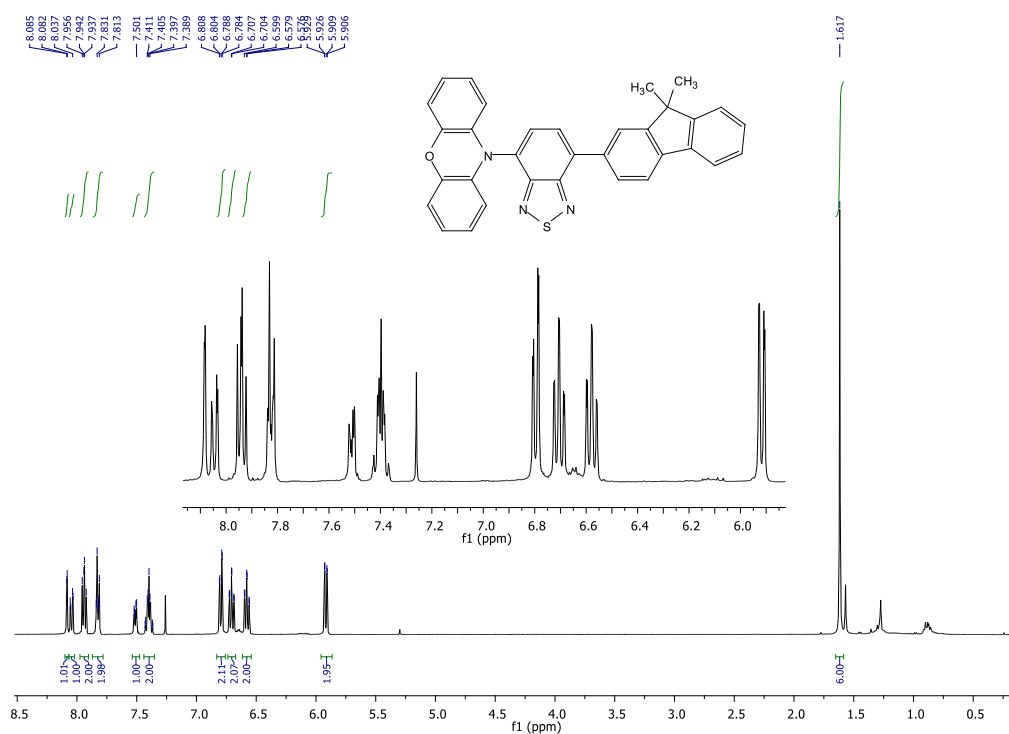


Figure 27. ^1H NMR spectrum of FL-BTD-PZX (400 MHz, CDCl_3).

6.2. Theoretical simulations

DFT was used to estimate HOMO and LUMO energy levels, as well as, to evaluate their distributions over the molecules (Figure 28 and Table 8). In addition, TD-DFT was used to determine S_1 and T_1 and, ΔE_{ST} , which can indicate the potential of the compounds to present RISC, and consequently display delayed fluorescence. HOMO values between -4.49 and -5.23 eV, along with LUMO energy values from -2.07 to -2.51 eV were estimated. These values indicated an E_{gap} from 2.08 to 3.16 eV, which are within the appropriate range for application as emissive layers in OLEDs. It is important to highlight that the insertion of phenoxazine and iminodibenzyl groups led to enhance in HOMO energy and consequently, a decrease in the bandgaps. This is expected since these nitrogenated heterocycles are better electron donors than the methoxyphenyl and methoxyphenoxy groups. In terms of orbital distribution, for all fluorophores, LUMO is highly concentrated over the acceptor BTD. Regarding the HOMO, for FL-BTD-AME the orbital coefficient over the whole structure is observed. The presence of additional oxygen in FL-BTD-AME is reflected as a confinement

of the orbital over the Ar-BTD fragment since no orbital coefficient was detected over the aryloxy unit. The significant HOMO distribution over the BTD core for these two compounds indicates that they are not prone to TADF. An opposite result was observed for compounds FL-BTD-IDB and FL-BTD-PXZ, in which the HOMO orbitals are highly concentrated over the donor IDB and PXZ groups. As for these compounds, LUMO is restricted to the acceptor units IDB and PXZ, and HOMO is distributed on donor groups, DFT indicates these compounds present a potential to display TADF properties. TD-DFT also shows the potential of FL-BTD-IDB and FL-BTD-PXZ to present delayed fluorescence. The exceedingly small ΔE_{ST} suggest a facilitated RISC, which can lead to luminescence with both T_1 and S_1 being populated.

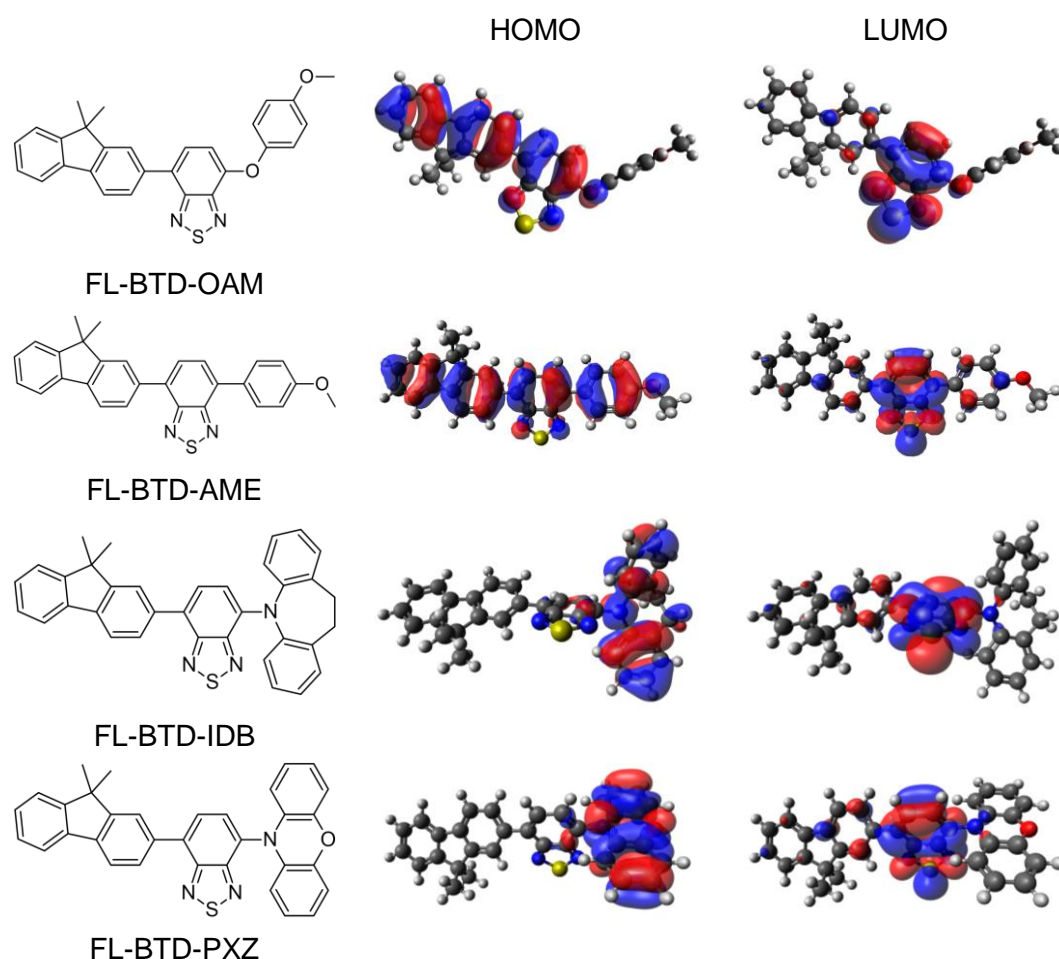


Figure 28. The HOMO and LUMO distribution from DFT calculations of FL-BTD derivatives.

Table 8. Theoretical simulation data in eV for FL-BTD derivatives.

	HOMO	LUMO	E _{gap}	E _S	E _T	ΔE _{ST}
FL-BTD-OAM	-5.23	-2.07	3.16	2.77	2.02	0.75
FL-BTD-AME	-5.20	-2.20	3.00	2.65	1.92	0.73
FL-BTD-IDB	-5.01	-2.41	2.60	1.94	1.89	0.05
FL-BTD-PXZ	-4.59	-2.51	2.08	1.45	1.44	0.01

6.3. Photophysical properties

The photophysical characterization of the FL-BTD derivatives was carried out in different solvents (toluene, THF, Chloroform, acetonitrile, and ethanol). Absorption and fluorescence spectra are presented in Figures 29 and 30, and relevant data are summarized in Table 9. Along with these data, for sake of comparison, the photophysical data of the previously reported FL-BTD-FL “hot exciton” TADF⁶⁶ is also reported. Absorption maxima between 397 and 505 nm were observed. The PXZ- and the IDB-substituted compounds presented redshifted absorption compared to the aryl/aryloxy-substituted compounds, which is in agreement with the smaller band gap calculated via DFT. FL-BTD-OAM, FL-BTD-AME and FL-BTD-IDB presented relatively high molar extinction coefficient values ($10^4 \text{ L mol}^{-1} \text{ cm}^{-1}$), whereas FL-BTD-PXZ presented a less intense band ($10^4 \text{ L mol}^{-1} \text{ cm}^{-1}$). This result indicates that the PXZ group play a significant role in the photophysics of this compound. FL-BTD-PXZ also present a distinct behaviour in terms of solvatochromism. While FL-BTD-OAM, FL-BTD-AME and FL-BTD-IDB presented a small $\Delta\lambda_{\text{abs}}$ (3-9 nm), the absorption maximum of FL-BTD-PXZ varied 33 nm. This result suggests a higher degree of charge separation for this derivative in the ground state. Optical bandgaps from 2.06 to 2.68 eV were estimated from the onset of the absorption curves, which are in reasonable agreement with the values obtained from DFT.

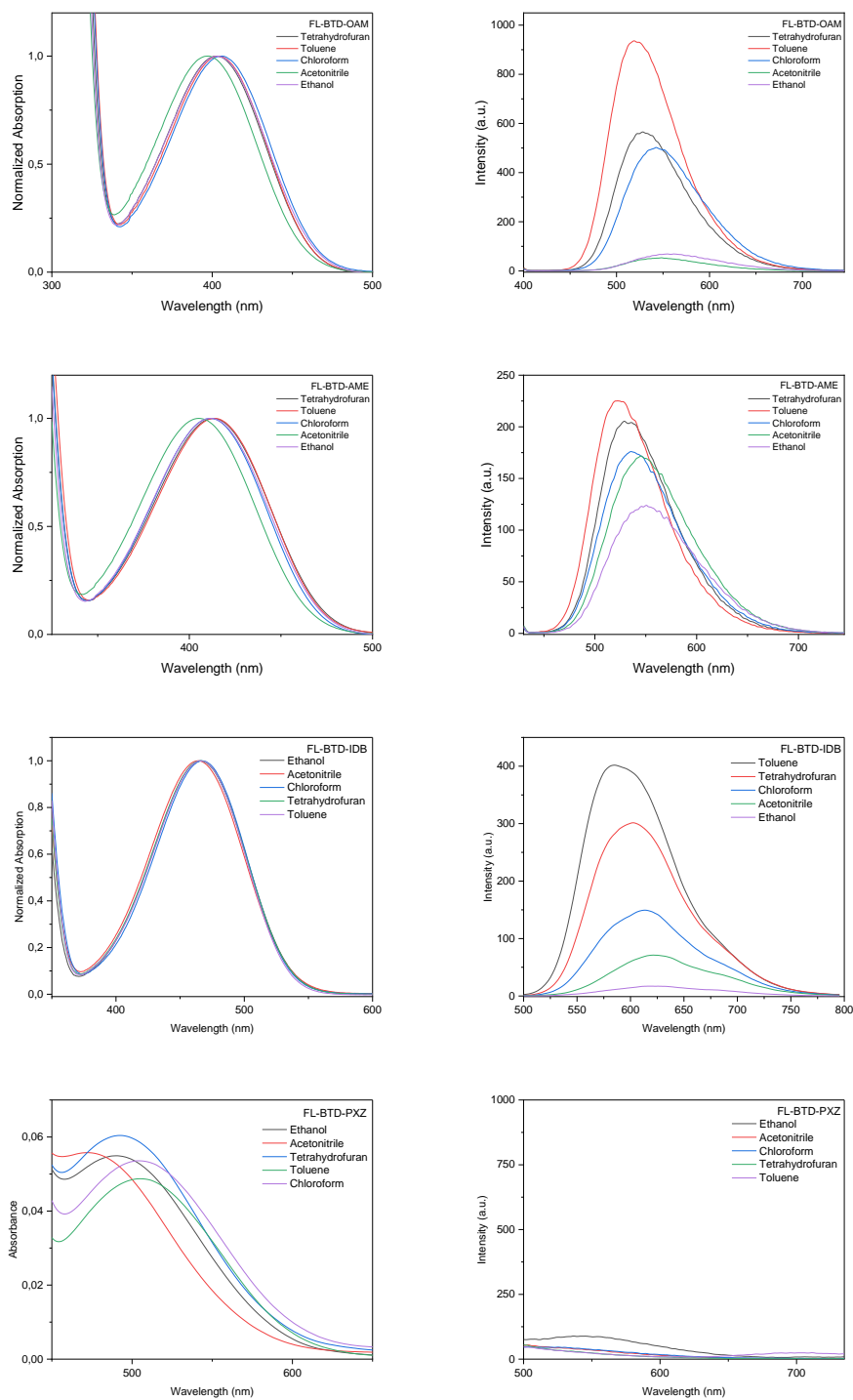


Figure 29. UV-vis absorption and fluorescence spectra in solution using different organic solvents of the FL-BTD derivatives.

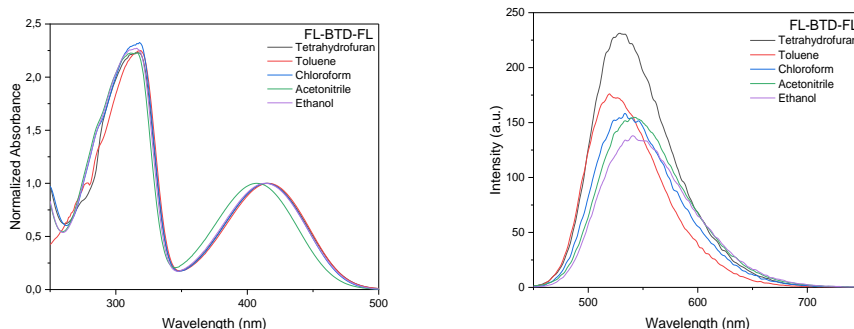


Figure 29–vis absorption and fluorescence spectra in solution using different organic solvents of FL-BTD-FL

Table 9. Photophysical data for FL-BTD derivatives in solution.

FL-BTD	OAM	AME	IDB	PXZ	2FL ⁶⁶	
λ_{abs} (nm)	Toluene	404	414	465	505	416
	THF	402	413	465	490	415
	Chloroform	405	411	467	505	415
	Acetonitrile	397	405	464	472	407
	Ethanol	403	411	466	490	414
$\Delta\lambda_{\text{abs}}$ (nm)		7	9	3	33	9
ϵ_{THF} (cm ⁻¹ mol ⁻¹ L)		9653	23564	11457	1400	- ^b
Optical band gap (eV) THF		2.68	2.63	2.32	2.06	2.55
λ_{em} (nm)	Toluene	519	522	585	-	519
	THF	528	529	603	-	529
	Chloroform	543	535	614	-	533
	Acetonitrile	548	545	621	-	541
	Ethanol	555	550	620	-	540
$\Delta\lambda_{\text{em}}$ (nm)		36	28	36	-	22
$\Delta\lambda_{\text{st}}$ (nm)	Toluene	115	108	120	-	103
	THF	126	116	138	-	114
	Chloroform	138	124	147	-	118
	Acetonitrile	151	140	157	-	134
	Ethanol	152	139	154	-	126
ϕ_f	Toluene	0.42	0.65	0.10	-	0.73
	THF	0.65	0.67	0.07	-	0.75

Compounds FL-BTD-OAM, FL-BTD-AME and FL-BTD-IDB presented fluorescence in solution. The aryl- and the aryloxy-substituted

compounds presented green to yellow emission (519-555 nm) and the IDB-derivative presented fluorescence in the yellow to orange region (585-620 nm). Contrarily, FL-BTD-PXZ did not display fluorescence emission in any of the tested solvents. Large Stokes shifts along with a positive solvatochromic effect were observed, which indicate a stabilized excited state with an ICT character. Fluorescence quantum yields (ϕ_f) were determined in toluene and THF solutions and values from 0.07 to 0.67 were observed, with the following fluorescence intensity order: FL-BTD-AME > FL-BTD-OAM > FL-BTD-IDB > FL-BTD-PXZ (not fluorescent). It is important to highlight that even the most emissive compound in the solution presented less intense fluorescence emission than the previously reported FL-BTD-FL ($\phi_f = 0.73-0.75$). However, this emission intensity order observed in the solution is not necessarily the same as observed in the solid state, since the aggregation can affect differently the fluorophores.

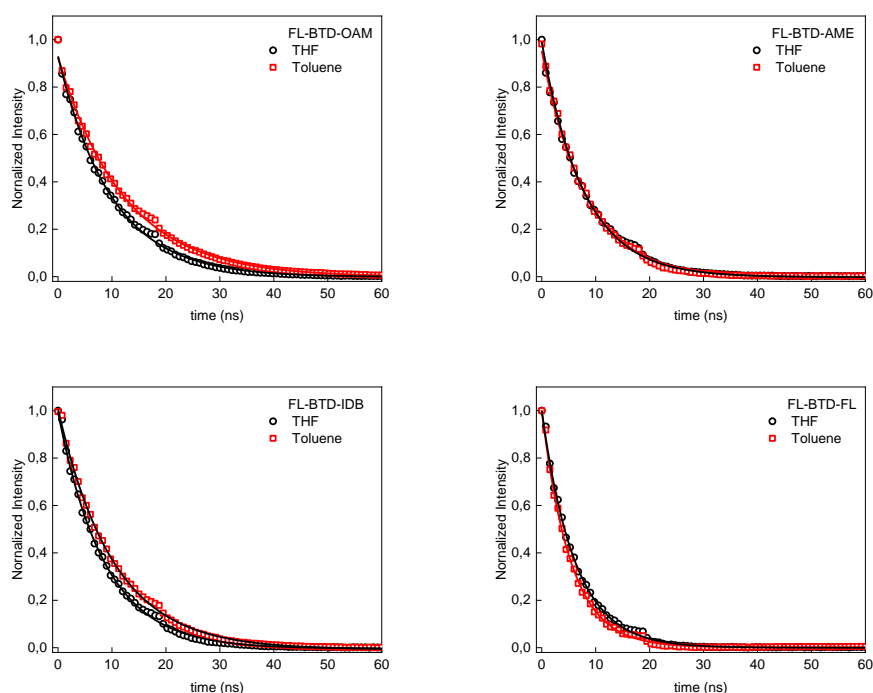


Figure 30. Fluorescence decays of FL-BTD derivatives.

To evaluate the excited state dynamics, and the occurrence of prompt and delayed fluorescence decays, time-resolved fluorescence measurements were performed for the FL-BTD derivatives. Photoluminescence decay curves in THF and Toluene are represented in

Figure 31 and τ values along with, k_r and k_{nr} are displayed in Table 10. For all compounds just the prompted fluorescence decay is observed, including FL-BTD-FL, previously reported by Liu et al. to present prompted and delayed fluorescence decays of 48.96 ns and 0.37 μ s, respectively,⁶⁶ for this compound measurements were made in two different equipment obtaining equivalent results, a monoexponential decay of 5.2 ns in toluene and 6 ns in THF.

For the designed compounds in this work, just τ_{prompt} values were obtained, 8.4 to 12.4 ns in toluene and 8 to 10 ns in THF, indicating the absence of delayed fluorescence. Radiative and non-radiative constants were determined as well, with k_r doubling the values of k_{nr} for FL-BTD-OAM and FL-BTD-AME, indicating the preference for emission in these compounds as a deactivation channel from the excited state. In contrast, FL-BTD-IDB, presented higher values of k_{nr} , indicating the tendency of this compound to relax from its excited state *via* non-radiative channels.

Table 10. Time-resolved fluorescence data of the FL-BTD derivatives.

Toluene	τ_{prompt} (ns)	ϕ_f	k_r ($\times 10^8 \text{s}^{-1}$)	k_{nr} ($\times 10^8 \text{s}^{-1}$)
FL-BTD-AOM	12,4	0,65	0,525	0,281
FL-BTD-AME	7,6	0,67	0,882	0,434
FL-BTD-FL	5,2	0,75	1,438	0,485
FL-BTD-IDB	8,4	0,10	0,123	1,068
THF				
FL-BTD-AOM	9,8	0,43	0,434	0,587
FL-BTD-AME	8	0,65	0,818	0,433
FL-BTD-FL	6	0,73	1,217	0,450
FL-BTD-IDB	10	0,08	0,077	0,923

6.4. Aggregation-induced enhanced emission (AIEE) properties.

Fluorescence measurements of FL-BTD-OAM, FL-BTD-AM and FL-BTD-IDB were performed in THF/H₂O mixtures with increasing water

fraction, to evaluate the AIEEgenic properties of these compounds (Figure 32a-f). For sake of comparison, the previously reported FL-BTD-FL derivative was also evaluated (Figure 32g-h). For FL-BTD-OAM, initially, the increment of water led to a significant decrease in the fluorescence intensity, which can be attributed to the improvement in the solvent polarity and its influence in the charged excited state (Figure 32a). However, around $f_w = 80$, the fluorescence intensity presented a sharp increase, attaining around 80% of the original fluorescence emission (in pure THF). For a better description of the phenomenon, fluorescence quantum yields were determined for selected samples. The ϕ_f value of 0.41 in pure THF decreased to 0.03 at $f_w = 70$ and attained 0.30 in 99% of water, which represents a 10-fold enhancement, with the restoration of nearly 73% of the fluorescence presented by the isolated species. Aggregation-induced enhanced emission was also observed for FL-BTD-IDB (Figures 32e-f). The fluorescence quantum yield of 0.08 observed for the isolated species decreased to 0.01 at $f_w = 70\%$ and was recovered by the aggregation ($\phi_f = 0.08$ in $f_w = 85\%$). Another noteworthy aspect observed for FL-BTD-OAM and FL-BTD-IDB is the emission colour (insets of Figures 32b and 32e). For both compounds, before aggregation, the improvement of solvent polarity caused the bathochromic shift. This is expected since a stronger interaction between a charged molecule (in the excited state) and a polar solvent causes stabilization. However, after aggregation, hypochromic shifts took place. This is due to the formation of solvent-inaccessible regions in the emissive nano-aggregates. The lack of solvent-fluorophore interactions led to both destabilization of the excited state (and consequently a blue shift) and improvement in the fluorescence intensity.

An opposite behaviour was observed for FL-BTD-AME, whose ϕ_f progressively decreased from 0.65 to 0.18 with the increment of water content, which excludes an AIEEgen character for this compound. However, it is important to emphasize that, despite AIEE was not observed, FL-BTD-AME fluorescence was not completely quenched by the aggregation since in higher f_w , fluorescence quantum yields greater than 0.18 were observed. The absence of AIEE was also noted for the previously reported “hot exciton

TADF” FL-BTD-FL, whose fluorescence was interestingly less affected by the augmentation in the water content.

Supplemental data for the AIEE/ACQ mechanisms in FL-BTD derivatives were obtained from crystal structures of compounds FL-BTD-OAM and FL-BTD-AME (Figure 33). It is expected that rigidity and restriction of rotations and vibrations in the aggregated state enhance the emission for good AIEEgens, as well as longer distances between each molecular unit in the crystal structure and large dihedral angles.

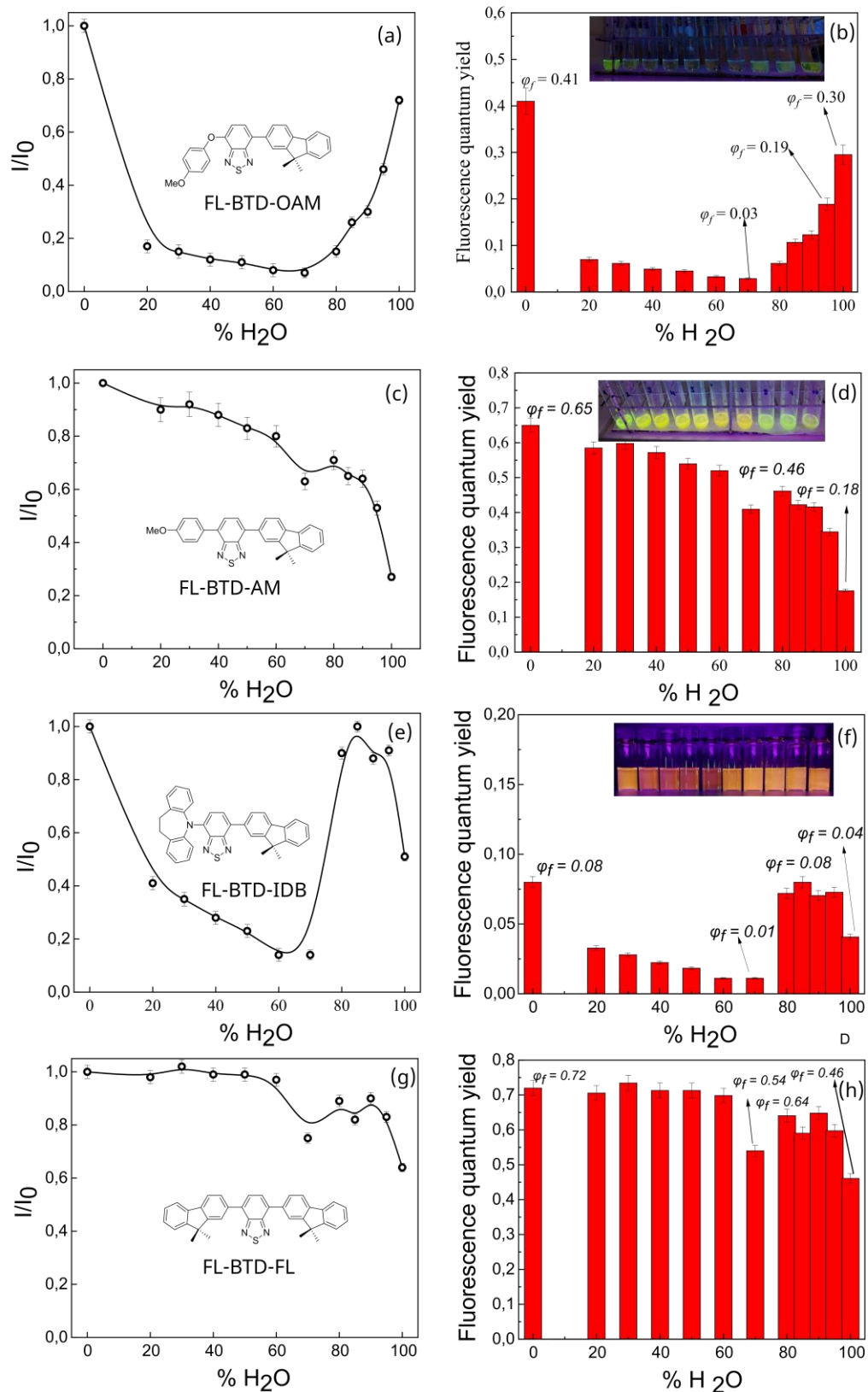


Figure 31. Relative fluorescence intensity (left) and $\phi_{f\zeta}$ (right) for FL-BTD derivatives in THF/water mixtures with different fw. (a, b) FL-BTD-OAM (c, d) FL-BTD-AME (e, f) FL-BTD-IDB (g, h) FL-BTD-FL

FL-BTD-OAM crystallizes with two crystallographic independent molecules in the asymmetric unit almost perpendicularly with respect BTDs planes (86.65°). Dihedral angles between the planes of acceptor and donor moieties are around 16° for FL/BTD and 80° for BTD/OAM in both independent molecules. These twisted conformations, provided mostly by the aryloxy group, generate distances between each molecular unit of 5.3 and 8.6 Å, avoiding π - π stacking interactions, which favours radiative decays.

A minor distortion in the molecular unit of FL-BTD-AME and a more planar conformation can be observed in the crystal structure (Figure 33). Dihedral angles of 41.76° and 49.02° between the planes of each donor with the BTD acceptor unit can be observed. This leads to a better approach between molecules, with the dissipation of the energy through π - π stacking interactions of 3.85 to 5.34 Å in the BTDs units enhanced by the short contacts between N---S of 3.45 Å. Thus, it is expected a decline of the emission intensity in the aggregate state, observed for FL-BTD-AME once the water fraction reaches a critical point.

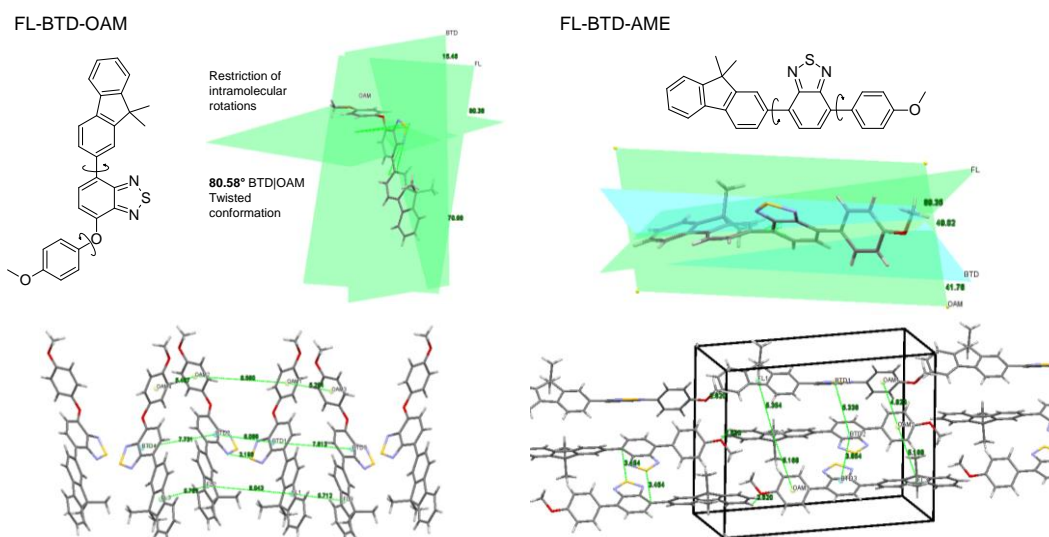


Figure 32. Molecular and single crystal structures (top) and packed crystal structures (bottom) of FL-BTD-OAM and FL-BTD-AME

6.5. Electroluminescence evaluation of FL-BTD-OAM

For the construction of the OLED, it was first necessary to determine the HOMO and LUMO energy levels of the compound to be used as emitting layer. Thus, using cyclic voltammetry, the electrochemical properties of FL-BTD-OAM were determined (Appendix A4). HOMO and LUMO energy levels were calculated from the onset of oxidation and reduction peaks respectively. HOMO was calculated to be -5.845 eV and LUMO -3.376 eV with the corresponding band gap of 2.469 eV.

The performance of compound FL-BTD-OAM as an emissive layer in OLEDs was evaluated with the fluorophore dispersed in a BCPO matrix. It is important to highlight that BCPO was selected considering the match between its emission band and the absorption of the BTD derivative. Another crucial factor is the favourable arrangement of the HOMO/LUMO levels of the matrix and the emitter. The device was fabricated with the following structure: ITO (150 nm) / MoO₃(2 nm) / β -NPB(30 nm) / BCPO(30 nm) / **FL-BTD-OAM** (30 nm) / Bphen (40 nm) / LiF(0.1 nm) / Al(150 nm) (Figure 34).

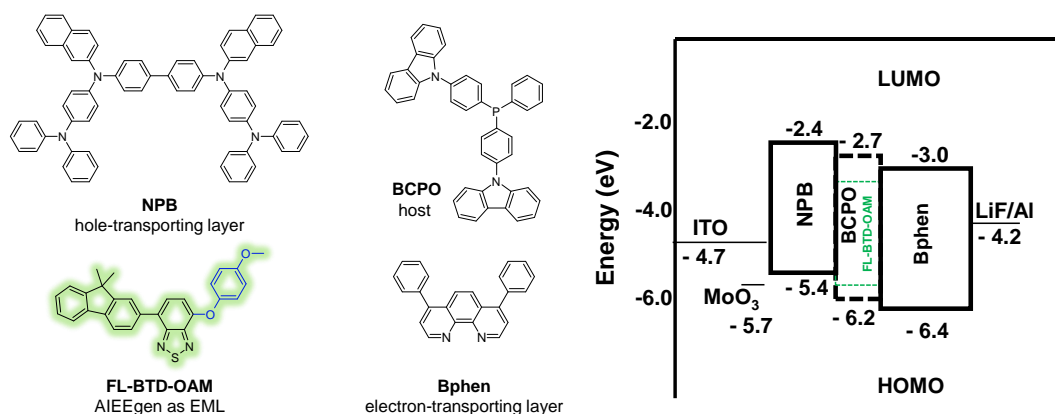


Figure 33. Energy diagram of materials used in the fabricated device.

The device presented low turn voltage ($V_{on} < 3V$) and green electroluminescence centred at 538 nm (Figure 35a) with CIE chromaticity coordinates ($x = 0.27$, $y = 0.72$). Moreover, the emission maximum was not altered by the improvement of the current intensity. A representative image of the device under operation is displayed in Figure 35b. The OLED

performance was then characterized in terms of luminance, irradiance, and current efficiency, with the device presenting excellent results for a metal-free, non-TADF emitter. The maximum luminance of 6450 cd m^{-2} indicates that the device is capable to operate with high brightness. The maximum irradiance of 503 mW cm^{-2} indicates an efficient charge injection and the attained 0.84 cd/A represents a reasonable value of current efficiency. This performance is considerably superior to the observed for our previously reported Ar-BTD-OAr AIEEgen⁸² and comparable to a previously reported thiophenyl- and triphenylamino-substituted BTD derivative.¹⁰⁴ Moreover, the maximum luminance attained with FL-BTD-OAM is more than twice the observed in a previously reported BTD-based TADF (2980 cd m^{-2}).⁶⁵ It is important to highlight that novel devices using FL-BTD-AME and FL-BTD-FL as emitters are under development in our group.

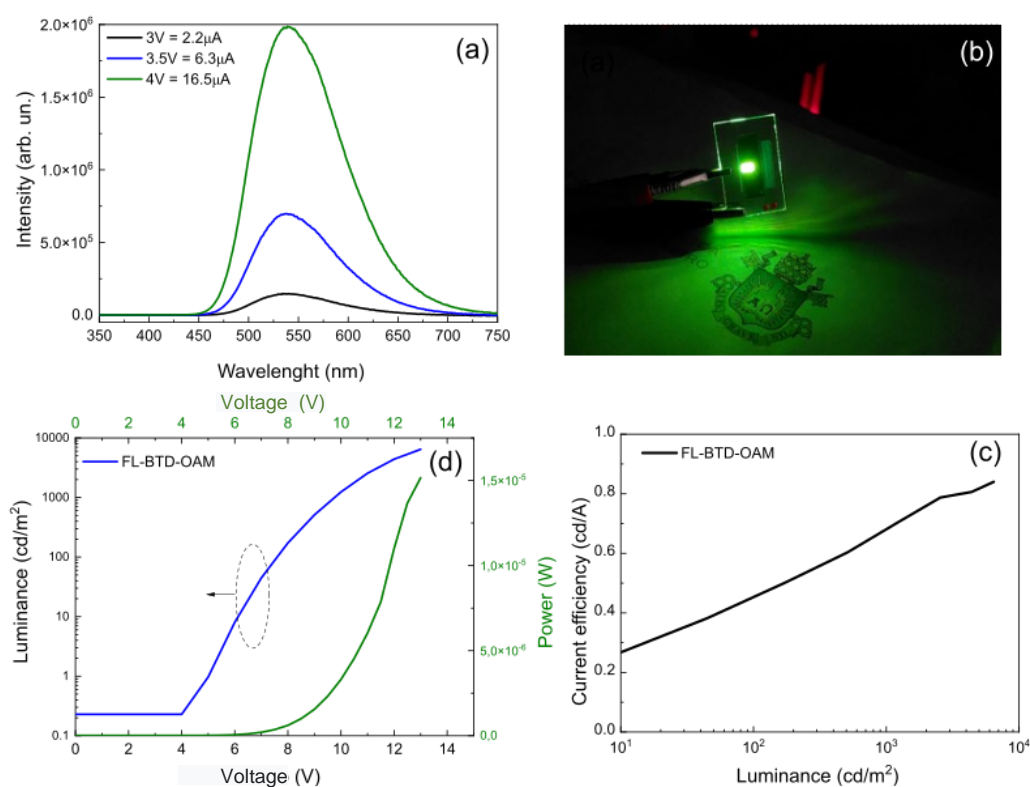


Figure 34. (a) electroluminescence spectrum of the OLED as a function of applied voltage. (b) Representative image of the device under operation. (c) Luminance and Potency in function of applied voltage. (d) Current efficiency as a function of luminance.

6.6. Partial Conclusions

In summary, four novel fluorenyl-BTD derivatives were designed and synthesized aiming TADF and AIEE. The compounds presented absorption in the blue to green regions and three of them presented fluorescence emission in solution. Fluorescence quantum yields between 0.07 and 0.67 were observed. Despite TD-DFT results indicating small DE_{ST} , time-resolved fluorescence refuted the occurrence of TADF in these compounds. The aryloxy-substituted and the iminodibenzyl-substituted fluorenyl-BTD derivatives presented aggregation-induced enhanced emission. The OLED fabricated with the fluorenyl-BTD-aryloxy derivative operated with high brightness, good irradiance and reasonable current efficiency.

Chapter 7. Conclusions and perspectives

In this work, new photoluminescent molecules were synthesised and studied, showing photophysical properties that make them potential candidates for applications in optoelectronic devices. A total of six PPC derivatives and four fluorenyl-BTD derivatives were obtained, which are unpublished and described for the first time.

PPC derivatives presented absorptions in the UV region and cyan to green emissions with fluorescence quantum yields in solution of up to 0.70. Donor groups in the D- π -A type system, had an important influence on the photophysical properties of the compounds, with the fluorenyl group achieving FL-PPC, with the highest emission, whereas 2-toluyyl substitution produced a weak to non-emissive compound, 2M-PPC. An interesting TICT/LE equilibrium for the excited states was observed for MT-PPC.

Measurements of delayed fluorescence showed that none of the designed compounds presented TADF, leading to think biaryl donors are not suitable for the obtention of delayed fluorescence in PPC systems, although additional studies would need to be conducted to affirm that this is the case.

Aggregation-induced enhanced emission was observed in FL-PPC, MT-PPC and ST-PPC, with promising results from MT-PPC to evaluate it as an emissive layer in OLED.

Regarding the second family, derivatives of fluorenyl-BTD with D-A-D type structure, presented absorption from 397 to 505 nm with emission from green to orange for 3 of the novel compounds, with fluorescence quantum yields of up to 0.67. Notwithstanding the results obtained in the computational simulations, the compounds did not show delayed fluorescence, which was refuted by the time-resolved fluorescence experiments. Regardless of the absence of TADF compounds, new luminescent materials with AIEE were obtained, having fabricated an OI FD

device using FL-BTD-OAM as an emissive layer with high brightness, good irradiance and reasonable current efficiency.

As future perspectives, is expected to continue the efforts in the construction of efficient devices, using MT-PPC as an emissive layer, as well as FL-BTD-AME, which, although it does not present AIEE, was not affected to a great extent in the aggregated states and its fluorescent quantum yield makes it attractive to be used as an emitter layer.

Additionally, it is anticipated the optimization of the synthesis of PA-PPC to isolate it, allowing its complete photophysical characterization, as well as the complete characterization of ST-PPC, to have further insights into the influence of this arylated donors on a recognized TADF acceptor as the PPC.

Bibliography

1. Bauri, J., Choudhary, R. B. & Mandal, G. Recent advances in efficient emissive materials-based OLED applications: a review. *Journal of Materials Science 2021* 56:34 **56**, 18837–18866 (2021).
2. Liang, X., Tu, Z. L. & Zheng, Y. X. Thermally Activated Delayed Fluorescence Materials: Towards Realization of High Efficiency through Strategic Small Molecular Design. *Chemistry – A European Journal* **25**, 5623–5642 (2019).
3. Yang, Z. *et al.* Recent advances in organic thermally activated delayed fluorescence materials. *Chemical Society Reviews* vol. 46 915–1016 Preprint at <https://doi.org/10.1039/c6cs00368k> (2017).
4. Xie, F. M., Zhou, J. X., Li, Y. Q. & Tang, J. X. Effects of the relative position and number of donors and acceptors on the properties of TADF materials. *Journal of Materials Chemistry C* vol. 8 9476–9494 Preprint at <https://doi.org/10.1039/d0tc02252g> (2020).
5. Zhang, Z. *et al.* Efficient Sky-Blue Organic Light-Emitting Diodes Using a Highly Horizontally Oriented Thermally Activated Delayed Fluorescence Emitter. *Adv Opt Mater* **8**, 2001354 (2020).
6. Karthik, D. *et al.* Acceptor–Donor–Acceptor-Type Orange–Red Thermally Activated Delayed Fluorescence Materials Realizing External Quantum Efficiency Over 30% with Low Efficiency Roll-Off. *Advanced Materials* **33**, 2007724 (2021).
7. Naqvi, B. A. *et al.* What Controls the Orientation of TADF Emitters? *Front Chem* **8**, 750 (2020).
8. Mei, J. *et al.* Aggregation-Induced Emission: The Whole Is More Brilliant than the Parts. *Advanced Materials* **26**, 5429–5479 (2014).

9. He, Z., Ke, C. & Tang, B. Z. Journey of Aggregation-Induced Emission Research. *ACS Omega* **3**, 3267–3277 (2018).
10. Mei, J., Leung, N. L. C., Kwok, R. T. K., Lam, J. W. Y. & Tang, B. Z. Aggregation-Induced Emission: Together We Shine, United We Soar! *Chem Rev* **115**, 11718–11940 (2015).
11. Chen, Z. *et al.* Emitters with a pyridine-3,5-dicarbonitrile core and short delayed fluorescence lifetimes of about 1.5 μ s: orange-red TADF-based OLEDs with very slow efficiency roll-offs at high luminance. *J Mater Chem C Mater* **6**, 6543–6548 (2018).
12. Chen, Y.-K. *et al.* Triarylamine-Pyridine-Carbonitriles for Organic Light-Emitting Devices with EQE Nearly 40%. *Advanced Materials* **33**, 2008032 (2021).
13. You, J. *et al.* Bipolar cyano-substituted pyridine derivatives for applications in organic light-emitting devices. *J Mater Chem* **22**, 8922–8929 (2012).
14. You, J. *et al.* Synthesis and characterization of cyano-substituted pyridine derivatives for applications as exciton blockers in photovoltaic devices. *J Mater Chem* **22**, 5107–5113 (2012).
15. Liu, W. *et al.* Novel Carbazol-Pyridine-Carbonitrile Derivative as Excellent Blue Thermally Activated Delayed Fluorescence Emitter for Highly Efficient Organic Light-Emitting Devices. *ACS Appl Mater Interfaces* **7**, 18930–18936 (2015).
16. Neto, B. A. D., Carvalho, P. H. P. R. & Correa, J. R. Benzothiadiazole Derivatives as Fluorescence Imaging Probes: Beyond Classical Scaffolds. *Acc Chem Res* **48**, 1560–1569 (2015).
17. Neto, B. A. D. *et al.* Deciphering the dynamics of organic nanoaggregates with AIEE effect and excited states: Lipophilic benzothiadiazole derivatives as selective cell imaging probes. *Journal of Organic Chemistry* **85**, 12614–12634 (2020).

18. Neto, B. A. D., Correa, J. R. & Spencer, J. Fluorescent Benzothiadiazole Derivatives as Fluorescence Imaging Dyes: A Decade of New Generation Probes. *Chemistry – A European Journal* **28**, e202103262 (2022).
19. Pode, R. Organic light emitting diode devices: An energy efficient solid state lighting for applications. *Renewable and Sustainable Energy Reviews* **133**, 110043 (2020).
20. Thejo Kalyani, N. & Dhoble, S. J. Organic light emitting diodes: Energy saving lighting technology - A review. *Renewable and Sustainable Energy Reviews* vol. 16 2696–2723 Preprint at <https://doi.org/10.1016/j.rser.2012.02.021> (2012).
21. Shi, H. *et al.* Key Factors Governing the External Quantum Efficiency of Thermally Activated Delayed Fluorescence Organic Light-Emitting Devices: Evidence from Machine Learning. *ACS Omega* **7**, 7893–7900 (2022).
22. Büнау, G. v. J. B. Birks: Photophysics of Aromatic Molecules. Wiley-Interscience, London 1970. 704 Seiten. Preis: 210s. *Berichte der Bunsengesellschaft für physikalische Chemie* **74**, 1294–1295 (1970).
23. Braslavsky, S. E. Glossary of terms used in photochemistry, 3rd edition (IUPAC Recommendations 2006). *Pure and Applied Chemistry* **79**, 293–465 (2007).
24. Jabłoński, A. Über den Mechanismus der Photolumineszenz von Farbstoffphosphoren. *Zeitschrift für Physik* **94**, 38–46 (1935).
25. Delorme, R. & Perrin, F. Durées de fluorescence des sels d'uranyle solides et de leurs solutions,. *Journal de Physique et le Radium* **10**, 177–186 (1929).
26. Klán, P. & Wirz, J. Photochemistry of Organic Compounds: From Concepts to Practice. *Photochemistry of Organic Compounds: From Concepts to Practice* 1–563 (2009) doi:10.1002/9781444300017.

27. Avouris, P., Gelbart, W. M. & El-Sayed, M. A. Nonradiative Electronic Relaxation under Collision-Free Conditions. *Chem Rev* **77**, 793–833 (1977).
28. *Principles of Fluorescence Spectroscopy*. (Springer US, 2006). doi:10.1007/978-0-387-46312-4.
29. Valeur, B. & Berberan-Santos, M. N. A brief history of fluorescence and phosphorescence before the emergence of quantum theory. *J Chem Educ* **88**, 731–738 (2011).
30. Taniguchi, M. & Lindsey, J. S. Database of Absorption and Fluorescence Spectra of >300 Common Compounds for use in PhotochemCAD. *Photochem Photobiol* **94**, 290–327 (2018).
31. Bruton, D. Spectra Code. <http://www.physics.sfasu.edu/astro/color/spectra.html>.
32. Wavelength to Colour Relationship | Academo.org - Free, interactive, education. <https://academo.org/demos/wavelength-to-colour-relationship/>.
33. Rurack, K. & Spieles, M. Fluorescence quantum yields of a series of red and near-infrared dyes emitting at 600-1000 nm. *Anal Chem* **83**, 1232–1242 (2011).
34. Uoyama, H., Goushi, K., Shizu, K., Nomura, H. & Adachi, C. Highly efficient organic light-emitting diodes from delayed fluorescence. *Nature* **492**:7428 **492**, 234–238 (2012).
35. Sun, W., Guo, S., Hu, C., Fan, J. & Peng, X. Recent Development of Chemosensors Based on Cyanine Platforms. *Chem Rev* **116**, 7768–7817 (2016).
36. Neto, B. A. D., Correa, J. R. & Spencer, J. Fluorescent Benzothiadiazole Derivatives as Fluorescence Imaging Dyes: A Decade of New Generation Probes. *Chemistry – A European Journal* **28**, e202103262 (2022).

37. Xiong, X. *et al.* Thermally activated delayed fluorescence of fluorescein derivative for time-resolved and confocal fluorescence imaging. *J Am Chem Soc* **136**, 9590–9597 (2014).
38. Wang, Y., Wang, J., Ma, Q., Li, Z. & Yuan, Q. Recent progress in background-free latent fingerprint imaging. *Nano Research* **2018** *11:10* **11**, 5499–5518 (2018).
39. Parker, C. A. & Hatchard, C. G. Triplet-singlet emission in fluid solutions. Phosphorescence of eosin. *Transactions of the Faraday Society* **57**, 1894–1904 (1961).
40. Tao, Y. *et al.* Thermally Activated Delayed Fluorescence Materials Towards the Breakthrough of Organoelectronics. *Advanced Materials* **26**, 7931–7958 (2014).
41. Méhes, G., Nomura, H., Zhang, Q., Nakagawa, T. & Adachi, C. Enhanced Electroluminescence Efficiency in a Spiro-Acridine Derivative through Thermally Activated Delayed Fluorescence. *Angewandte Chemie International Edition* **51**, 11311–11315 (2012).
42. Wex, B. & Kaafarani, B. R. Perspective on carbazole-based organic compounds as emitters and hosts in TADF applications. *J Mater Chem C Mater* **5**, 8622–8653 (2017).
43. Goushi, K., Yoshida, K., Sato, K. & Adachi, C. Organic light-emitting diodes employing efficient reverse intersystem crossing for triplet-to-singlet state conversion. *Nature Photonics* **2012** *6:4* **6**, 253–258 (2012).
44. Kishore Kesavan, K. *et al.* Achieving a 32% EQE solution-processed simple structure OLED via exciplex system. *Chemical Engineering Journal* **435**, 134879 (2022).
45. Zhang, Y. *et al.* Towards highly efficient red thermally activated delayed fluorescence materials by the control of intra-molecular π - π stacking interactions. *Nanotechnology* **27**, 094001 (2016).

46. Cao, X., Zhang, D., Zhang, S., Tao, Y. & Huang, W. CN-Containing donor–acceptor-type small-molecule materials for thermally activated delayed fluorescence OLEDs. *J Mater Chem C Mater* **5**, 7699–7714 (2017).
47. Zhang, D., Duan, L., Li, Y., Zhang, D. & Qiu, Y. Highly efficient and color-stable hybrid warm white organic light-emitting diodes using a blue material with thermally activated delayed fluorescence. *J Mater Chem C Mater* **2**, 8191–8197 (2014).
48. Yanai, N. *et al.* Increased vis-to-UV upconversion performance by energy level matching between a TADF donor and high triplet energy acceptors. *J Mater Chem C Mater* **4**, 6447–6451 (2016).
49. Chen, D. *et al.* Bipyridine-Containing Host Materials for High Performance Yellow Thermally Activated Delayed Fluorescence-Based Organic Light Emitting Diodes with Very Low Efficiency Roll-Off. *Adv Opt Mater* **8**, 1901283 (2020).
50. Zhang, L., Zhaoyue, L. & Wang, J. The Effect of Carrier Transport Layer on the Electroluminescent Properties of Solution-Processed Thermally Activated Delayed Fluorescent Device based on 4CzPN. *physica status solidi (b)* **259**, 2200072 (2022).
51. Skála, V., Böhm, S., Paleček, J. & Kuthan, J. Electronic and mass spectra of 2,6-disubstituted phenyl and 2-styryl derivatives of 3,5-dicyanopyridines and their 1,4-dihydroanalogues. *Collect Czechoslov Chem Commun* **43**, 434–446 (1978).
52. Duan, L. *et al.* Strategies to Design Bipolar Small Molecules for OLEDs: Donor-Acceptor Structure and Non-Donor-Acceptor Structure. *Advanced Materials* **23**, 1137–1144 (2011).
53. Mahmoud, N. F. H. & El-Sewedy, A. Multicomponent Reactions, Solvent-Free Synthesis of 2-Amino-4-aryl-6-substituted Pyridine-3,5-dicarbonitrile Derivatives, and Corrosion Inhibitors Evaluation. *J Chem* **2018**, (2018).

54. Jayakumar, J. *et al.* Pyridine-Carbonitrile-Carbazole-Based Delayed Fluorescence Materials with Highly Congested Structures and Excellent OLED Performance. *ACS Appl Mater Interfaces* **11**, 21042–21048 (2019).
55. Vigante, B. *et al.* Synthesis of Linear and V-Shaped Carbazolyl-Substituted Pyridine-3,5-dicarbonitriles Exhibiting Efficient Bipolar Charge Transport and E-Type Fluorescence. *Chemistry – A European Journal* **25**, 3325–3336 (2019).
56. Liu, H. *et al.* Modulating the acceptor structure of dicyanopyridine based TADF emitters: Nearly 30% external quantum efficiency and suppression on efficiency roll-off in OLED. *Chemical Engineering Journal* **401**, 126107 (2020).
57. Liu, H. *et al.* Efficient Yellow Thermally Activated Delayed Fluorescent Emitters Based on 3,5-Dicyanopyridine Acceptors. *Journal of Physical Chemistry C* **124**, 25489–25498 (2020).
58. Neto, B. A. D. *et al.* Deciphering the dynamics of organic nanoaggregates with AIEE effect and excited states: Lipophilic benzothiadiazole derivatives as selective cell imaging probes. *Journal of Organic Chemistry* **85**, 12614–12634 (2020).
59. Neto, B. A. D., Lapis, A. A. M., da Silva Júnior, E. N. & Dupont, J. 2,1,3-Benzothiadiazole and Derivatives: Synthesis, Properties, Reactions, and Applications in Light Technology of Small Molecules. *European J Org Chem* **2013**, 228–255 (2013).
60. Neto, B. A. D., Carvalho, P. H. P. R. & Correa, J. R. Benzothiadiazole Derivatives as Fluorescence Imaging Probes: Beyond Classical Scaffolds. *Acc Chem Res* **48**, 1560–1569 (2015).
61. Wang, C. *et al.* Benzothiadiazole-based Conjugated Polymers for Organic Solar Cells. *Chinese Journal of Polymer Science* **2021** 39:5 **39**, 525–536 (2021).

62. He, P., Li, Z., Hou, Q. & Wang, Y. Application of Benzothiadiazole in Organic Solar Cells. *Chinese Journal of Organic Chemistry* **33**, 288 (2013).
63. Du, J., Biewer, M. C. & Stefan, M. C. Benzothiadiazole building units in solution-processable small molecules for organic photovoltaics. *J Mater Chem A Mater* **4**, 15771–15787 (2016).
64. Han Kim, J. *et al.* Recent Progress of Highly Efficient Red and Near-Infrared Thermally Activated Delayed Fluorescent Emitters. *Adv Opt Mater* **6**, 1800255 (2018).
65. Ni, F. *et al.* Teaching an old acceptor new tricks: rationally employing 2,1,3-benzothiadiazole as input to design a highly efficient red thermally activated delayed fluorescence emitter. *J Mater Chem C Mater* **5**, 1363–1368 (2017).
66. Liu, J. *et al.* Experimental Evidence for “Hot Exciton” Thermally Activated Delayed Fluorescence Emitters. *Adv Opt Mater* **7**, 1801190 (2019).
67. Kumsampao, J. *et al.* A Simple and Strong Electron-Deficient 5,6-Dicyano[2,1,3]benzothiadiazole-Cored Donor-Acceptor-Donor Compound for Efficient Near Infrared Thermally Activated Delayed Fluorescence. *Chem Asian J* **15**, 3029–3036 (2020).
68. Huo, J. *et al.* A rational design strategy for red thermally activated delay fluorescence emitter employing 2,1,3-benzothiadiazole skeleton with asymmetric structure. *Dyes and Pigments* **196**, 109781 (2021).
69. Luo, J. *et al.* Aggregation-induced emission of 1-methyl-1,2,3,4,5-pentaphenylsilole. *Chemical Communications* **18**, 1740–1741 (2001).
70. An, B.-K., Kwon, S.-K., Jung, S.-D. & Park, S. Y. Enhanced Emission and Its Switching in Fluorescent Organic Nanoparticles. *J Am Chem Soc* **124**, 14410–14415 (2002).

71. He, Z., Ke, C. & Tang, B. Z. Journey of Aggregation-Induced Emission Research. *ACS Omega* vol. 3 3267–3277 Preprint at <https://doi.org/10.1021/acsomega.8b00062> (2018).
72. Tang, C. W. & Vanslyke, S. A. Organic electroluminescent diodes. *Appl Phys Lett* **51**, 913 (1998).
73. Thejo Kalyani, N. & Dhoble, S. J. Organic light emitting diodes: Energy saving lighting technology—A review. *Renewable and Sustainable Energy Reviews* **16**, 2696–2723 (2012).
74. C Leung, N. L. *et al.* Restriction of Intramolecular Motions: The General Mechanism behind Aggregation-Induced Emission. *Chemistry – A European Journal* **20**, 15349–15353 (2014).
75. Xu, S., Duan, Y. & Liu, B. Precise Molecular Design for High-Performance Luminogens with Aggregation-Induced Emission. *Advanced Materials* **32**, 1903530 (2020).
76. Tang, C. W., Vanslyke, S. A. & Chen, C. H. Electroluminescence of doped organic thin films. *J Appl Phys* **65**, 3610 (1998).
77. Gaylord, B. S., Wang, S., Heeger, A. J. & Bazan, G. C. Water-soluble conjugated oligomers: Effect of chain length and aggregation on photoluminescence-quenching efficiencies. *J Am Chem Soc* **123**, 6417–6418 (2001).
78. Zheng, K. *et al.* Polymorph-Dependent Thermally Activated Delayed Fluorescence Emitters: Understanding TADF from a Perspective of Aggregation State. *Angewandte Chemie International Edition* **59**, 9972–9976 (2020).
79. Xu, S. *et al.* An Organic Molecule with Asymmetric Structure Exhibiting Aggregation-Induced Emission, Delayed Fluorescence, and Mechanoluminescence. *Angewandte Chemie International Edition* **54**, 874–878 (2015).

80. Yang, J., Fang, M. & Li, Z. Organic luminescent materials: The concentration on aggregates from aggregation-induced emission. *Aggregate* **1**, 6–18 (2020).
81. Neto, B. A. D., Lapis, A. A. M., da Silva Júnior, E. N. & Dupont, J. 2,1,3-Benzothiadiazole and Derivatives: Synthesis, Properties, Reactions, and Applications in Light Technology of Small Molecules. *European J Org Chem* **2013**, 228–255 (2013).
82. Pazini, A. *et al.* Designing highly luminescent aryloxy-benzothiadiazole derivatives with aggregation-induced enhanced emission. *Dyes and Pigments* **178**, (2020).
83. Fiuza, R. M. *et al.* A styryl-benzothiadiazole derivative with aggregation-induced enhanced emission for latent fingerprint recognition. *J Lumin* **248**, 118920 (2022).
84. da Costa, R. G. M. *et al.* Synthesis, photophysical properties and aggregation-induced enhanced emission of bischalcone-benzothiadiazole and chalcone-benzothiadiazole hybrids. *J Lumin* **239**, 118367 (2021).
85. Volz, D. *et al.* From iridium and platinum to copper and carbon: new avenues for more sustainability in organic light-emitting diodes. *Green Chemistry* **17**, 1988–2011 (2015).
86. Hong, G. *et al.* A Brief History of OLEDs—Emitter Development and Industry Milestones. *Advanced Materials* **33**, 2005630 (2021).
87. Yang, J.-H. *et al.* 33-1: *Invited Paper*: TADF based OLED Devices. *SID Symposium Digest of Technical Papers* **50**, 458–461 (2019).
88. Wang, S., Zhang, H., Zhang, B., Xie, Z. & Wong, W. Y. Towards high-power-efficiency solution-processed OLEDs: Material and device perspectives. *Materials Science and Engineering: R: Reports* **140**, 100547 (2020).

89. Yadav, R. A. K., Dubey, D. K., Chen, S. Z., Liang, T. W. & Jou, J. H. Role of Molecular Orbital Energy Levels in OLED Performance. *Scientific Reports* 2020 10:1 **10**, 1–15 (2020).
90. Chen, H. W., Lee, J. H., Lin, B. Y., Chen, S. & Wu, S. T. Liquid crystal display and organic light-emitting diode display: present status and future perspectives. *Light: Science & Applications* 2018 7:37, 17168–17168 (2017).
91. Misra, R. & Gautam, P. Tuning of the HOMO–LUMO gap of donor-substituted symmetrical and unsymmetrical benzothiadiazoles. *Org Biomol Chem* **12**, 5448–5457 (2014).
92. Neese, F. Software update: the ORCA program system, version 4.0. *Wiley Interdiscip Rev Comput Mol Sci* **8**, e1327 (2018).
93. Becke, A. D. Density-functional thermochemistry. III. The role of exact exchange. *J Chem Phys* **98**, 5648–5652 (1993).
94. Tirado-Rives, J. & Jorgensen, W. L. Performance of B3LYP density functional methods for a large set of organic molecules. *J Chem Theory Comput* **4**, 297–306 (2008).
95. Hanwell, M. D. *et al.* Avogadro: An advanced semantic chemical editor, visualization, and analysis platform. *J Cheminform* **4**, 1–17 (2012).
96. Sheldrick, G. M. A short history of SHELX. *Acta Crystallogr A* **64**, 112–122 (2008).
97. MacRae, C. F. *et al.* Mercury 4.0: from visualization to analysis, design and prediction. *urn:issn:1600-5767* **53**, 226–235 (2020).
98. Pazini, A. *et al.* Phenoxy-benzothiadiazole dyes: Synthesis, photophysical properties and preliminary application in OLEDs. *Tetrahedron Lett* **59**, (2018).

99. Sjöback, R., Nygren, J. & Kubista, M. Absorption and fluorescence properties of fluorescein. *Spectrochim Acta A Mol Biomol Spectrosc* **51**, L7–L21 (1995).
100. Fiuza, R. M. *et al.* A styryl-benzothiadiazole derivative with aggregation-induced enhanced emission for latent fingerprint recognition. *J Lumin* **248**, (2022).
101. Pazini, A., Maqueira, L., Stieler, R., Aucélio, R. Q. & Limberger, J. Synthesis, characterization and photophysical properties of luminescent non-symmetric 4-pyridyl benzothiadiazole derivatives. *J Mol Struct* **1131**, (2017).
102. da Costa, R. G. M., Farias, F. R. L., Back, D. & Limberger, J. Synthesis of arylated chalcone derivatives via palladium cross-coupling reactions. *Tetrahedron Lett* **59**, (2018).
103. da Costa, R. G. M. *et al.* Synthesis, photophysical and electrochemical properties of novel D- π -D and D- π -a triphenylamino-chalcones and β -arylchalcones. *J Braz Chem Soc* **30**, (2019).
104. Zhang, J., Yang, Y., He, C. & Li, Y. Red-emission organic light-emitting diodes based on solution-processable molecules with triphenylamine core and benzothiadiazole-thiophene arms. *Sci China Chem* **54**, 695–698 (2011).
105. Murawski, C. *et al.* Efficiency Roll-Off in Organic Light-Emitting Diodes. *Advanced Materials* **25**, 6801–6827 (2013).

Appendix

A1. ^1H and ^{13}C NMR spectra

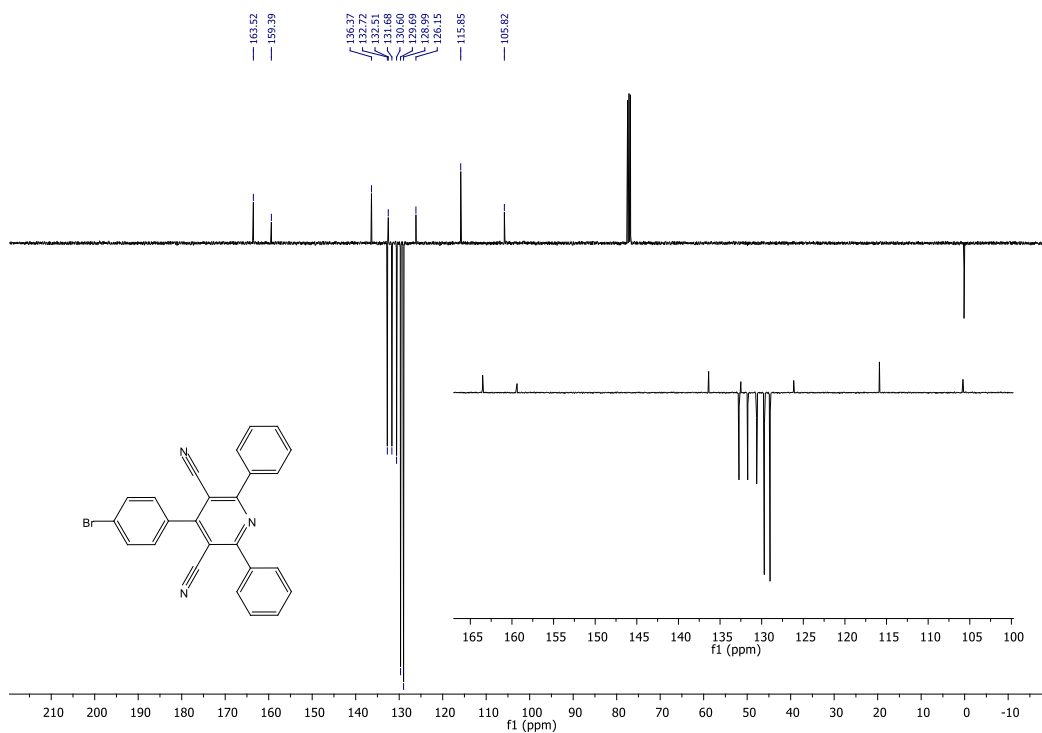


Figure A - 1. ^{13}C NMR (APT) spectrum of Br-PPC (101 MHz, CDCl_3).

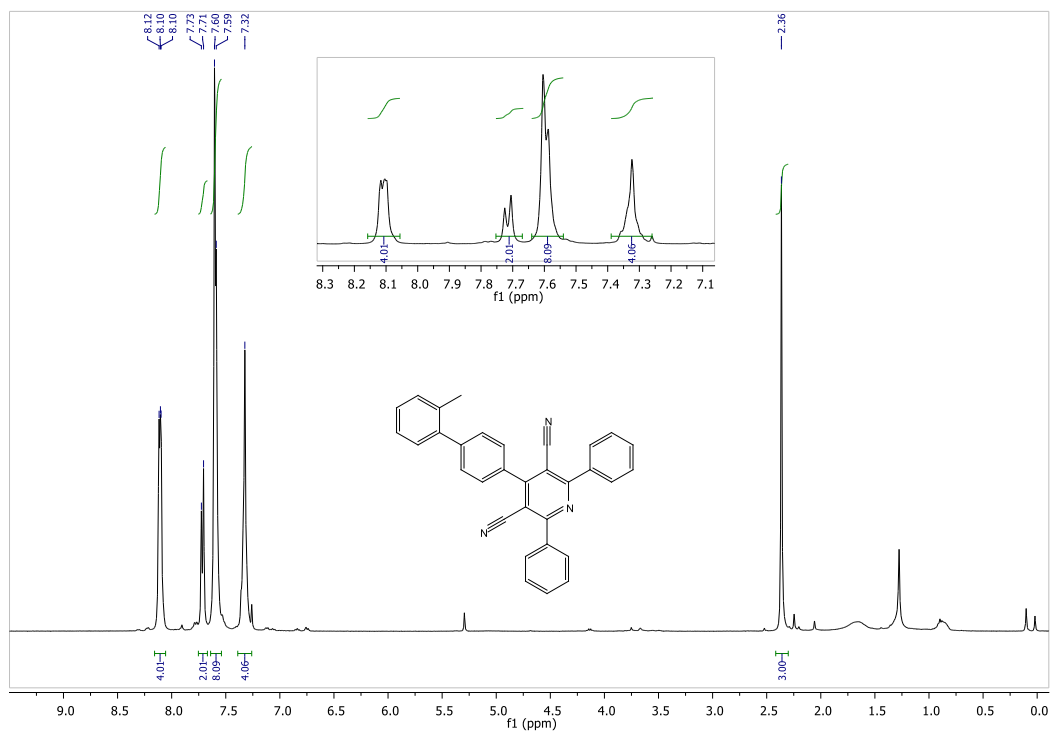


Figure A - 2. ^1H NMR spectrum of 2M-PPC (400 MHz, CDCl_3).

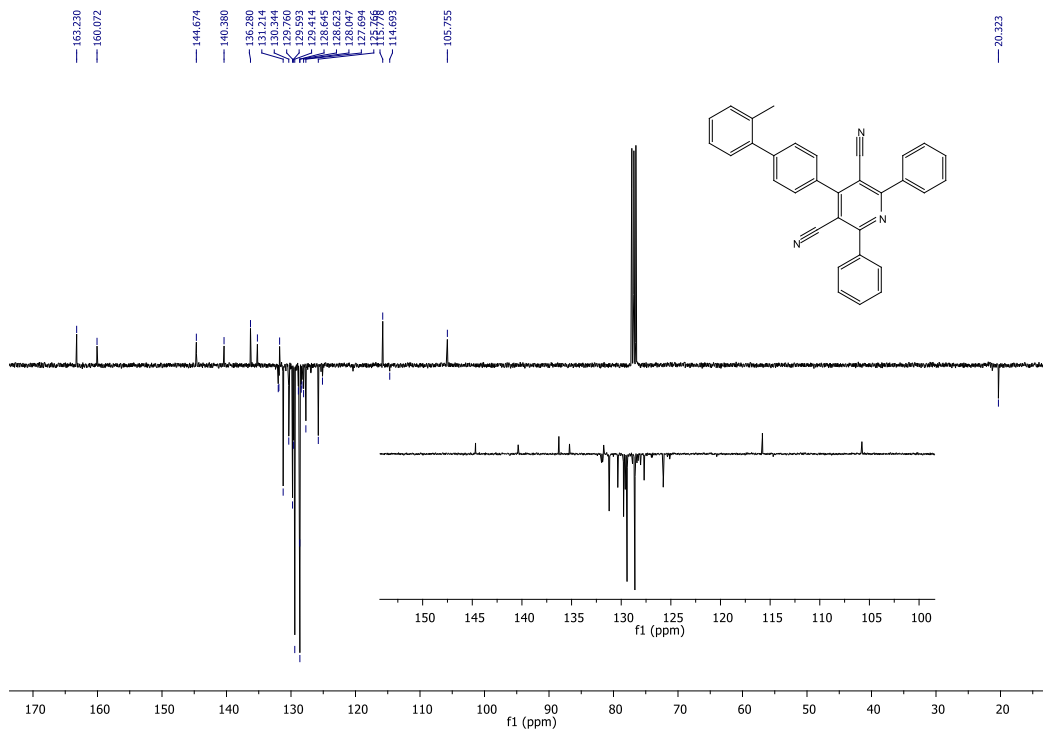


Figure A - 3. ^{13}C NMR (APT) spectrum of 2M-PPC (101 MHz, CDCl_3).

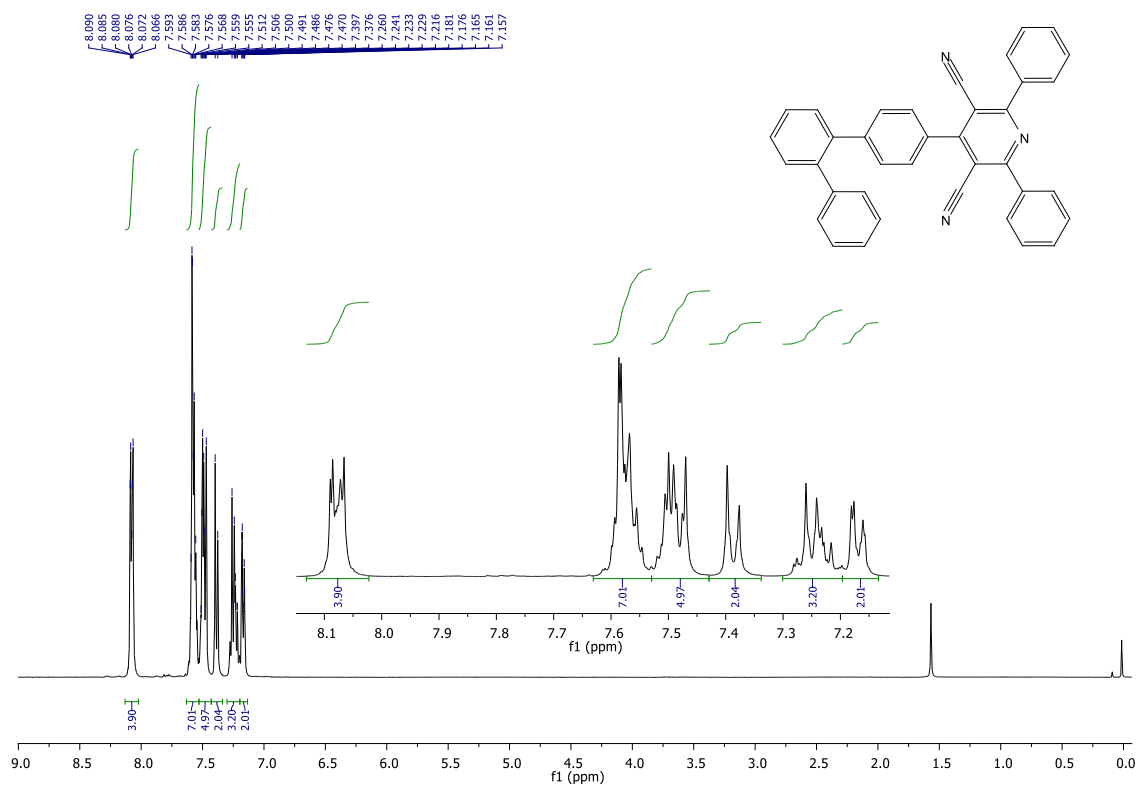


Figure A - 4. ^1H NMR spectrum of BP-PPC (400 MHz, CDCl_3).

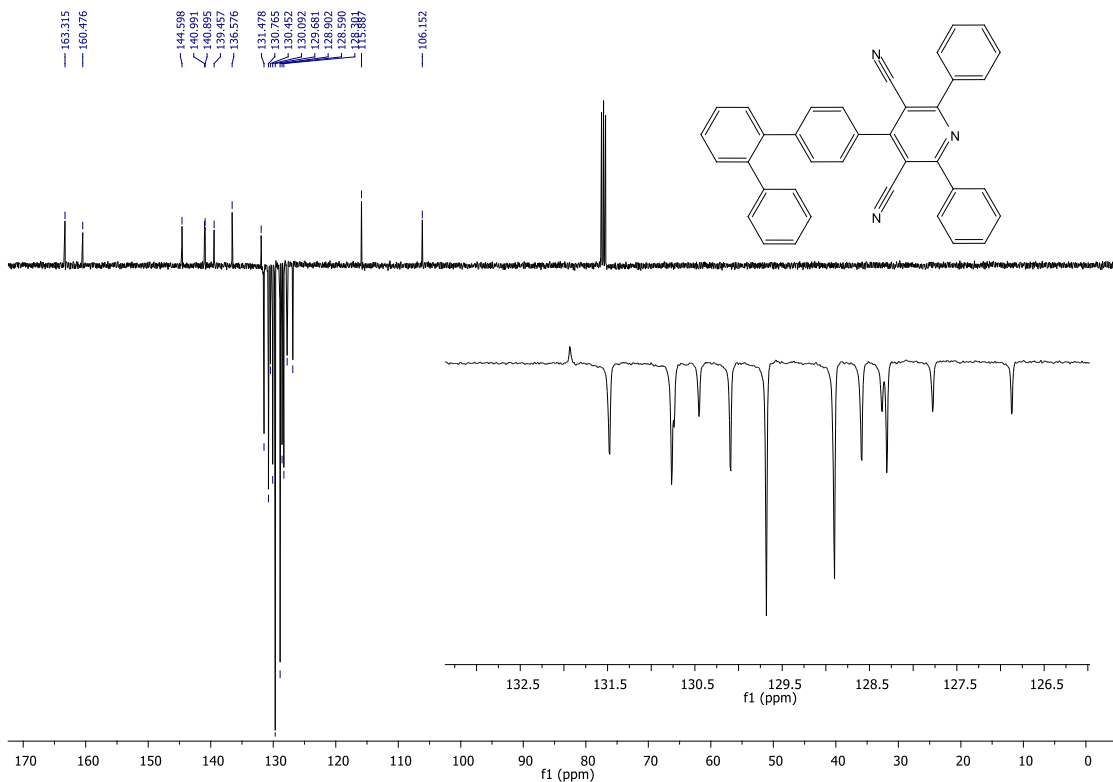


Figure A - 5. ^{13}C NMR (APT) spectrum of BP-PPC (101 MHz, CDCl_3)

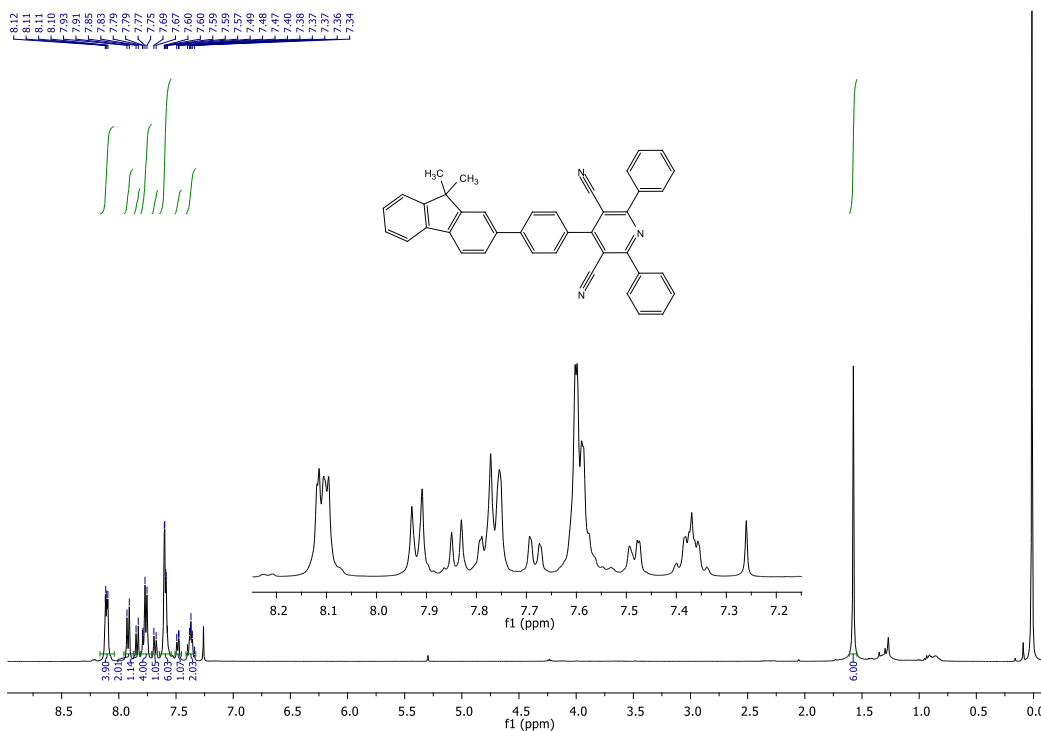


Figure A - 6. ^1H NMR spectrum of FL-PPC (400 MHz, CDCl_3).

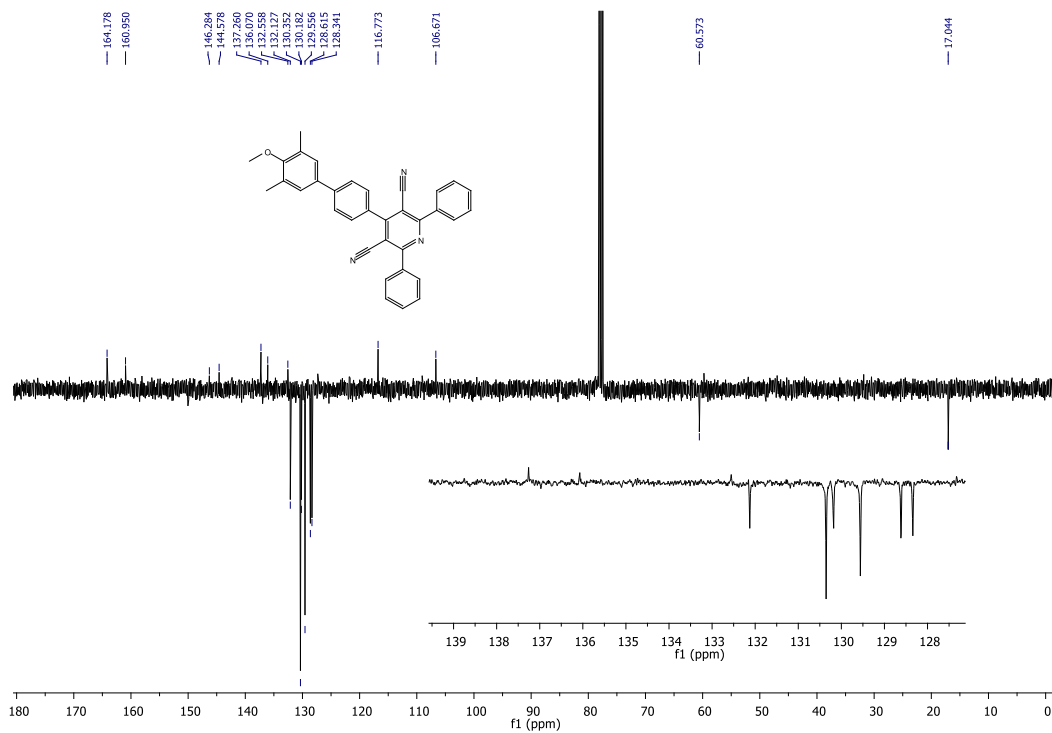


Figure A - 9. ¹³C NMR (APT) spectrum of MT-PPC (101 MHz, CDCl₃).

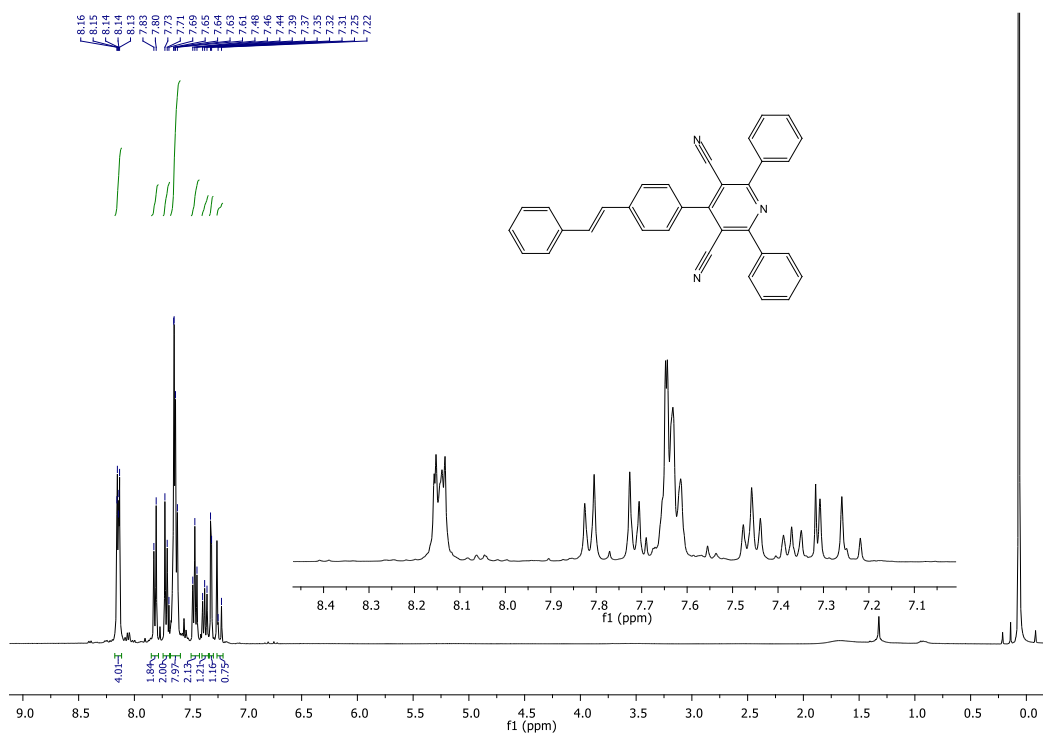


Figure A - 10. ¹H NMR spectrum of ST-PPC (400 MHz, CDCl₃).

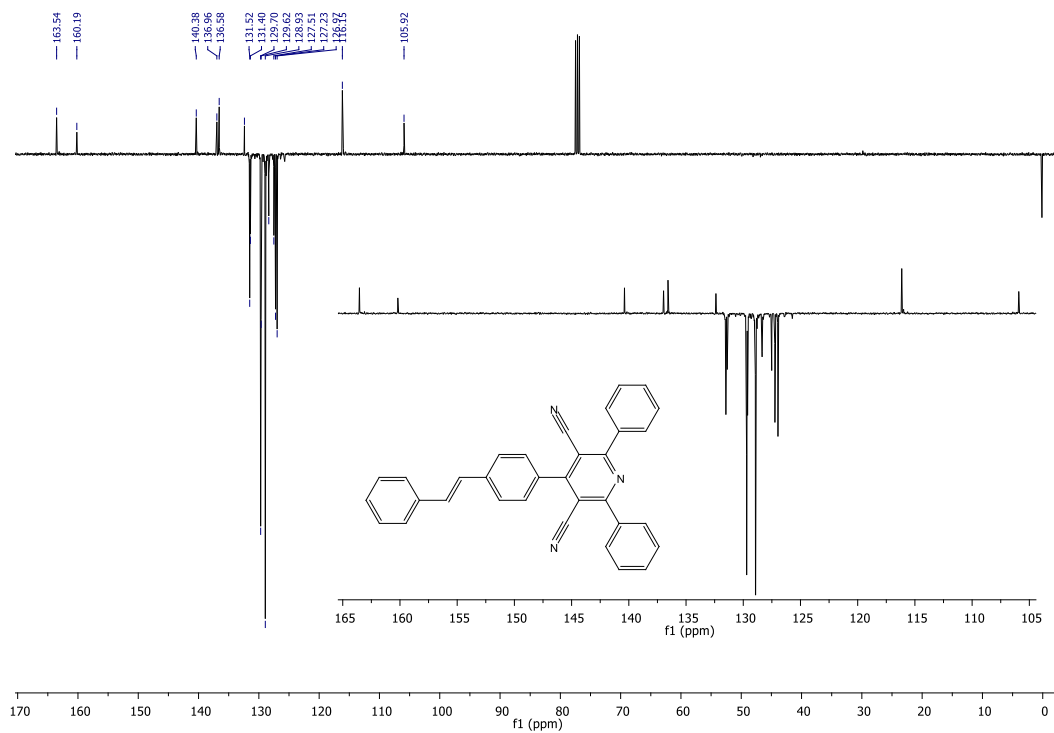


Figure A - 11. ^{13}C NMR (APT) spectrum of ST-PPC (101 MHz, CDCl_3).

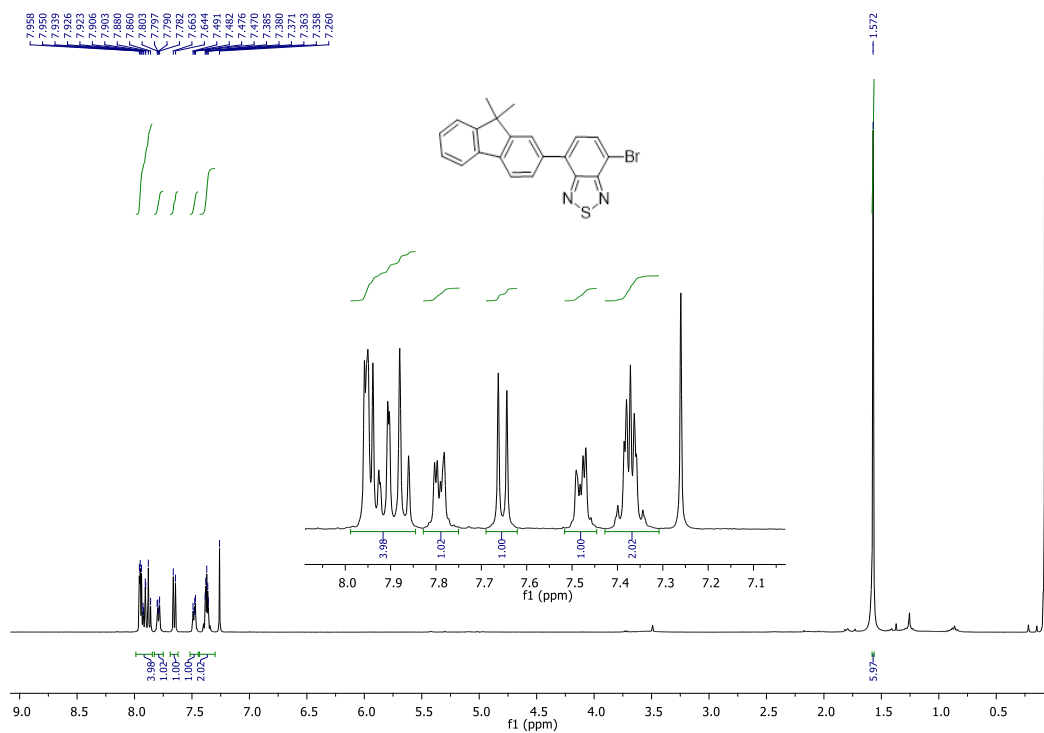


Figure A - 12. ^1H NMR spectrum of FL-BTD-Br (400 MHz, CDCl_3).

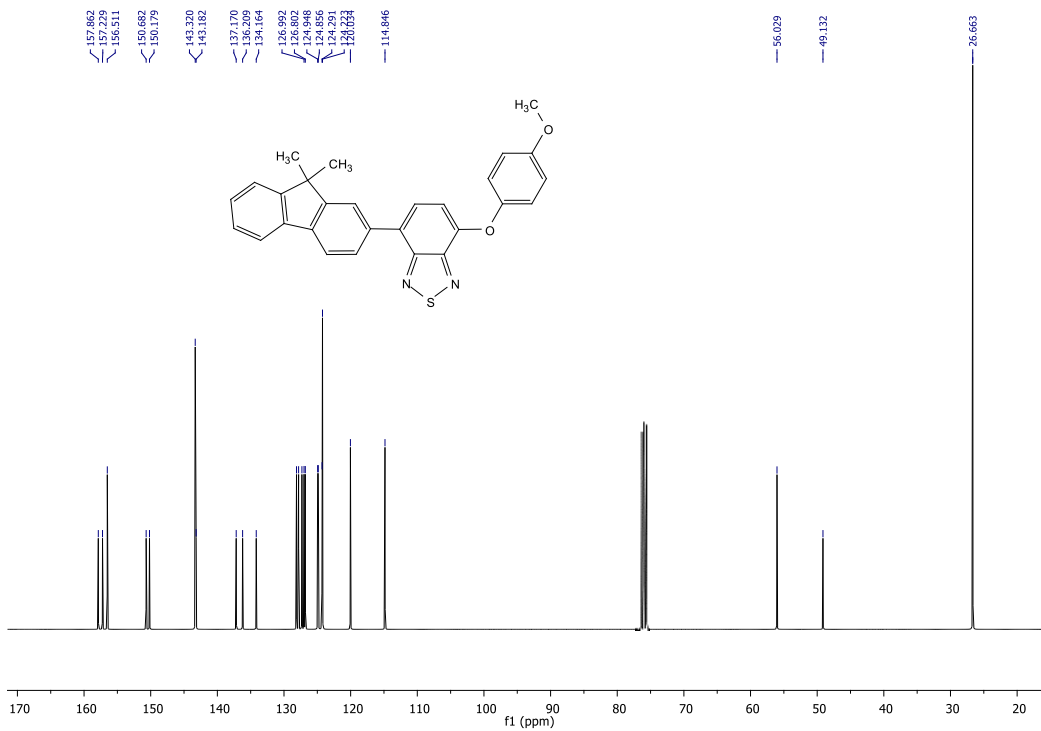


Figure A - 13. ¹³C NMR spectrum of FL-BTD-OAM (101 MHz, CDCl₃).

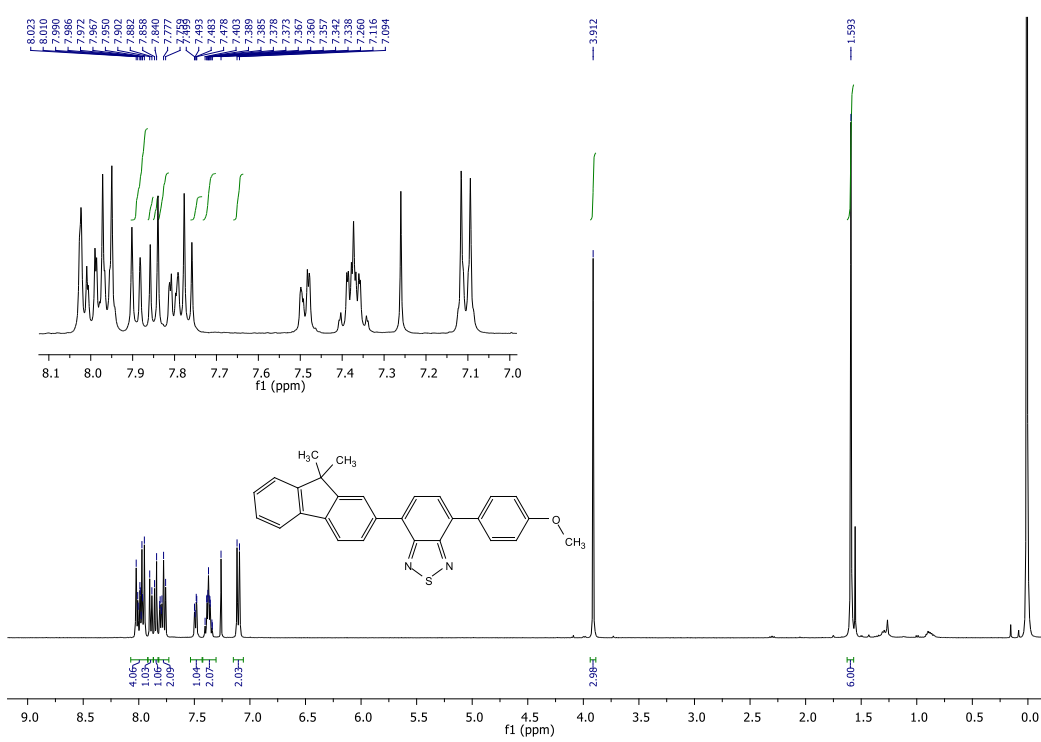


Figure A - 14. ¹H NMR spectrum of FL-BTD-AME (400 MHz, CDCl₃).

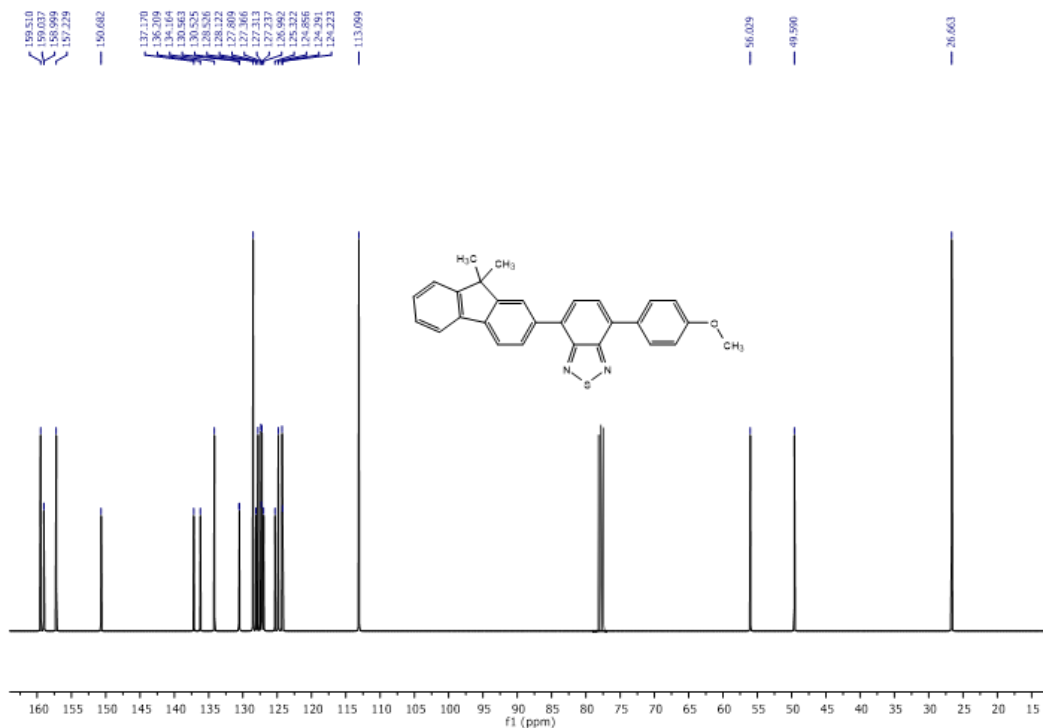


Figure A - 15. ^{13}C NMR spectrum of FL-BTD-AME (101 MHz, CDCl_3).

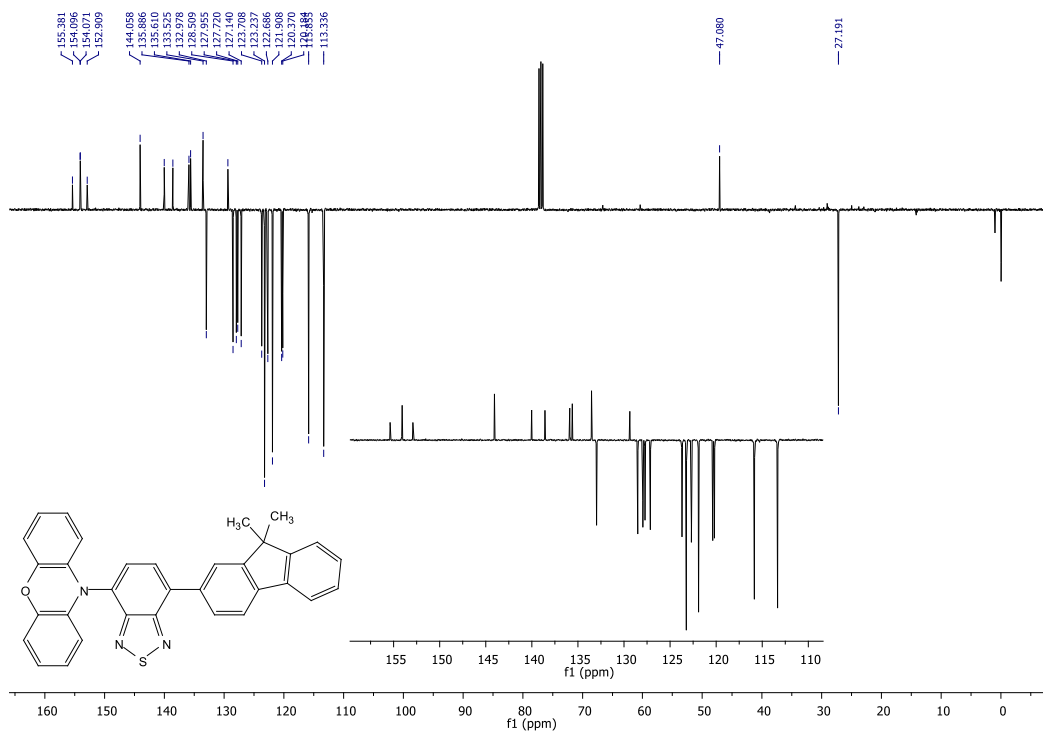


Figure A - 16. ^{13}C NMR (APT) spectrum of FL-BTD-PXZ (101 MHz, CDCl_3).

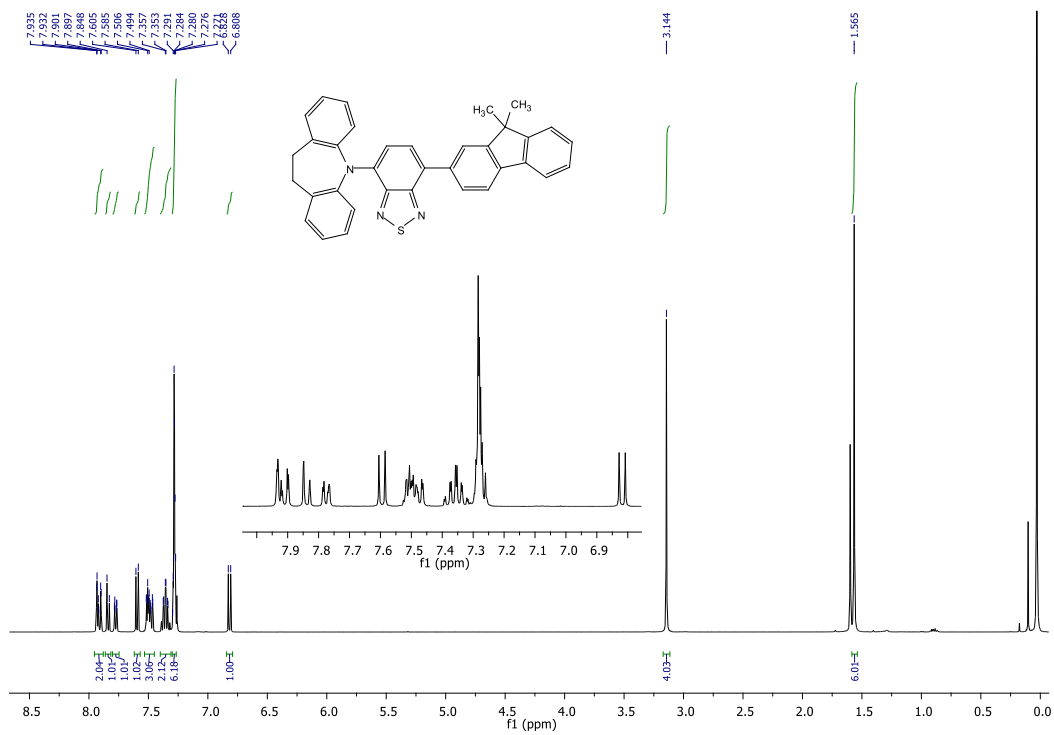


Figure A - 17. ^1H NMR spectrum of FL-BTD-IDB (400 MHz, CDCl_3).

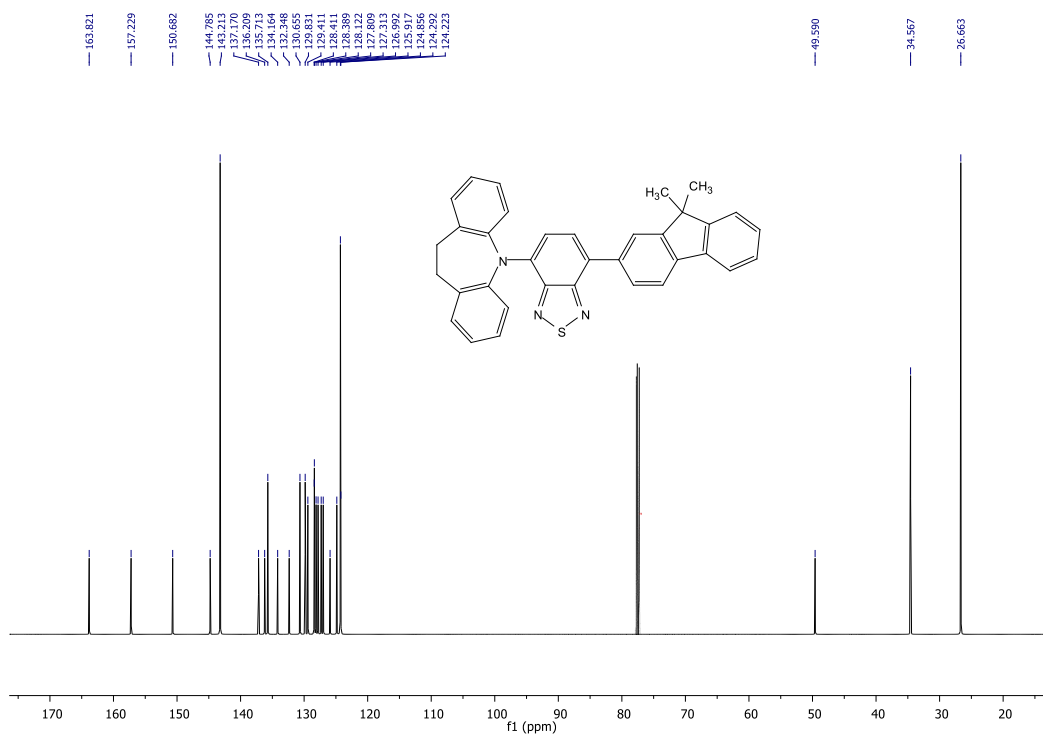


Figure A - 18. ^{13}C NMR spectrum of FL-BTD-IDB (101 MHz, CDCl_3).

A2. Crystallographic data

Table A - 1. Crystallographic data and structure refinement parameters for BP-PPC and FL-PPC.

	BP-PPC	FL-PPC
Molecular formula	C ₃₇ H ₂₃ N ₃	C ₄₀ H ₂₇ N ₃
FW (g mol ⁻¹)	509,58	549.65
T (K)	100 (2)	100(2)
Crystal system	Triclinic	Orthorhombic
Space group	P(-1)	Pca2(1)
a (Å)	9.2363(6)	18.5076(6)
b (Å)	11.4244(7)	19.8008(7)
c (Å)	15.5490(10)	7.6119(2)
α (°)	105.276(2)	90
β (°)	95.891(2)	90
γ (°)	104.620(2)	90
V (Å ³)	1506.15(17)	2789.50(15)
Z	2	4
ρ calc. (g cm ⁻³)	1.124	1.309
μ (mm ⁻¹)	0.066	0.077
F(000)	532	1152
Crystal size (mm)	0.23 x 0.13 x 0.10	0.12 x 0.06 x 0.03
θ range (°)	2.01 to 26.82	2.06 to 28.67
	-11 ≤ h ≤ 11	-24 ≤ h ≤ 24
Limiting indices (h, k, l)	-13 ≤ k ≤ 14	-26 ≤ k ≤ 26
	-18 ≤ l ≤ 19	-9 ≤ l ≤ 6
Reflections collected	24776	34782
Reflections unique (R _{int})	6422 [0.0592]	6241 [0.0934]
Completeness to θ _{max} (%)	99.5	99.7
Data/restraints/parameters	6422 / 0 / 361	6241 / 1 / 388
Absorption correction	Semi-empirical from equivalents	
Max. and min. transmission	0.9834 and 0.9949	0.9977 and 0.9880
R ₁ (I > 2σ(I))	0.0604	0.0566
wR ₂ (I > 2σ(I))	0.1302	0.0995
R ₁ (all data)	0.1027	0.0875
wR ₂ (all data)	0.1431	0.1097
S on F ²	1.028	1.062
Largest diff. peak and hole (e.Å ⁻³)	0.244 and -0.276	0.274 and -0.277

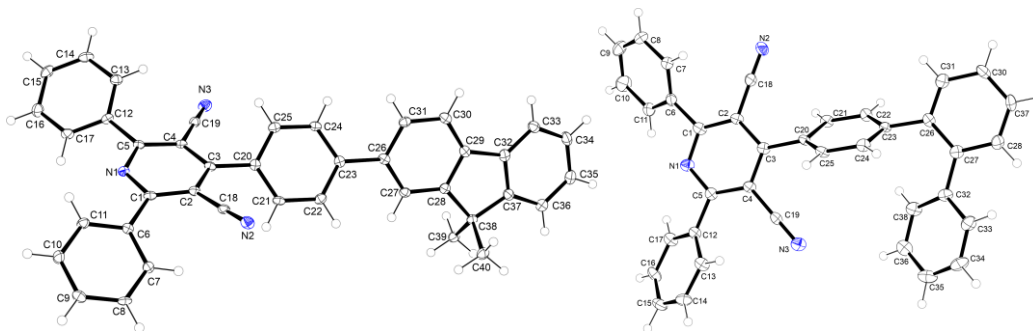


Figure A - 19. Crystal structures for FL-PPC (left) and BP-PPC (right).

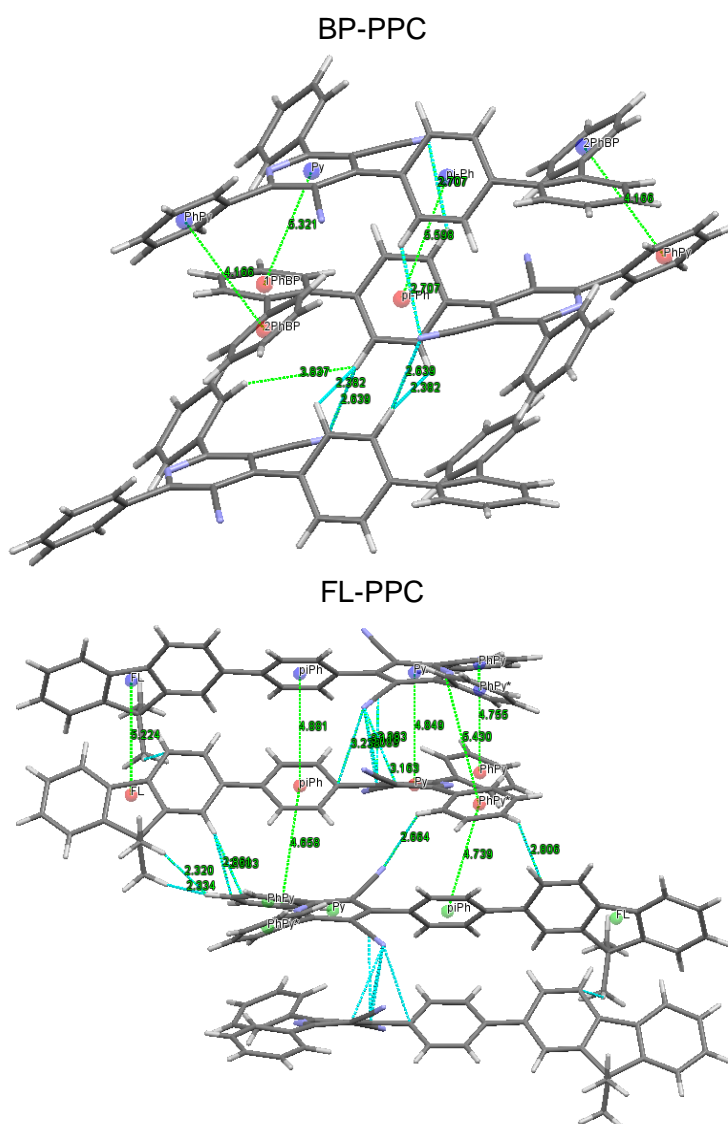


Figure A - 20. Distance lengths (Å) between short contacts and centroids for BP-PPC (top) and FL-PPC (bottom)

Table A - 2. Distance lengths (Å) for BP-PPC

Object 1	Object 2	Length (Å)	Distance measured
Py	1PhBP	5.321	Centroids
pi-Ph	pi-Ph	5.598	Centroids
2PhBP	PhPy	4.166	Centroids
PhPy	2PhPB	4.166	Centroids
N3	H21	2.707	Short contact
H25	H24	2.381	Short contact
H24	N3	2.639	Short contact

Table A - 3. Distance lengths (Å) for FL-PPC

Object 1	Object 2	Length (Å)	Distance measured
FL	FL	5.224	Centroids
piPh	piPh	4.881	Centroids
Py	Py	4.849	Centroids
PhPy	PhPy	4.755	Centroids
PhPy*	PhPy*	4.921	Centroids
piPh	PhPy	4.976	Centroids
N3	C18	3.118(3)	Short contact
N3	C20	3.238(4)	Short contact
N3	C3	3.089(4)	Short contact
N3	C2	3.363(4)	Short contact
C19	C3	3.363(4)	Short contact
H7	N2	2.664	Short contact
C9	H38	2.883	Short contact
C10	H38	2.861	Short contact
H10	H39A	2.334	Short contact
H10	H40A	2.320	Short contact
H9	C27	2.806	Short contact

Table A - 4. Crystallographic data and structure refinement parameters for FL-BTD-OAM and FL-BTD-AME.

	FL-BTD-OAM	FL-BTD-AME
Molecular formula	C ₅₆ H ₄₄ N ₄ O ₄ S ₂	C ₂₈ H ₂₂ N ₂ O ₂ S
FW (g mol ⁻¹)	901.07	434.54
T (K)	296 (2)	100 (2)
Crystal system	Triclinic	Monoclinic
Space group	P (-1)	P 21/c
a (Å)	8.0515 (6)	18.7392 (6)
b (Å)	11.1009 (8)	14.7782 (4)
c (Å)	25.2918 (18)	7.7873 (2)
α (°)	96.125 (3)	90
β (°)	97.954 (4)	91.0780 (10)
γ (°)	90.598 (4)	90
V (Å ³)	2225.3 (3)	2156.17 (11)
Z	2	4
ρ calc. (g cm ⁻³)	1.345	1.339
μ (mm ⁻¹)	1.520	0.174
F(000)	944	912
Crystal size (mm)	0.109 x 0.03 x 0.02	0.30 x 0.21 x 0.20
θ range (°)	4.01 to 83.13	2.17 to 30.57
Limiting indices (h, k, l)	-10 ≤ h ≤ 9 -14 ≤ k ≤ 13 -32 ≤ l ≤ 31	-26 ≤ h ≤ 25 -21 ≤ k ≤ 21 -11 ≤ l ≤ 10
Reflections collected	220041	34201
Reflections unique (Rint)	9925 [0.0647]	6589 [0.0254]
Completeness to θmax (%)	83.13 99.6%	30.57 99.6%
Data/restraints/parameters	9925 / 0 / 596	6589 / 0 / 289
Absorption correction	Semi-empirical from equivalents	
Max. and min. transmission	0.7543 and 0.6358	0.9660 and 0.9396
R1 (I > 2σ(I))	0.1771	0.0368
wR2 (I > 2σ(I))	0.1106	0.0983
R1 (all data)	0.2103	0.0429
wR2 (all data)	0.2310	0.1021
S on F2	2.108	1.032
Largest diff. peak and hole (e.Å ⁻³)	1.097 and -0.791	0.456 and -0.297

FL-BTD-OAM

FL-BTD-AME

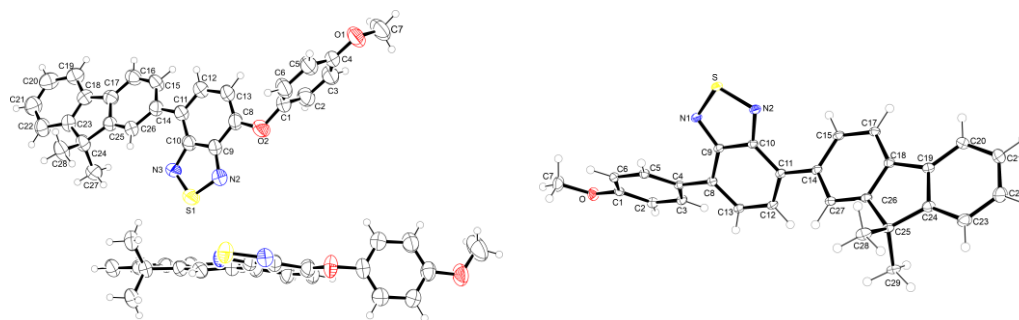


Figure A - 21. Crystal structures for FL-BTD-OAM and FL-BTD-AME

Table A - 1. Degree of torsion between planes of donor and acceptors in FL-BTD-OAM.

Plane 1	Plane 2	Degree
FL1	BTD1	16.13
BTD1	OAM1	80.58
OAM1	FL1	71.32
FL2	BTD2	15.46
BTD2	OAM2	80.38
OAM2	FL2	70.68
BTD1	BTD2	86.65
FL1	FL2	61.98
OAM1	OAM2	80.34

Table A - 6. Measured distances in FL-BTD-OAM.

Object 1	Object 2	Length (Å)	Distance measured
BTD1	BTD2	5.336	Centroids
BTD2	BTD3	3.864	Centroids
S1	N2	2.195	Short contact

A3. Delayed fluorescence

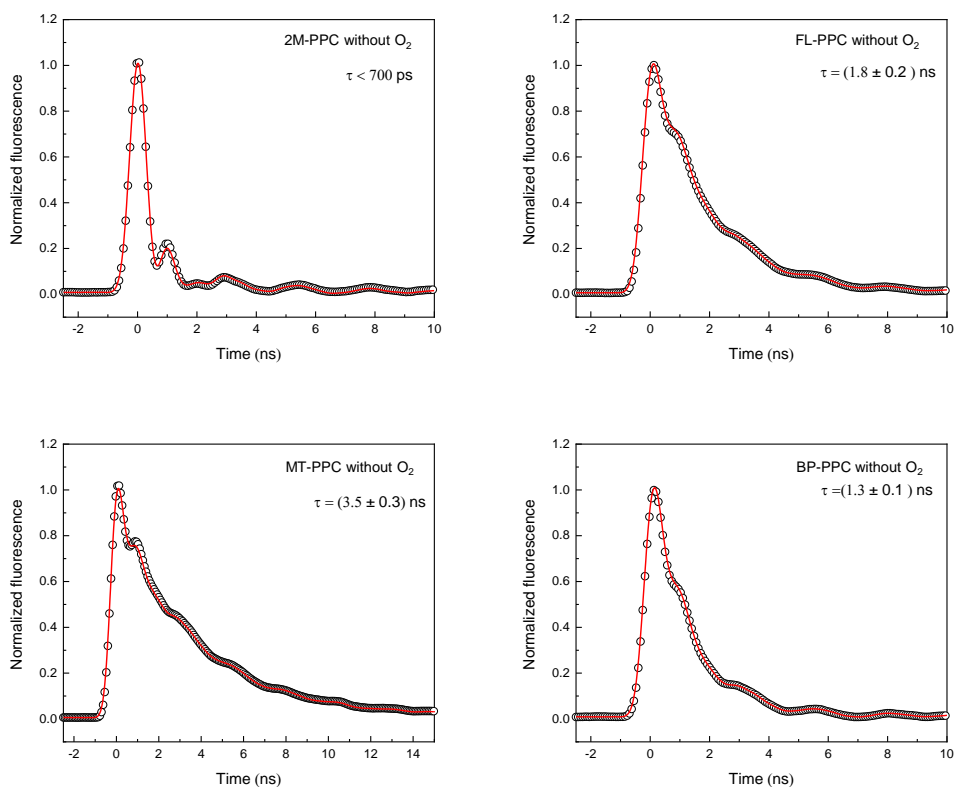


Figure A - 22. Fluorescence decays of PPC derivatives in Toluene.

A4. Cyclic voltammetry

Table A - 7. Cyclic voltammetry results for FL-BTD-OAM.

E^{ox} onset (V)	E^{red} onset (V)	HOMO (eV)	LUMO (eV)	E_{gap} (eV)
1.515	-0.9538	-5.845	-3.3762	2.4688

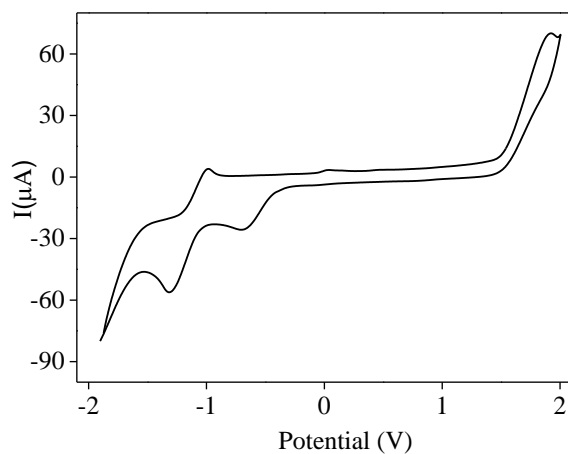


Figure A - 23. Cyclic voltammetry curve of FL-BTD-OAM.

A5. Licenses

Table A - 8. Licenses for adapted or reproduced objects.

Object	Reference	Licensed Publisher	License number
Figure 1	26	John Wiley & Sons, Inc.	5501701217179
Figure 2	28	Springer Nature	5501710786814
Figure 5	40	John Wiley & Sons, Inc.	5501711196050
Figure 10	8	John Wiley & Sons, Inc.	5501691223748
Figure 13	85	Royal Soc of Chem	1330293-1